UNIVERSITAT POLITÈCNICA DE CATALUNYA

DOCTORAL THESIS

Integration and electrical manipulation of single-photon sources in 2-dimensional devices

---

Author:
Carlotta CIANCICO

Supervisor:
Prof. Dr. Frank KOPPENS

Co-supervisor:
Dr. Antoine RESERBAT-PLANTEY

A thesis submitted in fulfillment of the requirements for the degree of Doctor of Photonics

in the

Quantum Nano-Optoelectronics Group
ICFO - The Institute of Photonic Sciences

"For there is always light,
if only we're brave enough to see it.
If only we're brave enough to be it."

Amanda Gorman, *The Hill We Climb*

Abstract

Quantum nanophotonics aims at studying the interaction between matter and single photons at the nanoscale. Nanoscopic solid state light sources can be placed in near proximity to other photonic elements to engineer their environment and modify their behaviour by near-field effects. The use of quantum emitters guarantees on-demand single photons following non-classical statistics, therefore allowing new types of phenomena at the nanoscale. The nanometer-sized single photon sources used in this thesis are stable, bright, narrow linewidth organic molecules. They are also scalable and reproducible, making them ideal for integration into a device as well as for tuning and sensing.
In this thesis, we developed an original approach to explore near-field effects by combining ultranarrow linewidth quantum emitters with 2-dimensional materials. We present the experimental setup based on confocal microscopy at cryogenic temperatures allowing us to excite and collect emission from individual elements of the hybrid device.
We first introduce a geometry of a device consisting of a capacitor where the 2-dimensional material is used as a transparent, non-invasive top electrode, deposited above a layer of polymer doped with quantum emitters. This configuration enables tuning of the single-photon emission by Stark shift over a range of 10^4 times the molecule's intrinsic linewidth. Dynamical modulation of the emission at high frequency (similar to the molecule's linewidth $\sim$ 100 MHz) is performed revealing interesting properties of the 2-dimensional electrode.
Another geometry explored in this thesis is achieved by depositing doped nanocrystals on top a graphene field-effect transistor. We study the electrostatic behaviour of the device at different locations, observing anomalies in the Stark shift of the molecules' emission at the edge of the graphene device compared to the centre. We predict the saturation of

atomic scale defect states at the edge of graphene, as supported by our electrostatic model.
A technique based on electron beam lithography of polymers for deterministic positioning 3D structures aligned on quantum emitters' location is also presented.

Resumen

La nanofotónica cuántica tiene como objetivo estudiar la interacción entre la materia y los fotones individuales a nanoescala. Las fuentes de luz de estado sólido nanoscópicas se pueden colocar muy cerca de otros elementos fotónicos para diseñar su entorno y modificar su comportamiento mediante efectos de campo cercano. El uso de emisores cuánticos garantiza fotones individuales bajo demanda siguiendo una estadística no clásica, permitiendo así nuevos tipos de fenómenos a nanoescala. Las fuentes de fotones individuales de tamaño nanométrico utilizadas en esta tesis son moléculas orgánicas estables, brillantes y de ancho de línea estrecho. También son escalables y reproducibles, lo que los hace ideales para la integración en un dispositivo, así como para la sintonización y la detección.
En esta tesis, desarrollamos un enfoque original para explorar los efectos de campo cercano mediante la combinación de emisores cuánticos de ancho de línea ultra estrecho con materiales bidimensionales. Presentamos la configuración experimental basada en microscopía confocal a temperaturas criogénicas que nos permite excitar y recolectar emisiones de elementos individuales del dispositivo híbrido.
Primero presentamos una geometría de un dispositivo que consiste en un capacitor donde el material bidimensional se usa como un electrodo superior transparente y no invasivo, depositado sobre una capa de polímero dopado con emisores cuánticos. Esta configuración permite el ajuste de la emisión de un solo fotón por el cambio de Stark en un rango de 10^4 veces el ancho de línea intrínseco de la molécula. La modulación dinámica de la emisión a alta frecuencia (similar al ancho de línea de la molécula $\sim$ 100 MHz) se realiza revelando propiedades interesantes del electrodo bidimensional.
Otra geometría explorada en esta tesis se logra depositando nanocristales

dopados en la parte superior de un transistor de efecto de campo de grafeno. Estudiamos el comportamiento electrostático del dispositivo en diferentes ubicaciones, observando anomalías en el cambio Stark de la emisión de moléculas en el borde del dispositivo de grafeno en comparación con el centro. Predecimos la saturación de los estados de defecto a escala atómica en el borde del grafeno, como lo apoya nuestro modelo electrostático.
También se presenta una técnica basada en la litografía por haz de electrones de polímeros para el posicionamiento determinista de estructuras 3D alineadas en la ubicación de los emisores cuánticos.

Acknowledgements

I would like to thank Prof. Stéphane Berciaud, Alex Clark and Niek Van Hulst for agreeing to be part of my PhD committee and for dedicating their time to read and comment this thesis.
My acknowledgments go to Prof. Frank Koppens for opening the doors of ICFO to me. These have been challenging years, thanks for giving me the platform to push myself and to grow.
Thanks to Antoine, for supervising me from the very first day of my PhD. I appreciated our daily conversations from fundamental physics to more light topics. Thank you for your big help with every written and oral presentation, especially this thesis. Kevin, you have been like a big brother in the lab to me. I have learn so much from you and enjoyed the time spent together in and outside the lab. The reign of Lab 206 goes now to Max and Álvaro. Have fun guys!
I'm grateful to Prof. Costanza Toninelli and the group at LENS, Pietro, Sofia and Maia, for sharing with us their knowledge on DBT molecules. I want to acknowledge the help from Dr. Johann Osmond, who often shared with me his huge technical experience and fun conversations.
I've had very enjoyable years in the NOE group and was sad to see many friends leaving before me. Achim, Peter, Mathieu, Jianbo, Teresa, Stijn and all the NOEs: thanks for being great friends before colleagues over these years. A big praise goes to Iacopo for being a fun neighbor and for his priceless help towards a deeper understanding of our often mysterious results. A kind thought goes to my warrior princess Gabi, a great companion of many sporty and non-sporty adventures. A special NOE member also deserves my acknowledgments. Bernat, thanks for being my family in Barcelona, for your support and your always provoking science discussions.
I'd like to acknowledge all the amazing people I've met at ICFO who have made the experience of the PhD more enjoyable. It was a pity to

have lost almost to years to Covid (and eventually to finish this thesis). Ale e Cate, you have been the greatest friends, sharing many fun experiences together, not-so-artistic results and infinite chats over life.
My Italian fiends: Ele, Fra, Fede, Ludo, Marti, Anna, Michele, Ila, Gio, Gemma,Francesco, Lorenzo who in their own special ways have supported me over these 5 years. *Grazie* to my mum and dad, who are proud of me even when I'm reluctant to share what is it that I'm really doing. To my brother Giacomo and sisters Giulia and Valeria, I will forever be your nerdy sister.

Contents

Chapter 1

Hybrid systems interfacing solid-state quantum emitters with 2-dimensional materials

Photonics focuses on controlling light-matter interactions for the development of new optical technologies for material science, communication, information processing and sensing. The transition into nanophotonics, supported by fabrication advances towards the integration of different photonic elements on-chip, enables the exploration of new types of physical effects at the nanoscale.
Based on the discovery of the rules of quantum mechanics, a second quantum revolution is now happening in the field of quantum technology, aiming at answering the increasing world wide demand for secure communication and fast transmission of huge amounts of data. In order to do so, a new type of light sources following a non-classical photon statistics need to be introduced. While quantum emitters are often fabrication- and experimental-wise quite challenging, they guarantee emission of one and only one photon at a time, with well-defined emission energy and narrow linewidth, proven anticorrelation and indistinguishability of the emitted photons and often access to the spin degree of freedom, opening the way to new physical phenomena and optical operations.

With initiatives like the Quantum Flagship (1 billion €) and prediction for the quantum computing market to exceed six billions € in 2027 globally [1], it's clear that Europe and the rest of the world have a very strong interest in bringing quantum technology from labs to market.

Some examples of companies exploiting single-photon sources (SPSs) for different quantum applications are already growing strong in Europe. Qnami (Basel) and QZabre (Zürich) use the control and measurement of a single spin in a nitrogen vacancy centre (NVC) in diamond to achieve extreme quantum sensing. Commercial single-photon sources integrated on-chip have been realized using semiconducting quantum dots (QDs) (Quandela, Paris) and 2D materials (NuQuantum, Cambridge). Single molecules also attracted commercial interest for ultrahigh-resolution inkjet printing of solutions containing organic molecules based on electrostatic droplet actuation, for deterministic positioning (Scrona, Zürich) [2].
Although much progress still needs to be made in terms of optimizing and making commercially available quantum technologies, we can be sure we have ahead of us a decade of exciting developments and breakthroughs.

1.1 Single molecules as narrow linewidth emitters for quantum technology

What are single photons needed for [3]? Even for present-day quantum technologies it is clear that single-photon sources are not always necessary. For example, for point to point quantum key distribution a faint pulsed laser could be used successfully instead. However, to guarantee secure long-lived quantum communication on-demand single indistinguishable photons are required [4].

SPSs follow a non-classical behaviour and behave according to the laws of quantum mechanics, which makes them key players for photonic quantum simulation [6, 7], linear optical quantum computing [8], device-independent quantum key distribution [3], and quantum metrology [9]. Trapped ions [10] and cold gases [11] (see Fig. 1.1a) have been the first reliable source of on-demand photons, but they require complex and bulky setups. For these reasons, solid state emitters became a promising alternative [4] as the ones closest to an ideal single-photon source, defined as a light source emitting deterministically one and only one photon at a time with 100% probability (see Fig. 1.1b,c).
Most solid state quantum emitters display their optimal emission properties when deeply embedded in the bulk material, hampering the access to

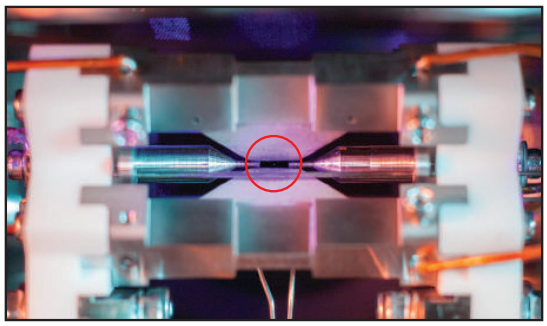

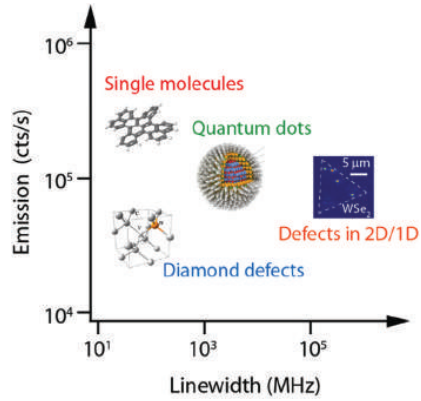

c

Table 1 | Summary of photophysical properties of solid-state SPEs.

	Maximum count rate (without a cavity, continuous wave) (counts s^{-1})	Lifetime (ns)	Homogeneous linewidth at 4 K	Indistinguishable photons (IP) and entanglement (E)	Spatial targeted fabrication of single emitters	Operation temperature	Integration of SPEs with dielectric cavities or plasmonic resonators
Colour centres in diamond	SiV: ~3×10^6 (ref. 138)* NV: ~1×10^6 (ref. 139)† For other sources see ref. 28	SiV: ~1 NV: ~12–22	NV, SiV lifetime-limited[29,30] Cr-related: 4 GHz (ref. 140)	NV: IP, E SiV: IP	Only for NV and SiV (ref. 28)	RT	Dielectric: NV, SiV only Plasmonics: NV only
Defects in SiC, ZnO and BN Rare earths in YAG/YOS	YAG: ~60×10^3 (ref. 141) ZnO: ~1×10^5 (ref. 44) SiC: ~2×10^6 (ref. 35) BN: ~3×10^6 (ref. 56)	19 (ref. 49)§ 1–4 (ref. 44) 1–4 (ref. 35) ~3 (ref. 56)	N/A	No	No	RT	No
Arsenide QDs	~1×10^7 (ref. 84)‡	~1 (refs 6,84)	Lifetime-limited	Yes	Yes	4 K	Yes
Nitride QDs	N/A	~0.3 (ref. 85)	~1.5 meV (ref. 85)	No	Yes	RT	Dielectric: yes Plasmonics: no
CNTs	~3×10^3 (ref. 68)	~0.4 (ref. 68)	N/A	No	No	RT	Dielectric: yes Plasmonics: no
2D TMDCs	~3.7×10^5 (ref. 57)	~1–3 (ref. 57)	N/A	No	No	4 K	No

The reported count rates for each system can be potentially optimized by integrating with cavities or improving collection optics. *Reported from a nanodiamond on iridium. †Recorded from a nanodiamond positioned on a solid immersion lens. Similar values obtained by etching a bullseye grating into a diamond membrane[142]. In both cases emitters in bulk diamond are dimmer. ‡Count rate at the objective, which is directly comparable to other systems. §Realized by optical upconversion to a short-lived excited state. N/A, not available; RT, room temperature.

Figure 1.1: Single-photon emission. **a:** Photo of a single atom in an ion trap (courtesy of David Nadlinger, University of Oxford). **b:** Representation of solid state single-photon sources based on their linewidth and emission intensity. Adapted from Ref. [5]. **c:** Summary of the photophysical properties of solid state quantum emitters. Adapted from Ref. [4].

near-field effects. Hence there is a quest to find emitters which preserve their brightness and narrow linewidth when at the surface or enclosed in a truly nanoscopic environment. This configuration would allow us to explore physical effects at the nanoscale as well as to sense charges and fields via the optical readout of environmental perturbations of the single-photon emission [12].

Among these atom-like emitters we find nitrogen vacancy centers in diamond nanocrystals (NVCs) [13], quantum dots (QDs) [14], carbon

nanotubes (CNTs) [15], Polycyclic Aromatic Hydrocarbons (PAH) in a nanocrystalline environment (DBT, DBATT) [16], emitters in 2D materials [17]. In this work, we will focus our attention on organic single molecules. These low cost, scalable SPSs rely on a flexible synthetic process of the organic chromophore inside a hosting matrix, giving access to a wide range of emission wavelengths. Single molecules are bright ($\sim 10^5$ counts/s as measured experimentally in our setup), stable, narrow linewidth (linewidth of bulk DBT $\sim$ 30 MHz [18]) and very reproducible.

1.1.1 Single organic molecules for photonic technologies

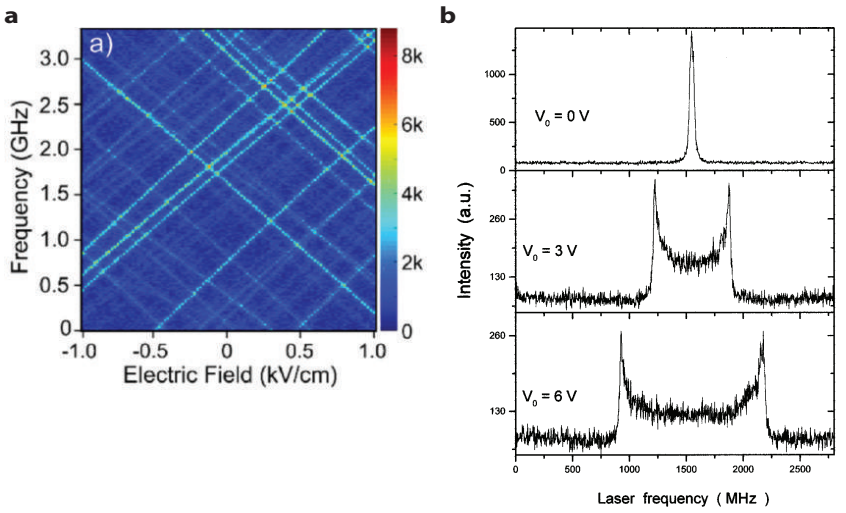

Figure 1.2: a: Single molecules in an in-plane electric field generated by two electrodes display strong linear Stark shift. **b**: AC voltage at three different amplitudes is applied to the device inducing oscillation of the molecule's emission resulting in the novel "Cat's ear". Panels adapted from: **a:** Ref. [19]; **b:** Ref. [20].

Single molecules have proven to be good sensors for electric fields [19] (Figure 1.2a) and local currents [20] (Figure 1.2b), thanks to their narrow linewidth and well defined transition energy. Due to their emission properties, the energy of these single-photon sources can be efficiently tuned electrostatically and even optically [21].

Ideally, we would like to couple these tunable probes with other nanophotonic elements for guiding, emission enhancement and exploring near-field effects. Thus, a huge effort has been put over the last years

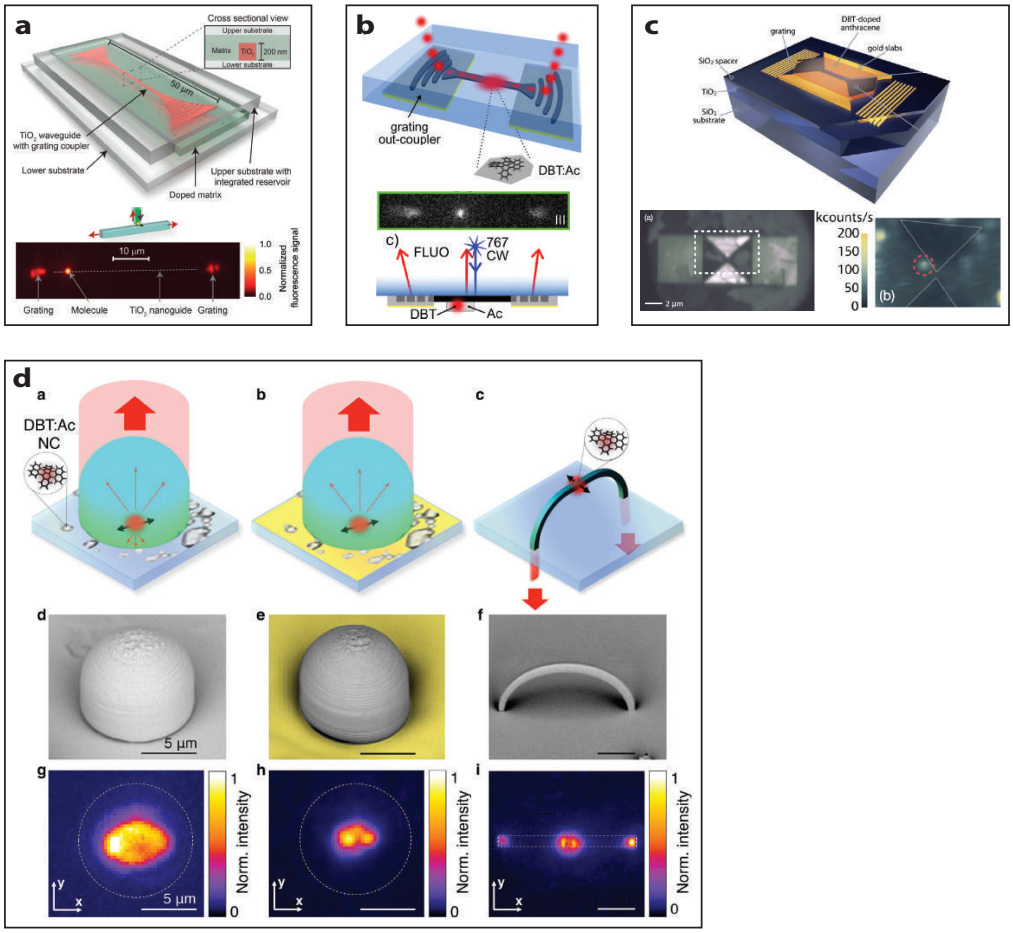

Figure 1.3: Integration of single molecules into waveguides and photonic structures. Examples of coupling to waveguides by capillarity (**a**) and deposition of a doped crystal (**b**,**c**). **d:** Lithographic approach to the design of 3D photonic architectures in polymers embedding single molecules. Panels adapted from: **a:** Ref. [22]; **b:** Ref. [23]; **c:** Ref. [24]; **d:** Ref. [25].

into integrating single molecules with nanophotonic structures such as waveguides [22–24, 26] (see Fig. 1.3a-c) and even 3D polymeric architectures [25] (see Fig. 1.3d). Often, these experiments are very challenging in terms of fabrication: on one hand we are handling organic material extremely sensitive to its environment, on the other rather big host crystals make integration at the nanoscale difficult. These aspects affect the outcome of positioning and coupling single molecules to nanophotonic structures.

Better control on the alignment between quantum emitters and nanophotonic elements as well as on the quantum emission tunability are needed. Achieving such improvements would be a big step forward towards the use of single molecules for classical and quantum nanotechnologies [27].

1.2 2-dimensional materials: a surface interface for optoelectronic applications

Nanoscale effects appear in the limit of distances $d < \lambda$, where λ is the emission wavelength, and can be effectively enhanced by engineering the surroundings of a quantum emitter in a non-invasive way. 2-dimensional materials are an interesting candidate for this role, as they offer a thin (atomic thickness) interface that can be placed as close as possible to a single-photon source to modify its optical properties as well as its electronic environment.
Within the family of 2-dimensional (2D) materials, we have access to different electronic properties: semi-metals like graphene [28, 29], semiconductors like transition metal dichalcogenides (TMDs) [30], insulators like hexagonal boron nitride (hBN) [31] and even superconductors [32]. These materials can also be combined into stacks to obtain an even better control of their electronic properties [33, 34].
2-dimensional membranes provide flexible optoelectronic elements whose fabrication technique has been perfected over the last fifteen years making it possible to interface them into more complex nanophotonic devices. Metal contacts are used to modify the electrostatic potential in the 2D device, allowing tuning of the electrical properties as well as of the charge dynamics, hence the electronic noise, of the material.

1.2.1 Modifying the environment of quantum emitters at the nanoscale

Working with nanoscopic emitters coupled to an atomically-thick layer means that we often work at distances $d < \lambda$, such that near-field effects become dominant. In this configuration, a plethora of physical effects which are otherwise negligible arise.
We can use the Fermi golden rule [39] to describe the transition rate between an initial state (1) and a final state (2) as:

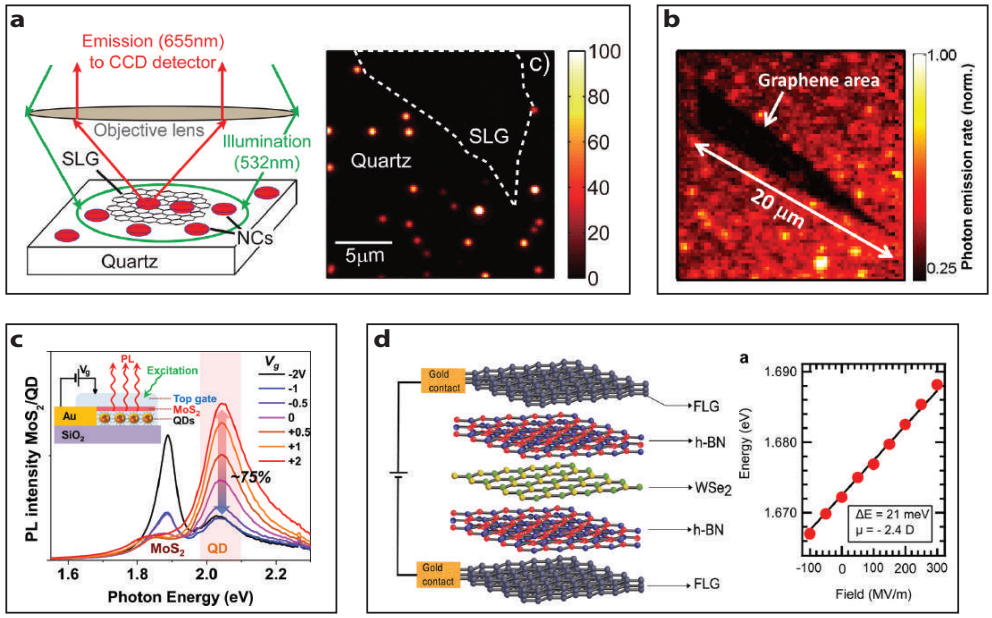

Figure 1.4: Non-radiative energy transfer (nRET) between quantum emitters and graphene (**a**, **b**) or a 2D semiconductor (**c**). **d:** Energy tuning of emitters in WSe_2 via Stark shift. Panels adapted from: **a:** Ref. [35]; **b:** Ref. [36]; **c:** Ref. [37]; **d:** Ref. [38].

$$\Gamma = \frac{2\pi}{\hbar} |M_{1,2}|^2 \, g(\hbar\omega) \tag{1.1}$$

where $|M_{1,2}|$ is the transition matrix element between the initial and final state and $g(\hbar\omega)$ is the density of final states. Equation 1.1 shows that the radiative decay of an emitter with a fixed transition matrix element is ruled by the density of optical states. This explains the enhancement in the spontaneous emission of an emitter by the Purcell effect [40] obtained by structuring its environment - that is the accessible optical states - using nanoscale geometries such as photonic crystals [41] and nanoantennas [42].

A relevant effect in hybrid devices combining quantum emitters with 2D materials is the non-radiative energy transfer (nRET). This dissipative phenomena causes an increase of the emission linewidth ($\Delta\nu \propto 1/d^4$) due to the opening of non-radiative decay channels for the excited emitter, therefore resulting in a reduction of the emission intensity. This effect has been observed with quantum emitters coupled to graphene [35, 36,

43–45] and 2D semiconductors [37] (see Figure 1.4). Similarly, stacks of TMDs and graphene exploit a selective non-radiative transfer effect for filtering photoluminescence from excitons in TMDs [46].
Dispersive effects such as Casimir-Polder shift and Stark shift also play a big role at the nanoscale and will be discussed in more details in the next section.
Our approach is therefore modifying the environment of single molecules to exploit the near-field effects arising between quantum emitters and 2-dimensional materials for tuning the single-photon emission and studying new physical phenomena. Our tool to explore such environmental effects is studying the emission properties of our ultranarrow linewidth emitters.

Casimir-Polder and Stark effect

The Casimir-Polder effect, a crucial prediction of quantum field theory, was first calculated in the idealised case of two neutral conducting plates with perfect reflection [47], then in the configuration of one neutral atom positioned in the vicinity of a conducting plate [48] and for any pair of neutral objects at short distance in general. The effect results from the modification of the vacuum electric field induced by the plate and was explained by modeling a spatially varying Lamb shift, whose gradient produces an attractive long-range force [49]. For quantum emitters, it is predicted to induce a shift of the transition frequency proportional to d^{-3} for a bulk material and d^{-4} for graphene, where d is the distance between the emitter and the interface [50]. The Casimir force dominates at very short distances and becomes essential when studying the interaction between objects at the nanoscale and in micro-electro mechanical devices (MEMS).
The Stark effect is the electric field-induced shift of the electronic levels of atoms or molecules resulting in a change of the emission energy. It was originally discovered by Stark in 1913 and in the same year by Lo Surdo - hence also called Stark-Lo Surdo effect - after the observation of enormous displacements in the spectra of some elements (as neon) produced by the application of an external electric field. In such configuration, the electrons would keep the same period of oscillation but centered around a new equilibrium position, causing a displacement of the potential energy. The effect was first described using the quantum formalism $\nu = \frac{E'' - E'}{h}$, where ν is the frequency of the new spectral line,

E', E'' the atomic energies of the "initial" and"final" stationary states and h is Planck's constant [51]. The Stark effect has been successfully observed in single molecules [19, 52, 53]. Their narrow optical band at cryogenic temperatures guarantees a strong shift in the emission energy, following the equation:

$$\hbar\Delta\omega_{ZPL} = a|\vec{E}| + b|\vec{E}|^2 \tag{1.2}$$

where a and b are the linear and quadratic Stark coefficients, which depend on the dipole moment and polarizability change, $\Delta\mu$ and $\Delta\alpha$ respectively, between ground and excited state. $\vec{E}$ is the external electric field. For centrosymmetric molecules, the dipole moments of both ground and excited states are zero therefore only a quadratic effect is expected. Still, disordered matrices can break the symmetry of the system allowing us to observe a linear shift. Stark shift has also been observed with emitters in 2D materials. By applying a perpendicular electric field we modify the separation between an electron-hole pair (exciton) trapped in a defect of the 2-dimensional system [38].

1.2.2 Engineering single-photon sources integrated in 2D materials

2D materials can also be used as a platform for engineering integrated SPSs. This approach has the obvious advantage of having maximum integration into a pure 2D optoelectronic platform and efficient interfacing into a device.
Different approaches have been used to fabricate quantum emitters in 2D materials. On one hand, strain has been used to localize excitons in 2D materials. A common technique used to apply controlled strain is by engineering the substrate with nanopillars and subsequently transferring the selected TMD on top. Interesting results have been obtained with WSe_2 at cryogenic temperatures [17, 54], showing antibunching at zero delay time $g^2(0) \ll 0.5$ - a clear signature of single-photon emission (see Fig. 1.5a,b). The idea of a monolayer-WSe_2-based LED has also been proposed [57]. AFM nano-indentation is another way to achieve exciton localization [56], as shown in Figure 1.5d.
A different approach consists in modifying the band of the 2D material by generating defects bombarding it with a focused helium ion beam (He-FIB) [55] (see Fig. 1.5c). These precisely positioned and scalable

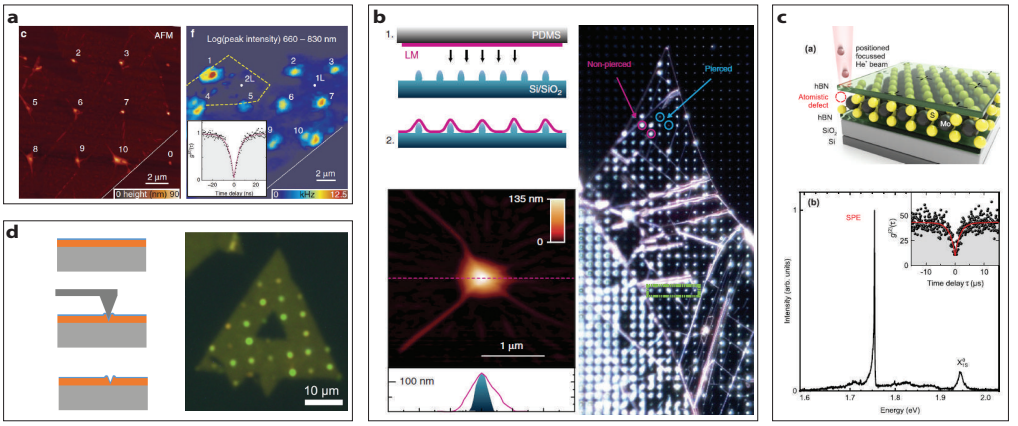

Figure 1.5: Engineering single-photon emitters in 2D materials. Strain induced photoluminescence in TMDs by deposition over pillars pre-lithographed on the substrate (**a**, **b**) or AFM nano-indentation (**d**). **c:** Defect generation in MoS_2 by irradiation with helium focused ion beam. Panels adapted from: **a:** Ref. [54]; **b:** Ref. [17]; **c:** Ref. [55]; **d:** Ref. [56].

single-photon emitters also show antibunching at zero delay time. Although the idea of having SPSs directly embedded in a 2-dimensional electronic platform is very appealing and has shown interesting results so far, these single-photon emitters still have performances below other solid state emitters in terms of linewidth ($\Gamma/2\pi \sim 40$ GHz [17]), emission intensity ($I \sim 10^3$ counts/s [54]) and anticorrelation at zero delay time ($g^2(0) \sim 0.2$ [55]).

1.3 Thesis guide

In this thesis, we will present a novel approach to explore near-field effects, by combining ultranarrow linewidth quantum emitters with 2-dimensional materials. In this way, we can exploit the unique properties of both building blocks of our hybrid devices to achieve electrical tuning of quantum emission, deterministic positioning of SPSs for guiding and enhancing emission and sensing of the 2D material's electrical behaviour. The thesis is organized in the following way:

Chapter 2

Introduction of single molecules' properties and of the experimental setup built to excite them and collect their emission, centered around a custom-built confocal microscope at cryogenic temperatures. Superlocalization of single spectrally selected molecules is also presented.

Chapter 3

Fabrication of hybrid devices made of single molecules and 2D materials. From the synthesis of nanocrystals doped with ultranarrow linewidth emitters, to exfoliation and transfer of 2D materials. Results on deterministic positioning of 3D structures aligned on the quantum emitters' position via electron beam lithography are shown.

Chapter 4

Hybrid devices where the 2D material is exploited as a transparent, non-invasive electrode to show tuning of the molecules' emission energy by the Stark shift over a large range. Dynamical modulation of the emission is also performed, revealing interesting properties on the 2D electrode used.

Chapter 5

Doped nanocrystals on top a graphene field-effect transistor reveal strong anomalies in their Stark shifted emission at the edge of the graphene device compared to the centre. Saturation of defect states at the edge of graphene is hypothesized and an electrostatic model of such scenario shows good agreement with the experimental data.

Chapter 2

Optics of quantum emitters

The study of a hybrid device combining 2D materials with quantum emitters requires being able to isolate and study single nano-objects. Working with solid state single-photons sources such as single molecules, it's crucial to single out the signal coming from the quantum emitters within the overall device response. Optically addressing single molecules requires to work at cryogenic temperatures to reduce perturbations coming from the environment as well as an experimental setup able to spatially and spectrally select single emitters.
In this chapter, we will present the experimental setup and techniques used to excite and characterize our devices. We will show how the spatial and spectral selection allowed by our experimental technique enables us to locate single molecules in the same nanocrystal with a resolution below 50 nm at 3 K.

2.1 Solid state single-photon sources

The use and uptake of photonic technologies has hugely increased in recent decades and they now play a central role in our everyday life. Since the 1960s, lasers have provided a classical source of light and have become more advanced and affordable over the years. Yet, the fast development of quantum technologies have emphasized the need of non-classical sources of light. Single photon emitters (SPEs) guarantee that no more than one photon is emitted at a time and that the photons are indistinguishable. These type of on-demand quantum light sources are a key element for scalable quantum information technology [58], quantum

computing [59], secure communication [60] and metrology [61].
Over the years, different approaches have been developed to produce single photons. Atom transitions at cryogenic temperatures produce on-demand photons but often require complex setups and long measurement times. A promising alternative that has established itself in recent years is the one of solid state single photons emitters [4], atom-like emitters that can be described as two-level systems. Among these SPSs we find fluorescent atomic defects, quantum dots (QDs), carbon nanotubes (CNTs), SPSs in 2D materials, organic molecules. These systems present good photophysical properties and are convenient for scalable integration.

2.1.1 Fluorescent organic molecules at cryogenic temperature

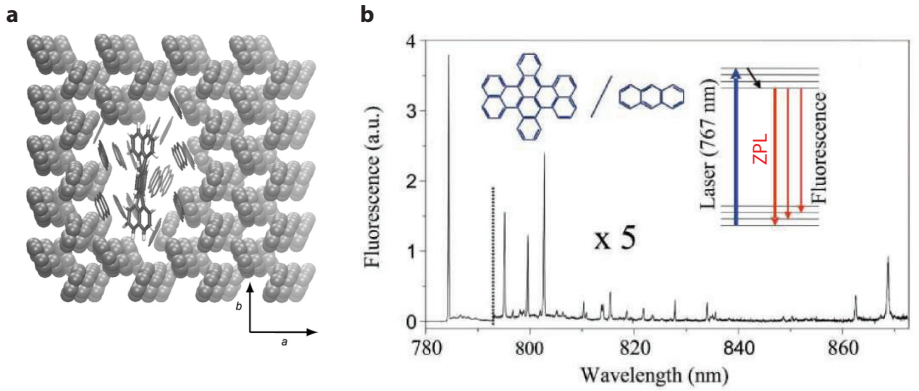

Figure 2.1: Single fluorescent molecules in an anthracene (Ac) matrix. **a:** View of the molecular models of DBT in one of the two main insertion sites in anthracene. The crystallographic axes "a" and "b" are indicated with arrows. Adapted from Ref. [18]. **b:** Low temperature emission spectrum of a DBT molecule with an intense, narrow zero-phonon line (ZPL) peak, vibrational fluorescence lines and phonon sideband. Adapted from Ref. [62].

Solid state photon sources combine atom-like optical properties with the scalability offered by the solid-state host system. Yet, these SPSs suffer the effect of their environment, causing inhomogeneous distributions and distinguishability between emitters [4].
The organic system composed by dibenzoterrylene (DBT) in an anthracene (Ac) matrix is one of the most attractive candidates among

the solid-state SPSs available today. DBT is a centrosymmetric molecule with two main insertion sites in the Ac crystal (see Fig. 2.1a), corresponding to the lowest-energy configurations [18]. It has a zero-phonon line (ZPL) transition at 785.1 nm (1.58 eV) and vibronic transitions as shown in Figure 2.1b [62, 63]. The amount of emission into the ZPL transition with respect to the total decay (branching ratio) is around 30 % [64, 65]. At cryogenic temperatures (T < 4 K), the ZPL peak reaches a narrow lifetime-limited linewidth ($\sim$ 30 MHz [18]) with fluorescence rates at saturation up to 1-3 $\cdot$ 10^5 counts/s and is photostable over days. The narrow linewidth at low temperatures allows us to address a single molecule and guarantees a large absorption cross-section.
Organic molecules, first optically measured in 1989 [66, 67] have confirmed themselves as bright and stable SPSs both at room [68, 69] and at cryogenic temperatures [62].

2.1.2 Resonant excitation of a two-level system

The Jablonski diagram in Figure 2.2a represents the energy levels of a DBT molecule in one of the main insertion sites of an Ac crystal at low temperature. The electronic ground state $|S_0\rangle$ is occupied by two electrons with antiparallel spins (singlet state). Resonant excitation at 785 nm (red arrow) allows us to excite one electron to the pure electronic excited state $|S_1\rangle$. At room temperature, off-resonant excitation (yellow arrow) is more commonly used since it allows to populate the whole vibronic bands of the electronic excited states ($|S_{i,\nu\neq 0}\rangle$), leading to higher emission rates. In this configuration, the excited electron decays first to lower vibronic bands or electronic levels via non-radiative vibrational relaxation.
Once prepared in the $|S_{1,\nu=0}\rangle$ excited state, two decay channels are possible for the molecule: fluorescence and intersystem crossing (ISC). Fluorescence (in solid red line in Fig. 2.2a) is the radiative transition corresponding to the relaxation of the excited electron to the electronic ground state (zero-phonon line, ZPL) or the vibronic bands. ISC (in dashed black line) corresponds to the transition from the singlet $|S_1\rangle$ to the triplet $|T_1\rangle$ excited state. This transition is spin-forbidden due to selection rules and therefore with low probability.

In our laser spectroscopy measurements we excite the system at resonance ($\hbar\omega_{exc.} = 1.58$ eV). When the electron relaxes back to the ground state, the system decays radiatively at the same energy as the excitation.

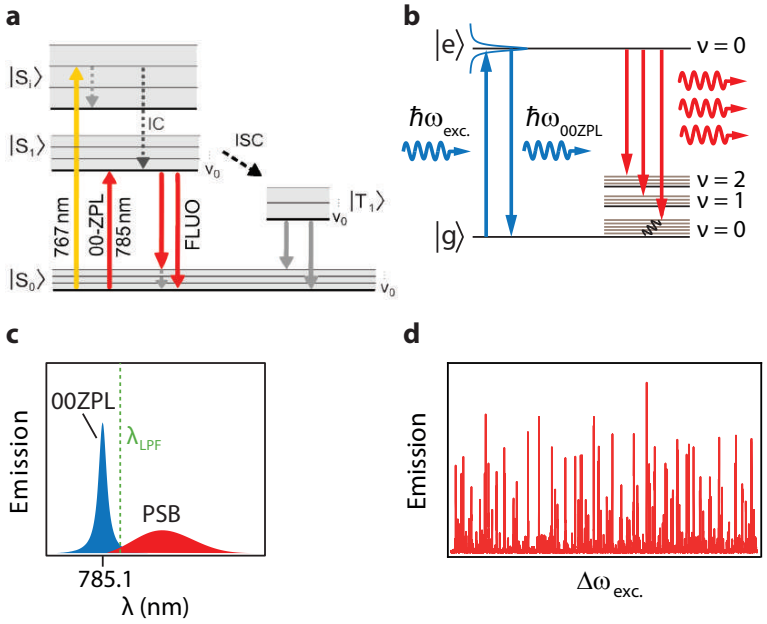

Figure 2.2: Excitation of single molecules. **a:** Jablonski diagram of a DBT:Ac guest-host system. Solid lines represent radiative transitions while dashed lines show non-radiative transitions. Adapted from Ref. [70]. **b:** Sketch of resonant excitation and emission of a two-level system. **c:** Emission spectrum of a single molecule showing the zero-phonon line and phonon sideband. **d:** Typical spectrum showing a forest of peaks corresponding to single molecules in the same nanocrystals (number of molecules $n < 100$).

This transition (00ZPL) (shown in blue in the sketch of Fig. 2.2b) is the strongest that the molecule experiences and is represented by the blue peak in Figure 2.2c. One electron in the excited state can also decay to the vibronic states of the electronic ground level (in red in Fig. 2.2b), contributing to the phonon sideband (PSB) (red peak in Fig. 2.2c). Other transitions can be excited at higher frequencies like the 01ZPL, 02ZPL, etc..., between the $\nu = 0$ vibrational level of the ground electronic state and the $\nu = 0$ vibrational level of the second, third, etc..., excited electronic states, but we will ignore them in this work.
As we use a longpass filter (at wavelength λ_{LPF}) to exclude the laser excitation from our detection, therefore we are always measuring the PSB transition. Figure 2.2d shows the typical spectrum obtained by performing laser spectroscopy of one anthracene crystal doped with DBT molecules, as it will be discussed in Section 2.3.1. Each peak shows the

emission of one molecule in the NC.

2.1.3 Temperature broadening and saturation with power

Single-photon sources are damped by the loss of photons and by dephasing of the transition dipole caused by coupling to environmental fluctuations. As a result, the total decay rate Γ has to take into account both Γ_1 and Γ_2, the population decay rate and the dephasing rate (or decay rate of the transition dipole) respectively. $\Gamma_1 = 1/T_1$, where T_1 is the lifetime, while $\Gamma_2 = 1/T_2 = \Gamma_1/2$ with T_2 the coherence time of the system. Using this formalism, the linewidth becomes $\Delta\nu = \Gamma_2/\pi \cdot \sqrt{1+S}$ [71].
Organic molecules are protected by their host matrix from lattice phonons and dephasing can be minimized by working at cryogenic temperature ($T \leq 4$ K).

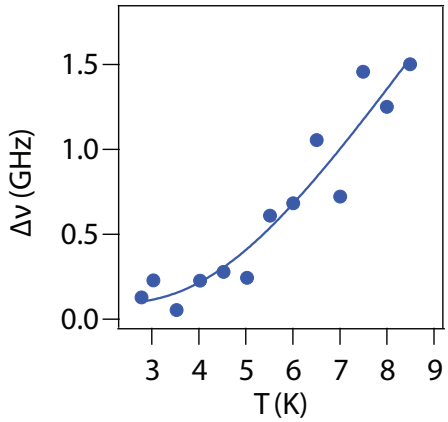

Figure 2.3: Temperature dependence of the emission linewidth at low excitation power (10 nW). Adapted from Figure 6.7 of Ref. [5].

Single molecules are extremely sensitive to their environment, meaning we have to verify that our measurement technique is performed in the optimal conditions and doesn't affect the properties of the emitter. We investigate the effects of temperature and excitation power on the molecules.
First, we consider the impact of the cryostat temperature on the linewidth. Starting from the lowest temperature reached by our cryostat (2.8 K), we measure the same molecule's linewidth as a function of the increasing

temperature, at a low excitation power of 10 nW. Figure 2.3 shows a fast linewidth broadening with temperature, following the Arrhenius law [18]:

$$\Delta\nu(T) = \Delta\nu_0 + A\ exp\left(\frac{-E_a}{k_B T}\right) \tag{2.1}$$

where $\Delta\nu_0$ is the lifetime-limited linewidth, A is a constant, E_a is the energy of activation of the local phonons inducing broadening by dephasing of the optical dipole [71], k_B is the Boltzmann constant. From the fit with Equation 2.1, we find an activation energy $E_a = 2.5$ meV which is in agreement with previous results obtained with similar guest-host molecular systems [72]. Figure 2.3 confirms the importance of working at low temperature with single molecules, to access their intrinsic linewidths. With our cryostat we reach the lowest temperature of 2.8 K, which means that the smallest linewidth we are able to observe is $\Delta\nu$ (2.8 K) = 1.1 $\Delta\nu_0$, forcing us to consider an error of 10 % in our observable linewidths compared to the intrinsic ones.

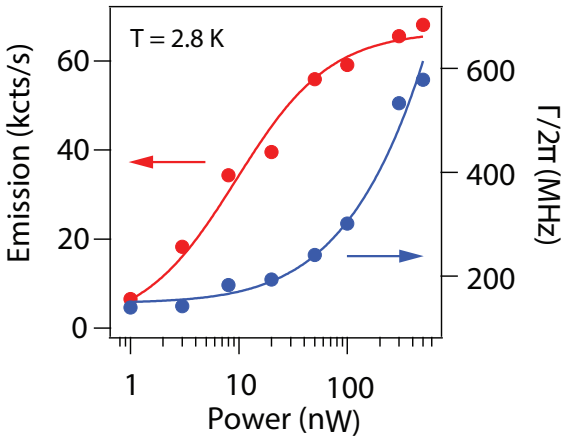

Figure 2.4: Linewidth (in blue) and emission strength (in red) dependence from the excitation power. Solid lines are fits to the data as described in the main text. Adapted from Figure 6.7 of Ref. [5].

Then, we study the effect of the excitation power on the on-resonance emission rate and single molecule's linewidth at 2.8 K. From Figure 2.4 we see a significant increase in linewidth (in blue) and emission saturation (in red) with the excitation power. The linewidth is expressed as $\Gamma/2\pi$, where Γ is the total decay rate of the molecule. The behaviour of the

emission rate - that is the radiative decay rate for lifetime-limited emitters - $\Gamma_{rad}(I)$ and of the single molecule total decay rate $\Gamma(I)$ as a function of the intensity I is given by [73, 74]:

$$\Gamma_{rad}(I) = \Gamma_{rad,sat}\left[\frac{I/I_{sat}}{1+I/I_{sat}}\right] \tag{2.2}$$

$$\Gamma(I) = \Gamma_{sat}\left[1+(I/I_{sat})\right]^{1/2} \tag{2.3}$$

where $\Gamma_{rad,sat}$, I_{sat} and Γ_{sat} are the radiative emission rate, intensity and total decay rate at saturation. The intensity at saturation is defined as $I_{sat} = \frac{\hbar\omega}{2\sigma\tau} = \frac{P_{sat}}{\sigma}$. σ is the absorption cross section, τ is the excited state lifetime and P_{sat} is the saturation power. Fitting the data in Fig. 2.4 with Equations 2.2 and 2.3 respectively we get $P_{sat} \sim 20$ nW (corresponding to a saturation intensity $I_{sat} \sim 10$ W $\cdot$ cm^{-2} and radiative emission rate saturation $\Gamma_{rad,sat} \sim 70$ kcts/s). These results highlight the need to use low excitation powers, typically of 5-10 nW, to avoid the emission saturation regime and linewidth broadening.

2.1.4 Anticorrelated single photons

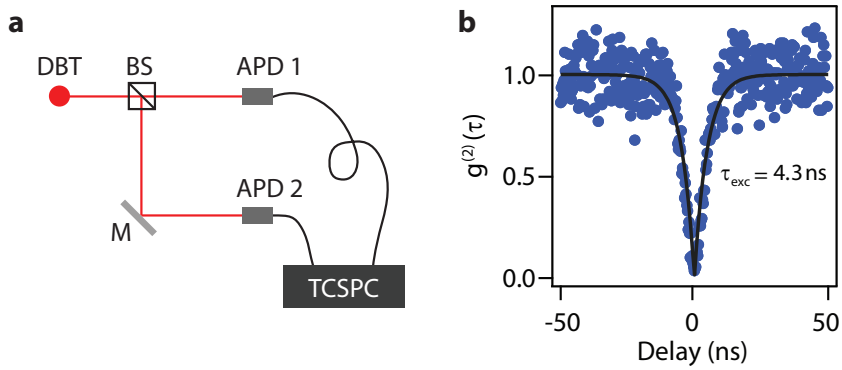

Figure 2.5: Photon antibunching measurement. **a:** Sketch of the Hanbury-Brown-Twiss configuration. **b:** Photon time correlation measurement, showing $g^{(2)}(0) < 0.5$ for a single molecule. The black line is the fit of the data as explained in the main text.

To understand the nature of a light source we have to perform photon time correlation measurement, which allows us to distinguish between thermal, coherent and anticorrelated photons. The three regimes

have very different photon statistics. Thermal light is characterized by bunched photons traveling in "packets" while coherent light sources emit independent photons, with a finite probability of emitting two photons at the same time. Only antibunching guarantees that the light source is generating anticorrelated photons, hence that just one photon is emitted at a time $< \tau_{exc.}$, with $\tau_{exc.}$ the excited state lifetime defined as $\tau_{exc.} = \frac{1}{\Gamma_{rad}+\Gamma_{nrad}}$ where Γ_{rad} and Γ_{nrad} are the radiative and non radiative linewidths of the molecules respectively.
The Hanbury-Brown-Twiss (HBT) experiment [75] allows us to measure time correlation between photons. A sketch of the measurement procedure is shown in Figure 2.5a: photons emitted by a DBT molecule are divided by a 50:50 beam splitter (BS) into two identical arms and guided by mirrors (M) towards two avalanche photo diodes (APDs) for detection. The occurrence of a photon being measured by one of the APDs is noticed by a time-correlated single photon counting (TCSPC), which generates a coincidence histogram as a function of the time delay between the events detected by the APDs.
Figure 2.5b shows the result of the time correlation measurement for a single molecule. Since we are in the limit of short inter-photon times (< 100 ns), the histogram collected by the TCSPC follows the second-order correlation function as a function of the intensity [76]:

$$g^{(2)}(\tau) = \frac{\langle I(t)I(t+\tau)\rangle}{\langle I(t)\rangle^2} \tag{2.4}$$

where τ is the delay time between the two channels of the TCSPC and $I(t)$ is the photon rate at time t. The clear antibunching [77] appearing in the autocorrelation measurement confirms the non-classical nature of our SPSs. Ideally, a quantum source of light should have $g^{(2)}(0) = 0$ but this value increases experimentally due to multi-photon emission and noise, hence we define a single-photon source as having $g^{(2)}(0) \ll 0.5$. When $g^{(2)}(0) \to 0$ the probability to get multi-photon events decreases. We fit the correlation measurement with a second-order correlation function defined as [71]:

$$g^{(2)}(\tau) = 1 - \frac{p+q}{2q}\, e^{-\frac{1}{2}(p-q)\tau} + \frac{p-q}{2q}\, e^{-\frac{1}{2}(p+q)\tau} \tag{2.5}$$

where $p = \Gamma_1 + \Gamma_2$, $q = \sqrt{(\Gamma_1 - \Gamma_2)^2 - 4\Omega^2}$ and τ is the delay time. Ω is the Rabi frequency related to the saturation parameter $S = I/I_{sat}$

according to the relation: $S = \Omega^2/(\Gamma_1\Gamma_2)$. We extract the DBT excited state lifetime $\tau_{exc.}$ = 4.3 ns. The corresponding intrinsic linewidth is $\Gamma_0/2\pi = 1/\tau_{exc.}$ = 37 MHz, in agreement with values of linewidth in bulk crystals [62].
Photon antibunching is an essential requirement for our study as it guarantees that only one photon is emitted within a time smaller than the excited state lifetime and it ensures that we are addressing only one single molecule.

2.2 Experimental setup

Excitation of single molecules and collection of single photons, as well as detection of the optical end electric response of 2D materials, are some of the key aspects of investigation of our hybrid quantum emitters - 2D materials devices. Probing and isolating single nano-elements of the hybrid device is a challenging part of our measurements. We optically excite and then measure optical reflection or fluorescence from single molecules and 2D materials. Tuning can also be performed electrically. A setup with good spatial and spectral resolution allows us to address single nano-components within the device.
In this chapter, we will present the experimental setup and techniques used to collect the results presented in this thesis, focusing on the custom-made cryogenic temperature scanning confocal microscope which is at the centre of our single-photon detection.

2.2.1 Confocal microscopy at cryogenic temperature to investigate in situ emission properties

A necessary step when working with ultra-narrow linewidth emitters is to work at low temperatures to reduce thermal fluctuations from the environment, allowing us to address the intrinsic properties of the two-level systems.

For cryogenic cooling we use a closed-cycle optical cryostat (Montana Instruments Cryostation), shown in Figure 2.6a, which can reach temperatures as low as 2.8 K. The sample is mounted inside the chamber via a metal printed circuit board (PCB), connected to the cold finger for temperature stability (see Fig. 2.6b). A series of pins connect the PCB to the exterior for electrical control (see Fig. 2.6c). Both the cold finger and

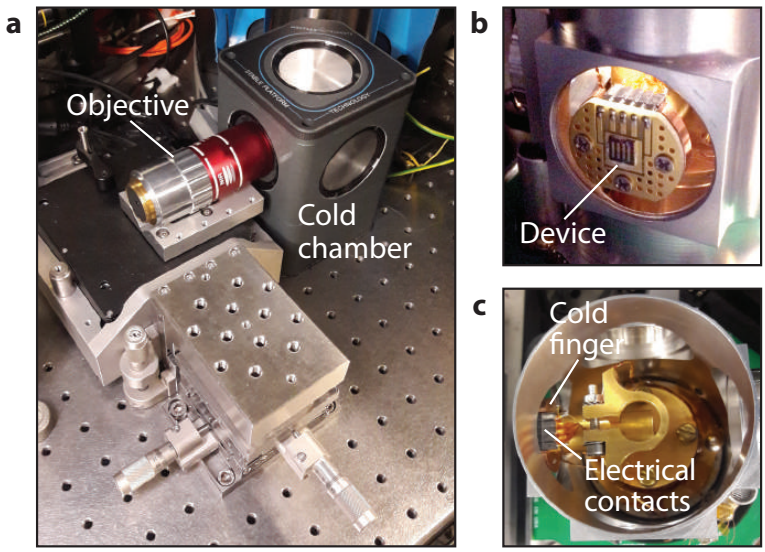

Figure 2.6: Cryogenic cooling system. **a:** Exterior of the cold chamber. The objective is positioned at the optical entrance of the cryostat. **b:** Device mounted on the cold finger via a printed circuit board (PCB). **c:** PCB contacted via a jumper of electrical pins.

the radiation shield are set to ground to avoid stray electric fields. The chamber is optically accessible by a small optical window. Before cooling down the sample, the air from the chamber is evacuated using a turbo-molecular pump which enables reaching a vacuum of approximately $7 \cdot 10^{-6}$ mbar. The system is designed in order to isolate the sample on the cold finger from mechanical vibrations coming from the pump and other external sources. Experimentally, we observe a sample drift below 1 μm/day in the three directions.

In order to isolate the signal of SPSs from the background, a confocal microscope configuration [78, 79] is used. This results in spatial confinement of the excitation and detection to a small volume. A point-like illumination spot is obtained using a high numerical aperture objective and is combined with a point-like detection, obtained using a single-mode fiber (diameter of the order of μm), fiber-coupled to an avalanche photodiode (APD) in order to reach high spatial sensitivity. Spectral filtering combined with scanning confocal microscopy allows us to obtain 2D optical reflection and fluorescence maps with very low background. The sketch in Fig. 2.7 shows the confocal setup for excitation, reflection and fluorescence collection. The continuous wave (CW) laser used is a

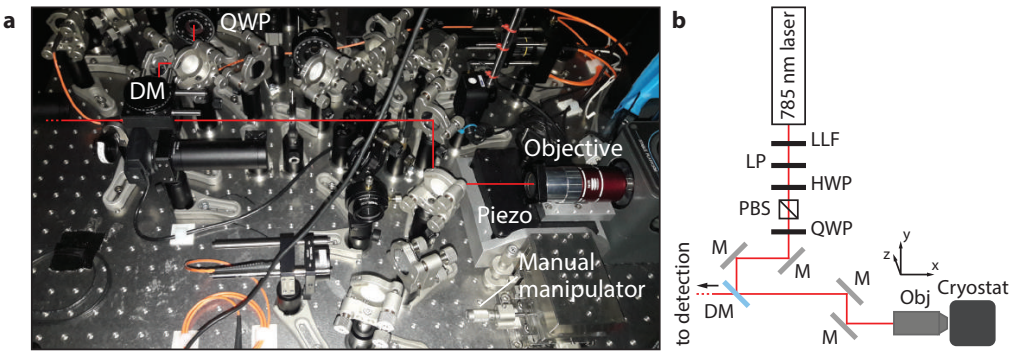

Figure 2.7: Photo (**a**) and sketch (**b**) of our custom-made confocal microscope.

785 nm diode laser (Toptica DL 100 DFB). The collimated beam passes through a laser line filter (LLF, Semrock MaxLine). It is a pass-band filter centred at 785 nm with an optical density (OD) > 6, suppressing the signal outside a narrow bandwidth of 2 nm for spectral cleaning. Then the beam passes through a linear polariser (LP) to fix the polarisation along a single axis. A computer-controlled half-wave plate (HWP) is used to rotate the polarisation angle with respect to a polarising beam-splitter (PBS). This allows us to change the amount of light transmitted, and hence control the excitation power (power range $\sim 10^3$). After the PBS, a quarter-wave plate (QWP) transforms the linear polarisation into circular. Then, a dichroic mirror (DM) reflects the beam towards two mirrors which guide it into the objective. We focus the excitation light into the cryostat with a long (10 mm) working distance microscope objective (100x Mitutoyo Plan Apo NIR HR Infinity Corrected) with a numerical aperture N.A. = 0.7 and transmission approximately 60-80 %. A plane-wave enters the back aperture of the objective (beam diameter $\simeq$ back aperture of the objective = 3 mm) and is focused at its focal point. The objective is mounted on a computer-controlled 3D piezo stage for focusing and fine scanning, while manual manipulators are used for rough positioning.

2.2.2 Single photon detection for quantum photonics

A sketch of the single photon detection is shown in Figure 2.8. An important part of the detection consists of spectral filtering the beam to isolate the emission signal from the quantum emitters. Proper spectral filtering enables us to relax the conditions on spatial filtering at the detection level, that is to use multi-mode fibers for light collection for higher emission

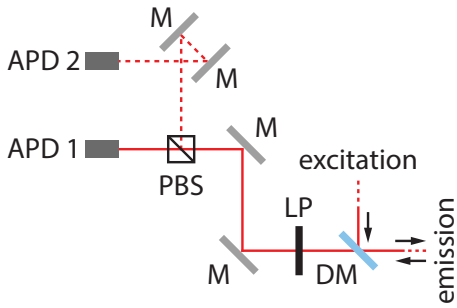

Figure 2.8: Sketch of our single photon detection setup.

count rates. The first step of spectral filtering is the narrowband laser line filter (LLF) used at excitation, as previously discussed. Then, emission from single molecules passes through a dichroic mirror (DM, Semrock LPD01-785RU) which reflects the excitation with reflectivity $\sim$ 99% and passes longer wavelengths. Finally, right before detection, a longpass filter (LPF, Semrock LP02-785RU) removes any residual excitation light (OD $\sim$ 6.5 for $\lambda < 785$ nm).
After spectral filtering, the emission is collected by a multi-mode fiber (diameter 100 μm) via a 10x Olympus objective and is fiber-coupled to an avalanche photo diode (APD, Perkin-Elmer SPCM AQRH 14 FC) in single photon counting mode. The APD produces an electrical pulse every time a single photon is detected. These pulses are then averaged by the counter module of the data acquisition card (DAQ, National Instruments PCI-6230) used for the measurement, resulting in a signal in counts/s. Measured dark count rate is $\sim$ 500 counts/s. The APD's dead time is 50 ns and the output length is 35 ns, which implies that APDs can only detect one photon every 85 ns. This timescale is more than enough to resolve the emission of a single molecule well below the APD saturation.

2.2.3 Room temperature setup for fluorescence imaging

In order to rapidly localize emitters in a device without needing to cool it down in the cryostat (for example in-between fabrication steps), we built a wide-field excitation and imaging system combined with spectral filtering which provides 2D reflection and fluorescence maps of big areas of the sample at room temperature.
A wide-field off-resonant excitation (see Fig. 2.9a) is used to illuminate many emitters at the same time, by shining a 730 nm light emitting

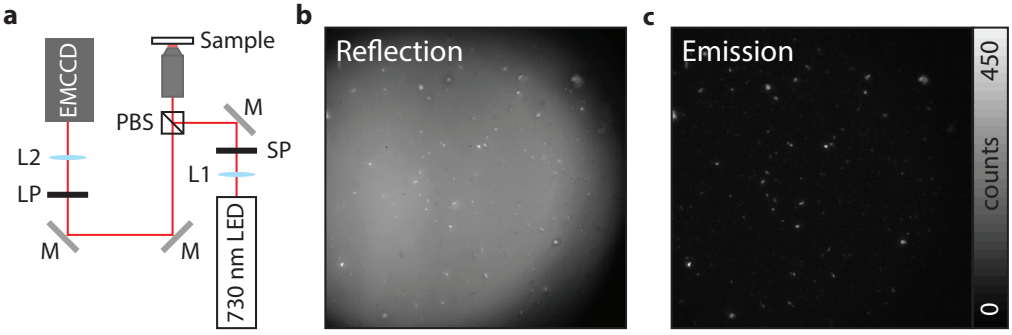

Figure 2.9: Wide-field off-resonant imaging setup at room temperature (RT). **a:** Sketch of the RT setup for optical reflection and fluorescence detection. Reflection (**b**) and fluorescent emission (**c**) images of DBT-doped nanocrystals embedded in a PVA layer.

diode (LED) (Opulent Far Red 720-740 nm) [80]. The LED light is first collimated by a lens (L1), then it is filtered with a shortpass filter (SP) cutting-off wavelengths < 750 nm, to attenuate excitation light at the DBT resonance (785 nm). The beam is then focused onto the back focal plane of the objective (input power $\sim$ 1 mW) by a second lens (L2), allowing to illuminate a big area of the sample (diameter $\sim$ 100 μm). The reflected light/fluorescence is guided back to a highly sensitive EMCCD camera. A longpass filter (LP) strongly suppress wavelengths smaller than 785 nm disclosing the fluorescent nanocrystals (Figure 2.9c), while reflection (Figure 2.9b) is collected with no spectral filtering.

2.3 Spectroscopy of single emitters

For studying the effects of the environment on a single molecule, which is essential when exploring coupling effects in hybrid devices, we need to have access to it's energy and emission linewidth. Traditional spectroscopy cannot fulfill this job since molecules are usually hard to isolate because they are densely distributed within a nanocrystal and they have a linewidth $\Gamma \sim 50$ MHz $\equiv 0.1$ pm which is much smaller than our spectrometer resolution (0.1 nm).
Spectral resolution is then given by a scanning laser spectroscopy (SLS) technique which allows us to address single molecules in an ensemble within the same illumination spot, as it will be further discussed in this section.

2.3.1 Scanning laser spectroscopy

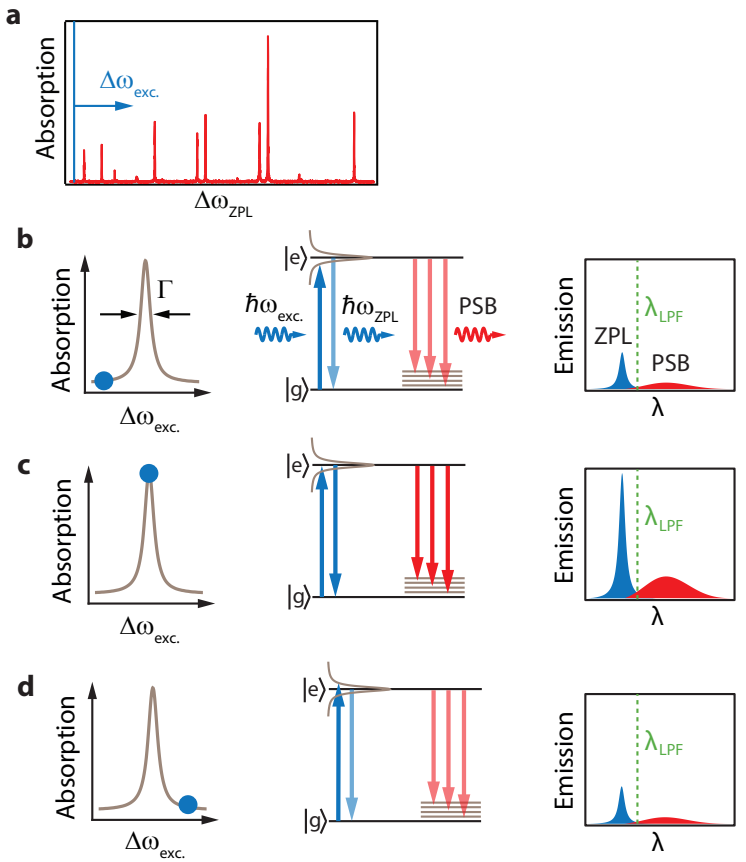

Figure 2.10: Scanning laser spectroscopy of single emitters. **a:** A tunable laser with narrow linewidth is scanned across a single molecule's absorption resonance, as shown in details in **b-d**. The emission spectrum of the molecule shows the 00ZPL and PSB emission. A longpass filter (LPF) is used to suppress resonant excitation, hence only off-resonant detection is performed. Adapted from Ref. [5].

Single emitter spectroscopy is performed by scanning the energy of a tunable laser with narrow linewidth ($\Gamma_{laser} \sim 1$ MHz $\ll \Gamma_{DBT} \sim 50$ MHz) across the Lorentzian absorption resonance (00ZPL) while collecting the off-resonance emission into the PSB [74] (see Figure 2.10a). In order to do so, it's necessary for the ensemble of molecules within the nanocrystal to be broadly spectrally distributed and for the laser to be stable and fine-tunable over a big range. DBT molecules at cryogenic temperatures

fulfill these conditions thanks to their narrow linewidth, inhomogeneous broadening ($\Delta\omega_{ensemble}/2\pi$ > 200 GHz - 1 THz) and approximately 100 molecules contained in a nanocrystal.
As shown in Figures 2.10b-d, we excite each molecule on-resonance with the 00ZPL ($\omega_{exc.} = \omega_{00ZPL}$). The molecule emits into the 00ZPL transition and the phonon sideband as discussed in Section 2.1.2. Experimentally, a LPF is used to suppress the resonant excitation and therefore the 00ZPL, thus we only collect the PSB.

2.3.2 Excitation of an inhomogeneous broadened DBT ensemble

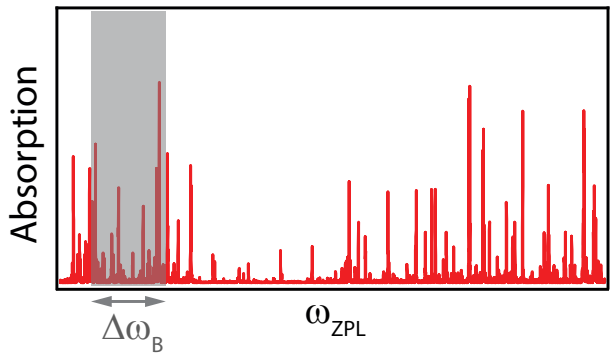

Figure 2.11: The excitation energy of the laser is artificially broaden to excite at same time multiple molecules within the illumination spot. Adapted from Ref. [5].

Locating nanocrystals containing fluorescent molecules at cryogenic temperatures requires us to detect spatial emission maps. In order to do so, we need to artificially broaden the excitation energy of the laser (Γ_{laser} < 1 MHz) over a frequency range $\Delta\omega_B/2\pi$ broad enough to simultaneously excite many molecules within the same excitation spot, as sketched in Figure 2.11. The pseudo-broadband excitation is obtained by modulating the diode laser current at frequency f = 200 Hz (faster than the APD measurement frequency $1/\tau_{APD} \sim$ 50-100 Hz) using a waveform generator. This leads to an artificial broadening of $\Delta\omega_B/2\pi \sim$ 100 GHz, approximately 1/10 of the typical inhomogeneous broadening of the molecules in the nanocrystal.

2.4 Superlocalization of single molecules

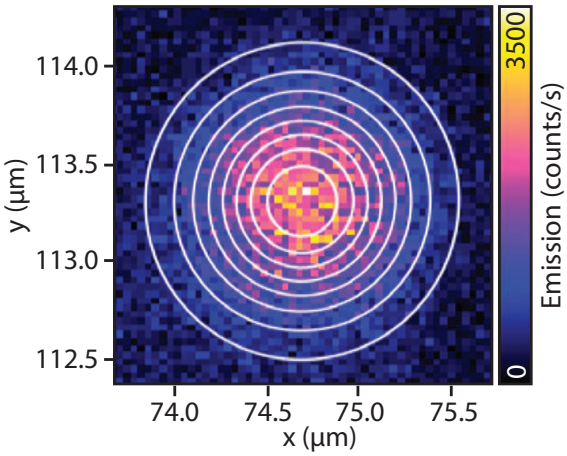

Figure 2.12: Intensity distribution of the image spot of a single molecule excited resonantly. White lines show Gaussian fit, as discussed in text.

The diffraction limit of a microscope is the main bottleneck when optically studying single emitters with nanometer spatial resolution. This is a big issue for studying near-field effects, for which knowing the exact position of a single molecule with respect to its environment is a very valuable information.
Different approaches have been developed to tackle this issue with solid state SPSs. The spontaneous exciton localization in carbon nanotubes at low temperature has been studied using a hyperspectral imaging technique [81]. In order to determine the position of semiconductor quantum dots, the high sensitivity of their emission frequency to local stress is exploited [82]. With NVCs, their photoluminescence blinking is used to identify them with a sub-20 nanometer resolution [83].

In the case of single molecules, since two point-like emitters are almost never identical due to their different environments, we can always spectrally distinguish them regardless of their separation [74, 84]. Interesting results have been achieved by applying an inhomogeneous electric field using a scanning probe electrode to identify different narrow-linewidth molecules via Stark shift [85] with nanometer resolution and to manipulate their dipole-dipole coupling [12]. We use a different approach, based on analyzing the intensity distribution of the image spots to locate the position of each emitter, also known as superlocalization.

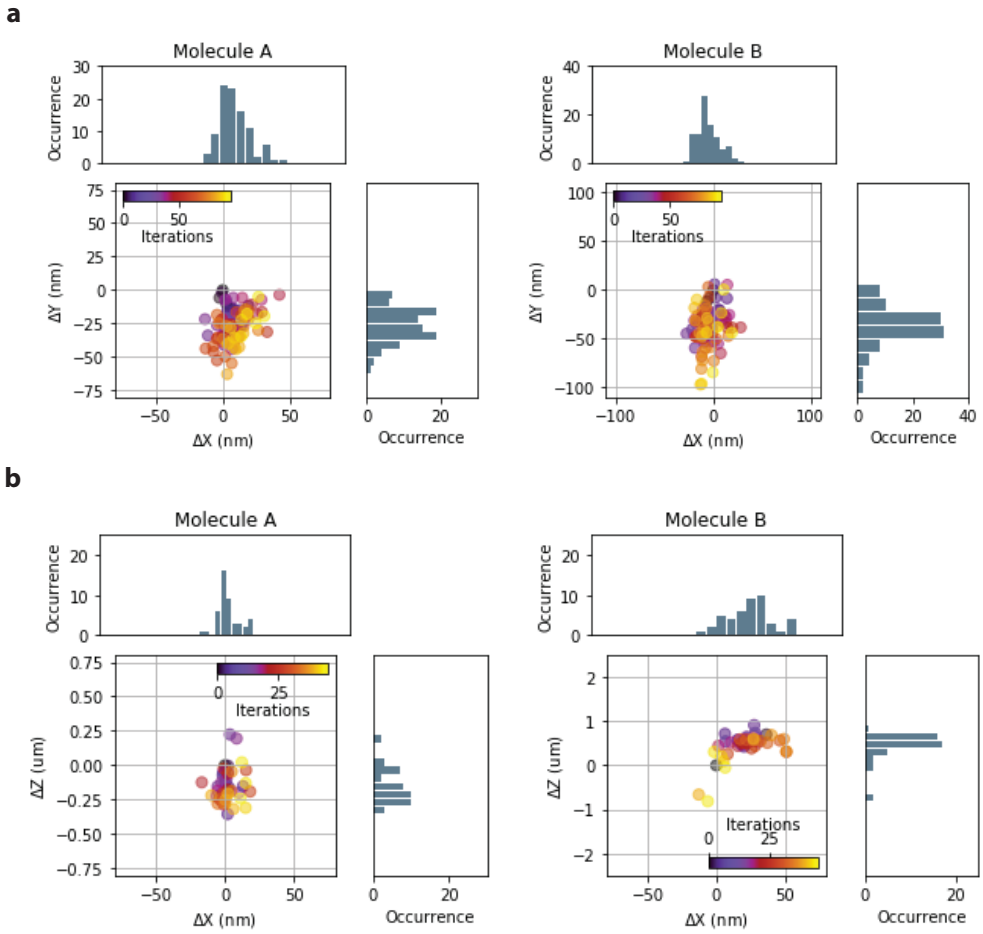

Figure 2.13: Positions in the x-y (**a**) and x-z plane (**b**) of two molecules (A and B) obtained by repeating $\sim$ 100 times the Gaussian fit of the intensity distribution.

In collaboration with Prof. Dr. Michel Orrit (Leiden University) we have been able to localize single molecules within one nanocrystal by spectral selection.First we focus the laser beam at the centre of the NC, then we perform laser spectroscopy as explained in Section 2.3.1. We choose one bright, stable, narrow peak well isolated from the others. We fix the excitation energy at resonance with the chosen peak and run a 2D emission map (for more details see Section 2.3.2) in order to collect the 2D Gaussian image spot, as shown in Figure 2.12.
We analyze the intensity distribution of the image spot by fitting it with

a Gaussian mode to find the x-y position of the maximum, which we assume coincides with the single molecule's position. The measurement and analysis are repeated approximately 100 times to collect statistically valid results on the maximum position.
We are therefore able to locate the center of each emitter with a great lateral accuracy, mainly limited by the signal-to-noise ratio of our measurement. In the x-y plane, the measurements performed on two different molecules (molecule A and B) confirm a position accuracy with an error of $\sim$ 50 nm (see Fig. 2.13a). The error on the z position is higher ($\sim$ 250 nm as shown in Fig. 2.13b), due to the beam waist.

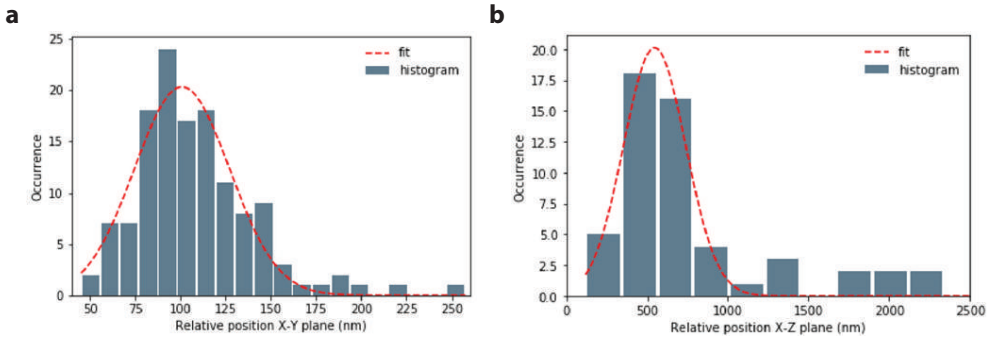

Figure 2.14: Histogram of the distance between molecules A and B in the x-y (**a**) and x-z plane (**b**) and relative Gaussian fit (in red).

We calculate the distance between the two molecules in the x-y and x-z plane. Using the set of positions (x_A, y_A) and (x_B, y_B) obtained by repeating 100 times the measurement of the image spot intensity, we build an histogram of the distance as shown in Figure 2.14a and b for the x-y and x-z plane respectively. We fit the histogram with a Gaussian distribution. It results that we are able to to identify two molecules with a distance 100 ± 37 nm in the x-y plane and 547 ± 272 nm in the x-z plane. This technique allows to spatially locate spectrally selected single molecules with nanometer resolution, allowing us to correlate the spectral properties of SPSs with their position with respect to the environment.

2.5 Conclusions

In this chapter, we introduced the solid state single-photon sources at the centre of this work. DBT molecules show bright, stable, narrow

linewidth emission at cryogenic temperatures. These lifetime-limited quantum sources are therefore sensitive detectors of changes in their environment, a desirable requirement when coupling them to an hybrid device.

We presented the experimental setup used to optically address our hybrid quantum emitters + 2D materials devices, cooled to 2.8 K using a cryogenic system. A custom-built confocal microscope allows us to locally excite fluorescence from DBT molecules and combined with spectral filtering at the single photon detection level secures to ensures single emitters. In addition to that, scanning laser spectroscopy is performed to probe the transition energy and linewidth of single DBT molecules at 2.8 K.

Finally, we showed the experimental technique and analysis developed to perform superlocalization of single molecules within the same illumination spot. Spectral filtering combined with intensity distribution analysis enables to locate molecules with an error as small as 50 nm.

Optics of quantum emitters

- We presented single organic molecules as promising SPSs with bright (1-3 $\cdot 10^5$ counts/s), stable, ultranarrow linewidth ($\Gamma_{DBT} \sim$ 30 MHz at 3 K)
- We highlighted the photophysical properties of single molecules and the need to work at cryogenic temperatures, given that Γ_{DBT}(3.7K) is already twice Γ_{DBT}(0K)
- We discussed the experimental setup used for resonant excitation, optical reflection and off-resonant fluorescence detection
- We described the scanning laser spectroscopy technique to address single molecules in a inhomogeneously broadened ensemble and the spatial collection of emission from several molecules using an artificially broadened laser excitation by fast modulation
- We showed results of superlocalization of single molecules within the same nanocrystal with 50 nm resolution in x-y and 250 nm in the x-z plane

Chapter 3

Fabrication of devices integrating ultra-narrow linewidth quantum emitters with 2D materials

Nanoscale integration of single-photon emitters is a central requirement for the development of hybrid devices combining photon sources with different active nanophotonic elements in order to attain efficient optical and electrical control. Solid-state single photon sources [4] such as quantum dots (QDs) and nitrogen-vacancy centers in diamond (NVCs) have already proven their potential in terms of efficient positioning [86] and localization [87], integration [88], electrical control [89] and mechanical coupling [90]. Our chosen solid-state quantum emitters, Dibenzoterrylene (DBT) molecules in anthracene (Ac) nanocrystals, are bright lifetime-limited single-photon sources (SPSs) with extremely high photostability and narrow emission peaks [91], providing uncorrelated photons at cryogenic temperatures. These SPSs have a high signal to noise ratio which makes them good electric field sensors but at the same time makes them sensitive to modification of their environment. Hence, integration of single organic molecules typically degrades the photostability of the emitter itself. 2D materials provide a non-invasive atomically-thin interface with tuneable electronic properties that can be easily integrated with quantum emitters at the nanoscale to explore near-field effects. Here, we present the fabrication technique developed to obtain high quality single organic molecules in noncrystals and different approaches to integrate them in

a hybrid device in order to explore multiple configurations, such as deterministic positioning via lithography, non-invasive water-based stamp process, capacitive hybrid devices.

3.1 DBT molecules in anthracene nanocrystals for integration at the nanoscale

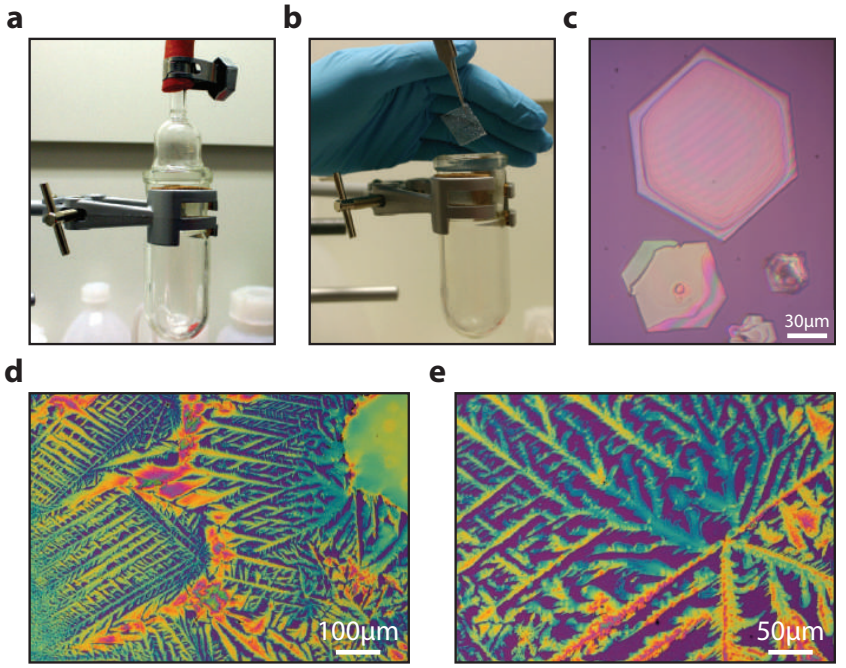

Figure 3.1: Fabrication of anthracene crystals embedding DBT molecules by co-sublimation and spincoating. **a:** For co-sublimation a mixture of DBT and Ac in powder is heated up in a glass pipe at stable nitrogen atmosphere (150 mbar). **b:** A rise in the vapour pressure induces a convective nitrogen flow where small crystals start to grow and later deposit on a coverslide. **c:** Optical microscope image showing the extremely pure crystalline structure, as can be seen from the almost perfect hexagonal shapes (all adapted from [70]). **d:** Optical image - and zoom **(e)** - of spincoated crystals of Ac doped with DBT, showing the typical "fingers" due to the deposition of a DBT:Ac:ACE suspension and immediate spinning at 3000 rpm, ramp 1500 rpm, for 60 seconds.

One of the building blocks of our hybrid devices are DBT-doped anthracene nanocrystals. Historically, anthracene crystals embedding DBT molecules have been fabricated either by sublimation [92, 93] or spincoating [68, 70]. These techniques provide a high quality, stable crystal environment to host DBT moelcules. On the other hand, they either require complex fabrication procedures leading to extremely regular as well as large crystals, with diameter $\sim 10^2 \mu m$ as shown in Figure 3.1a-c, or they imply a fabrication process lacking control on the final position of DBT molecules (Fig. 3.1d,e).
A novel approach consists in fabricating anthracene nanocrystals doped with DBT molecules by reprecipitation technique [94] in water [16] or a water-based solution such as poly(vinyl alcohol) (PVA).

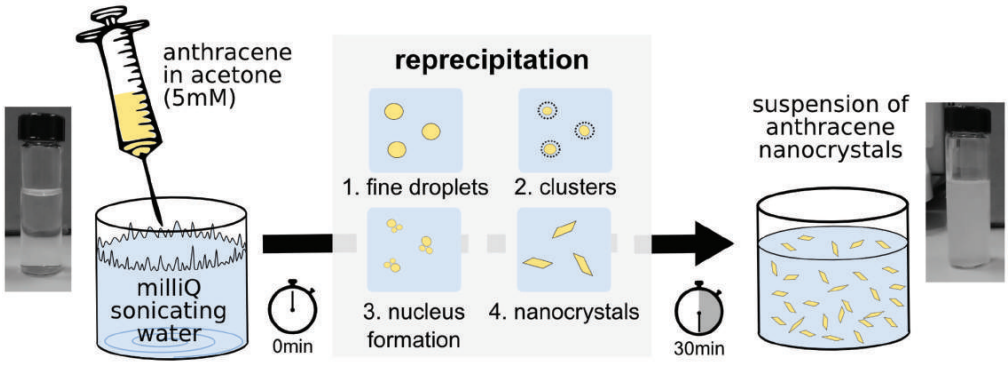

Figure 3.2: Steps of the reprecipitation technique for the formation of DBT-doped Ac NCs in deionized (DI) water or water-based polymers such as PVA. Adapted from [70].

A suspension of DBT and anthracene in acetone (DBT:Ac:ACE, concentration 10 μMol) is prepared by first dissolving 100 mg of anthracene (Sigma-Aldrich) into a bottle with 20 mL of acetone (purity $\geq$ 99.9%, Merck). Then, 100 μL of a solution of DBT (ME20200236 Dibenzoterrylene, Mercachem) dissolved in toluene (standard, Merck) with concentration 2 mMol, are injected. The injection of the DBT:Ac:ACE suspension is performed with a fast shot deep into a vial containing 1mL of deionized (DI) water or PVA (5%/weight), while the vial itself it's sonicating, to garantee a fast and even evaporation of the acetone. While acetone dissolves, micro droplets of DBT:Ac reprecipitate forming nanocrystals, as shown in Figure 3.2. Fig. 3.3 shows nanocrystals made in deionized (DI) water. The suspension is then spin-coated onto a Si^{--}/SiO_2 chip.

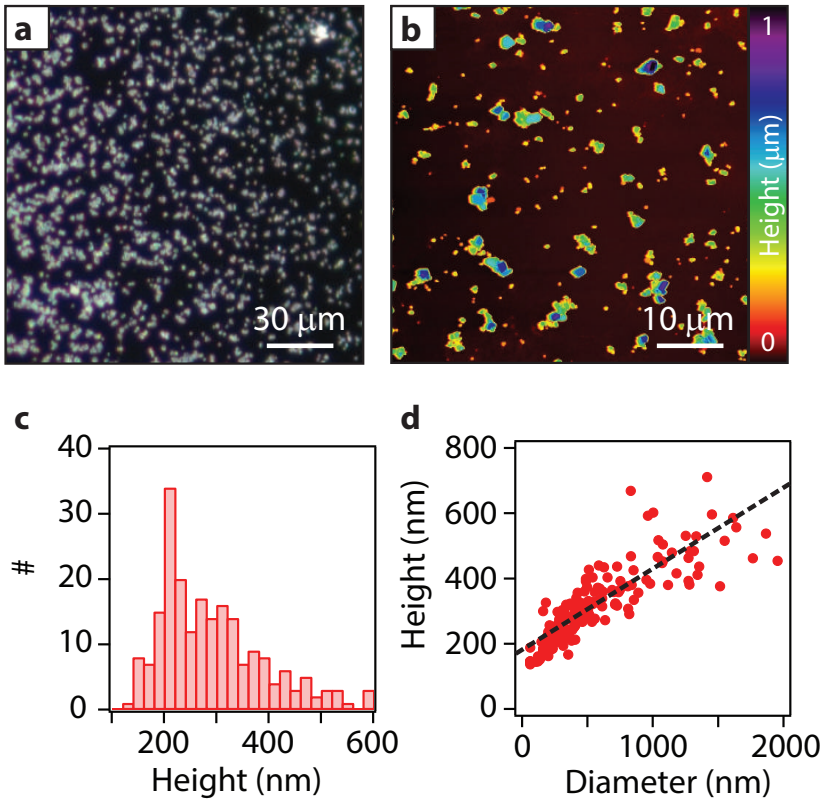

Figure 3.3: DBT-doped anthracene nanocrystals. **a:** Dark-field reflection image of DBT-doped anthracene nanocrystals on a chip. **b:** AFM scan of nanocrystals within an area as shown in **(a)**. **c:** Height distribution of nanocrystals shown in **(b)**. **d:** Aspect ratio of nanocrystals. Here, the height is plotted against an idealized circular diameter extracted from the real particle area as measured in **(b)**. The black dashed line shows the result of the fit suggesting an aspect ratio of height / diameter = 0.25, as discussed in the text.

Upon evaporation of the water, a distribution of nanocrystals is visible in a dark-field optical micrograph (3.3a). An AFM scan of nanocrystals in this distribution is shown in Fig. 3.3b and allows extraction of height (3.3c) and aspect ratio (3.3d) distributions. Typical nanocrystals are approximately 220 nm high and aspect ratio of height h = 170 nm + 0.25 d, where d is the idealised circular nanocrystal diameter obtained from AFM measurements.

3.2 Narrow linewidth quantum emitters in electron beam shaped polymer

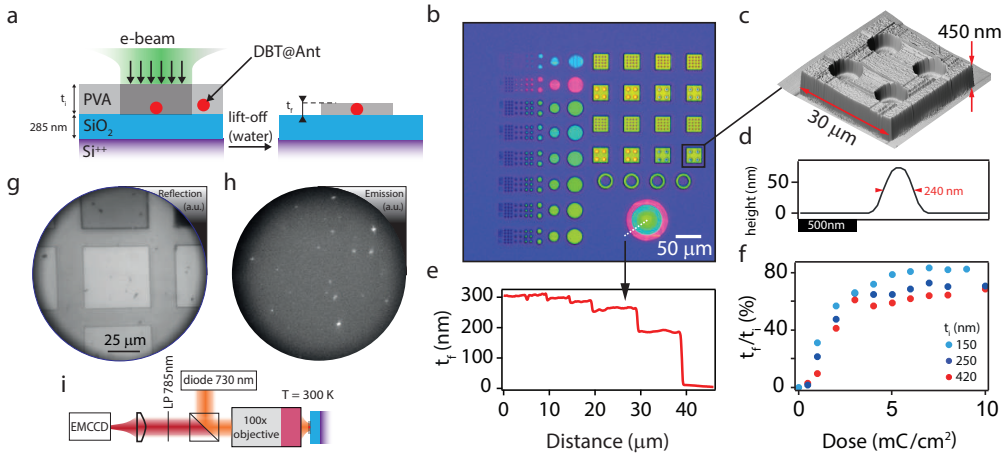

Figure 3.4: Nanostructuring PVA thin films hosting anthracene nanocrystals by electron beam lithography (EBL). **a:** DBT molecules are contained inside anthracene nanocrystals (labelled as DBT@Ant), randomly dispersed in a PVA layer. Zones that are non-exposed to electron-beam are lifted-off in water. Optical **(b)** and atomic force **(c)** micrographs of nano-structured PVA. **d:** AFM profile of a lithographed PVA nano-pillar (not shown in **(b)**). **e:** Height profile of nano-structured PVA measured by atomic force microscopy (dashed line in **(b)**). **f:** Ratio of remaining over initial PVA thickness as a function of EBL dose for three different initial film thicknesses. **g:** Optical reflection at 730 nm of patterned PVA squares and corresponding room temperature DBT emission **(h)**. Squares of different contrasts correspond to exposed areas with various e-beam doses. **i:** Sketch of the room temperature wide field fluorescence imaging setup.

Polymers offer an interesting platform for structuring the environment of SPSs at the nanoscale in order to couple them to photonic structures [25, 95, 96] on chip. While lithography techniques have already shown impressive results for on-chip integration of nitrogen-vacancy centres [97] and quantum dots [98], the outstanding properties of organic single molecules as quantum emitters and their compatibility with polymers motivate the quest for novel approaches based on electron-beam lithography to achieve nanophotonic integration while preserving their emission properties.

Here, the technique based on dibenzoterrylene (DBT) molecules hosted in anthracene nanocrystals fabricated by reprecipitation method [16] is modified to make a suspension of nanocrystals in a polymer instead of water. This suspension of nanocrystals in PVA - termed "doped-PVA" in the following - can be spin-cast on a standard Si^{--}/SiO_2 substrate (Fig. 3.4a). Reference measurements on water-based suspensions show that nanocrystals in such films display typical dimensions ranging from 50 to 500 nm, with a distribution peaked at 230 nm (see Figure 3.3c,d). PVA is a water-based polymer which combines two advantageous properties for nanophotonic integration of quantum emitters: i) it is insoluble in most organic solvents used in nanofabrication and thus protects encapsulated nanocrystals [69] and ii) can be deterministically structured by electron-beam cross-linking [99–101], using water as a developer. Together, these two properties enable the fabrication of three-dimensional structures (Fig. 3.4b,c) which can host and protect quantum emitters.

3.2.1 Nanostructuring PVA thin films by electron beam lithography

This e-beam patterning technique enables extreme lateral nanostructuring. The height difference due to the cross-linking process is appreciable in the change of colour in the exposed structures. In our study, we have realized structures ranging from micron sizes down to 240 nm wide pillars (Fig. 3.4d). Furthermore, complex structures with non-uniform height such as mesas with shallow holes (Fig. 3.4c) and lens-like (Fig. 3.4e) structures can be fabricated by locally varying the electron beam dose, which controls the height of cross-linked structures. For instance, Fig. 3.4e shows the atomic force microscopy (AFM) profile of concentric rings obtained by decreasing the e-beam dose from the centre to the edges.
Measurements on structures fabricated over a large range of doses (1-10 mC/cm^2) show that our technique provides continuous structure height control up to 80% of the initial PVA film thickness, independent of the initial thickness t_i (Fig. 3.4f). The 20% reduction is an effect of the polymer shrinking after cross-linking. These measurements show that electron-beam lithography of PVA enables nanoscale 3D shaping quantum emitter environment.

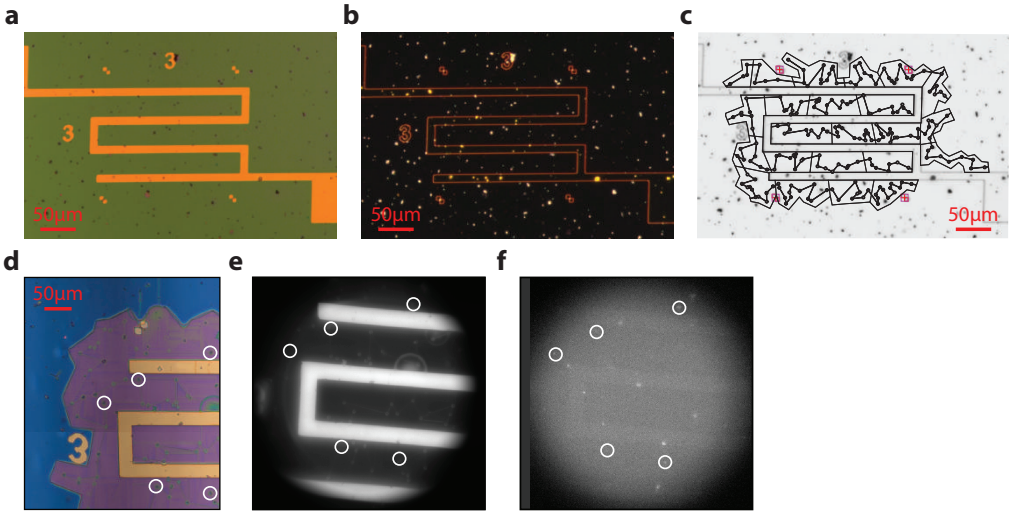

Figure 3.5: Design of electron-beam patterned structures. Bright field **(a)** and dark field **(b)** microscope image of a layer of doped-PVA spincoated on a silicon chip with gold markers and electrodes, previously deposited. **c:** Final .gds design aligned on the position of Ac nanocrystals extracted from the dark field image and from the fluorescence map at room temperature, measured with the setup in 3.4i. The lines are channels between the structures for gas evacuation. **d:** Optical microscope image of the lithographed structure after development for 30 seconds in DI water. Holes centered on the nanocrystals as well as gas evacuation channels can be clearly observed. White circles highlight nanocrystals which are visible as well in our room temperature fluorescence setup, both in reflection **(e)** and in fluorescence mode **(f)**.

3.2.2 Characterization of DBT emission properties at room temperature

To evaluate the fluorescence properties of the DBT molecules in the structure PVA we first characterize the emission properties at room temperature (RT). To this end, we use a custom microscope with wide field light-emitting diode (LED) illumination at 730 nm which off-resonantly excites DBT molecule ensembles, as reported previously [16, 102]. DBT emission is then imaged using a camera (Fig. 3.4i). Reflection and fluorescence images of an exposed square area after development at ambient conditions are shown in Fig. 3.4g,h. Due to the cross-linking process, exposed areas have a different contrast to non-exposed ones (Fig. 3.4g). The emission map (Fig. 3.4h) reveals bright spots randomly dispersed on

the sample in both exposed and non-exposed areas, which indicates that electron-beam irradiation does not inhibit the emission of DBT molecules.

3.2.3 Deterministic positioning of lithographed structures on nanocrystals' positions

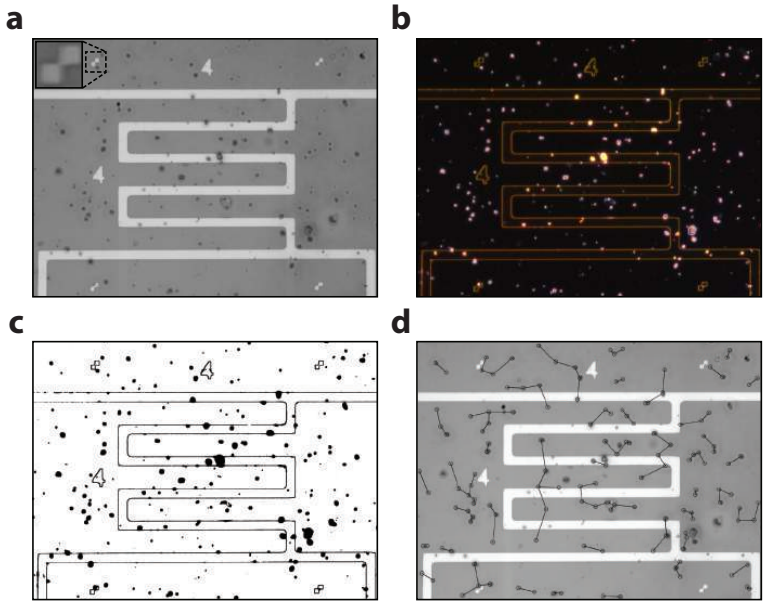

Figure 3.6: Automatic alignment of lithography mask. Bright field **(a)** and dark field **(b)** of a layer of doped-PVA spincoated on a silicon chip with gold markers and electrodes, previously deposited. Inset in **(a)** shows the marker used to align the optical image with the .gds design. **c:** Optical image treated in order to enhance the signal coming from the nanocrystals, which will be identified by the MATLAB code. **d:** The automatized mask overlapping circles on the nanocrystals' position. Using a different electron dose inside and outside the circles allows us to get 3D holes centered at the nanocrystals' position. Lines are guides for designing gas evacuation channels between the holes.

This setup enables the design of structures aligned with the nanocrystals' positions.
First, we compare the optical microscope image of the doped-PVA spincoated on the Si^{--}/SiO_2 chip to the fluorescence image taken with the room temperature setup illustrated in Figure 3.4i), to identify regular,

bright crystals of anthracene as shown in Figure 3.5a,b. Gold markers on chip facilitate the localization of such crystals. The optical image at RT of the anthracene nanocrystals on top of the gold markers is superimposed to the layout design containing the markers and electrodes to extract a precise location of the nanocrystals. The design is then modified such that at the position of each chosen crystal, extracted from the optical image, we overlap the design of the structures to be lithographed. Figure 3.5c shows an ensemble of more than 200 holes with DBT-doped Ac nanocrystals at the centre, connected by channels which will be useful for further fabrication steps for gas evacuation. The new design is used for electron beam lithography above the previously deposited doped-PVA, using the pre-existing markers for alignment. By choosing a different dose for the holes and the support area outside, after development for 30 seconds in DI water, a 3D lithographed structure in PVA aligned on the nanocrystals' position is obtained (see Fig. 3.5d), where the emission properties of the molecules are kept intact, as shown in Figure 3.5e,f.
This manual approach to making the design was later optimized and automatized using a MATLAB code, with the help of Dr. Kevin Schädler, as shown in 3.6. The resulting design, containing the markers and the relative position of the chosen structures, is used as a mask for the e-beam exposure and provides lithographed structured aligned on doped-PVA nanocrystals.

3.2.4 The effect of electron dose on single-photon emission

Next, we study the optical emission linewidth of DBT at low temperature with a custom cryogenic confocal scanning microscope (Fig. 3.7a) with single molecule fluorescence excitation spectroscopy [85]. Samples are cooled to 2.7 K in order to guarantee lifetime-limited linewidth of molecules and illuminated with a tuneable laser at 785 nm that excites the zero-phonon line (00ZPL) of DBT molecules. Before performing the measurement, we characterize the emission properties of DBT molecules such as linewidth and emission intensity as a function of the excitation power as discussed in Chapter 2. Working at low powers help to preserve the molecules' emission properties, hence laser intensity is kept below 1 W/cm^2 to avoid emission saturation.

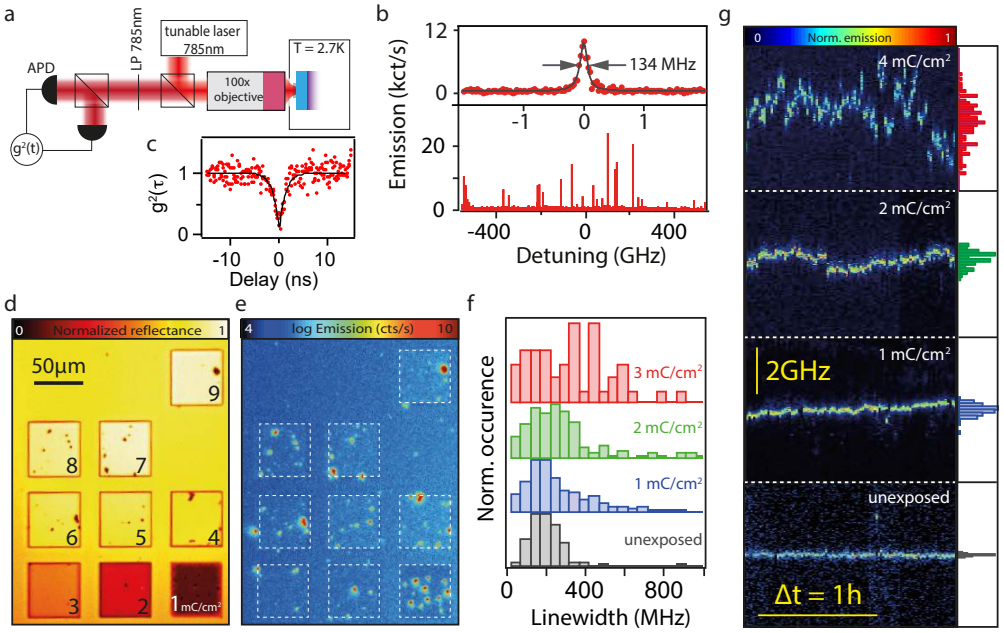

Figure 3.7: Narrow quantum emitters integrated in nanostructures. **a:** Sketch of the optical cryogenic setup to detect emission from single molecules. **b:** Fluorescence excitation spectrum of an ensemble (bottom) of single molecules (top: zoomed spectrum) in a nanocrystal at 2.7 K that have been exposed to e-beam (dose = 1 mC/cm^2). **c:** Anti-bunching measurement for resonant excitation of a single peak. The solid line is a fit to the data using a second-order correlation function. **d:** Optical micrograph of patterned squares of PVA containing nanocrystals exposed to different electron doses (from 1 to 9 mC/cm^2). **e:** DBT fluorescence map (integrated over all laser detuning) of the sample shown in **(d)**. **f:** Emission peak linewidth distribution for DBT subjected to various electron beam doses. **g:** Time traces of single DBT molecules emission for unexposed, 1, 2 and 4 mC/cm^2 e-beam doses (from bottom to top). Normalized histograms of central peak position are shown on the right to quantify the emitter's stability in time.

By sweeping the laser frequency and collecting red-shifted DBT fluorescence, the excitation spectrum of single molecules is detected. For instance, Fig. 3.7b (bottom) shows an excitation spectrum of an ensemble of DBT molecules in a single nanocrystal contained in nanopatterned PVA resist irradiated by an electron dose (1 mC/cm^2). A typical peak within the inhomogeneously broadened ensemble (top panel of Fig. 3.7b) displays a linewidth of $\Gamma/2\pi = 134 \pm 5$ MHz. The photon correlation

function measured in Hanbury-Brown and Twiss configuration under resonant fluorescence excitation of a single peak (Fig. 3.7c) shows strong antibunching with $g^2(0) = 0.08 \pm 0.02$, well below 0.5 which guarantees we're working with a single photon source, as discussed in Chapter 2. This observation confirms that the spectral peaks observed correspond to the emission from single molecules and that single photon emission is preserved upon electron irradiation.
Having observed single photon emission from electron-irradiated single DBT molecules, we now investigate the impact of electron dose on the emission linewidth and time stability of the molecules. We prepare an array of mesas irradiated with increasing electron dose ranging from 1 to 9 mC/cm^2 (Fig. 3.7d,e). In all exposed areas, we observe bright emission spots over the full laser detuning (Fig. 3.7e) corresponding to nanocrystal positions easily identified in the reflection image (Fig. 3.7d). DBT emission is only observed in the exposed areas as nanocrystals in non-exposed ones are washed away during the development process.
Then, we measure the spectra of a total of 808 single DBT emission peaks subjected to different e-beam doses, to obtain a linewidth histogram as a function of the e-beam dose (Fig. 3.7f). The emission linewidths are extracted from spectra measured via scanning laser spectroscopy [18] on anthracene nanocrystals within the mesa, with an averaging time of 0.01 s/point and a resolution of 0.02 GHz.
Our results show that low dose exposure (1 mC/cm^2) does not significantly broaden the DBT emission line in comparison to a control experiment (unexposed sample). With gradually increasing dose, larger emission linewidths are observed which broaden the distribution. We attribute this result to a modification of the molecule's environment due to detrimental effects of the electron radiation such as electrostatic charging, thermoplastic deformation, hydrocarbon contamination and knock-on mechanisms [103, 104] that affect the crystallinity of the host nanocrystal. Interestingly, a fraction of narrow linewidth ($< 2\pi \cdot$ 200 MHz) peaks remains for each e-beam dose studied. This is indicative of a dominant surface effect of the e-beam on the nanocrystal. This can be understood assuming a random distribution of molecules within the nanocrystal: molecules closer to the surface are strongly affected by any surface reconstruction [105], electrostatic puddles [106] or amorphous carbon contaminants [107] which can lead to a broadening of emission lines. Conversely, molecules closer to the centre of the nanocrystal are

less perturbed and exhibit narrow linewidth similar to non-exposed samples.
To determine the influence of electron beam irradiation on the spectral stability of the molecules, we monitor the behaviour of single molecule emission spectra in time for various doses (Fig. 3.7g). At lower dose, we observe stable lines over a time scale of hours, similar to the unexposed control sample. In contrast, measurements on emitters irradiated with higher doses reveal emission spectral jittering which can be due to the presence of fluctuating charge puddles created by e-beam exposure. Interestingly, it appears that even high electron irradiation doses do not induce significant emission blinking.

To highlight the versatility of our method and reduce even more the e-beam dose needed to create the nanostructures, we developed a similar protocol with another another water-based polymer, hydroxypropyl cellulose (HPC) [108]. Upon irradiation of an HPC film doped with DBT molecules with increasing dose ranging from 20 to 100 $\mu C/cm^2$, two orders of magnitude lower than for PVA, we pattern an array of mesas containing fluorescent nanocrystals (Fig. 3.8a,b). From this, we can control the height of the mesas of up to 80% of the initial film thickness, independent of the initial thickness t_i (Fig. 3.8c), similarly to the case of PVA. This result takes into account the natural shrinking of the polymer after it's cross-linked.
At such low doses, detrimental effects due to electron radiation are drastically reduced, as shown in Fig. 3.8d. At the maximum dose (100 $\mu C/cm^2$), we still observe that the most probable linewidths within the ensemble are similar to the unexposed case. Thus, EBL on HPC enables a more extensive height control of the doped polymer layer while exposing the molecules to a lower e-beam dose.

3.2.5 The effect of structure geometry on single-photon emission

Figure 3.9 shows an extensive study conducted to analyze the effect of holes size and exposure to electron beam in the immediate proximity of the nanocrystals to the organic molecules' emission properties. An ensemble of holes with diameter ranging from 3 to 10 μm is designed after alignment on DBT:Ac nanocrystals embedded in a PVA layer. The holes are surrounded by a support region with channels to evacuate gas

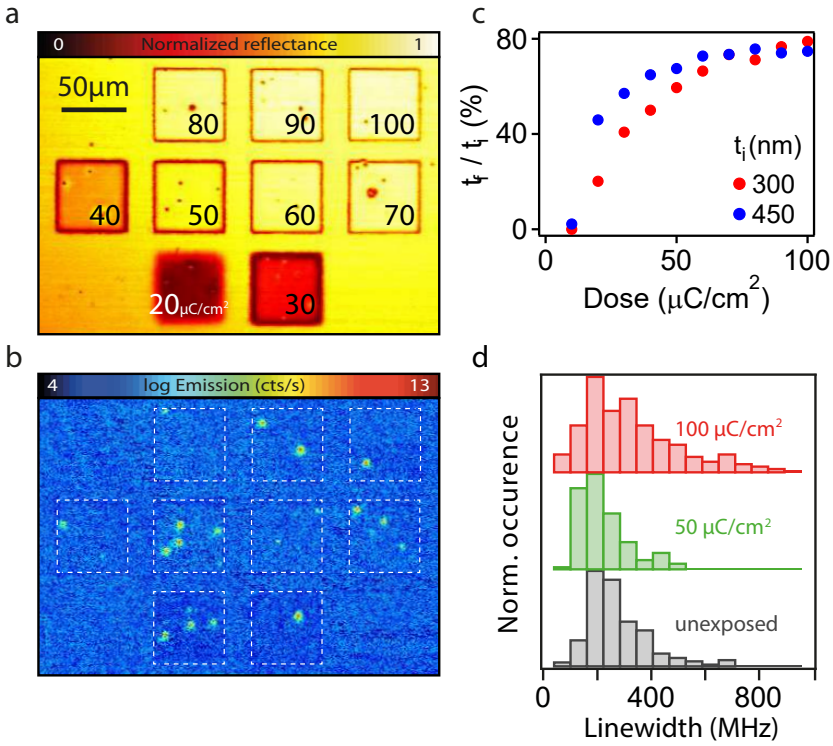

Figure 3.8: Low-dose nanolithography on HPC thin films doped with anthracene nanocrystals. **a:** Optical micrograph of patterned squares of HPC containing nanocrystals of DBT@Ant exposed to different electron doses (from 20 to 100 μC/cm^2). **b:** DBT fluorescence map (integrated over all laser detuning) of the sample shown in **(a)**. **c:** Ratio of remaining over initial HPC thickness as a function of EBL dose for two different initial film thicknesses. **d:** Emission peak linewidth distribution for DBT molecules subjected to various electron beam doses.

from in case of transfer of 2D materials. In this device, a layer of doped PVA is first spincoated and baked at 60 °C for 90 sec., then multiple layers of bare PVA are deposited on top reaching a total thickness of $\sim$ 400nm. Since the bare PVA hasn't been baked it will be sensitive to the electron-beam and will undergo cross-linking. Holes at the top of the dashed line in Fig. 3.9a have been exposed to low dose of 1 mC/cm^2, while at the bottom of the line only the support area has been exposed to a dose of 9 mC/cm^2. After development for 30 sec. in DI water we obtain holes with depth varying in the range $\sim$ 200 - 370 nm, depending on the diameter

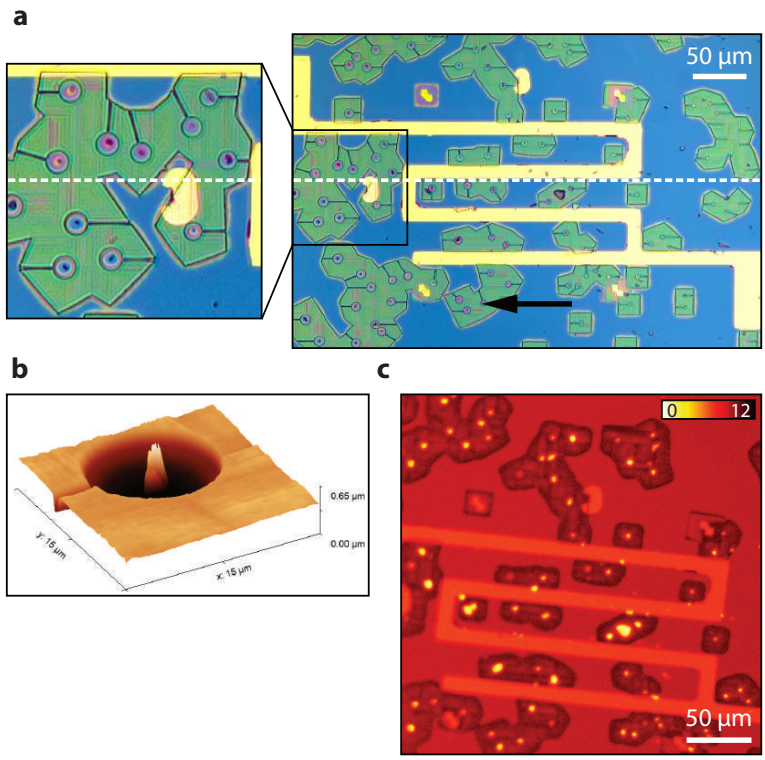

Figure 3.9: Electron-beam exposure of holes with different sizes aligned on DBT:Ac nanocrystals. **a:** Optical image of a series of holes of different diameter centered on nanocrystals, support area and gas evacuation channels. The dashed line separates holes that have been exposed with electron-beam at low dose (top) from the ones for which only the support region around has been exposed (bottom). In the inset, a visible change of colour between holes at the top and at the bottom indicates a difference in the depth of the hole. The black arrow represents the direction in which the diameter of the holes grows going from 3 to 10 μm. **b:** AFM image of a 10 μm diameter hole with a nanocrystal protruding at the centre. **c:** Emission map collected with out confocal microscope at 2.7 K, showing fluorescence from all of the nanocrystals in the holes. Scale bar shows the logarithmic scale of the emission.

of the hole as well as if the hole itself has been exposed to electron-beam. In case of exposure, the cross-linking induced by the lithography produces less shallow holes. In most cases though, despite embedding the nanocrystals in a layer of baked PVA, after the development we get nanocrystals protruding from the centre of the hole (see Fig. 3.9b), which

would jeopardize further fabrication steps.
To investigate the effects of such electron-beam exposure on the emission properties of the molecules, the sample is cooled down to 2.7 K and an emission map is collected (see Fig. 3.9c) using the technique presented in Chapter 2. We observe fluorescence from all the crystals inside the holes, hence we proceed analyzing single spectra from each of these crystals. Overall, we notice higher background compared to state-of-art molecules, and very few cases of narrow linewidth emission in case of holes with diameter below 5 μm. For nanocrystals in holes with diameter above 5 μm we still see bright and narrow peaks. The exposure of the centre of the hole to a dose of 1 mC/cm^2 also seems to slightly harm the emission properties of the molecules in the crystal. This effect might be attributed to the modification of the molecule's crystalline environment by the electron radiation through effects such as electrostatic charging, thermoplastic deformation, hydrocarbon contamination and knock-on mechanisms [103, 104], as mentioned before.

3.3 Integrating solid state single-photon sources into a nanophotonic device

3.3.1 Coupling narrow linewidth quantum emitters to waveguides

Impressive results have been achieved using capillarity to integrate doped crystals into waveguides [22, 23, 109], as well as using laser writing of the polymer hosting the crystal to create 3D waveguides [25].
We now present two applications of our method showing integration of narrow-linewidth emitters in nanophotonics devices: hybrid single organic molecules-waveguide structure and integration to a "bullseye" antenna. Fig. 3.10a shows a silicon nitride (SiN) crossed waveguide (WG) on a SiO_2 substrate fabricated in the group of Prof. Wolfram Pernice at the University of Münster. The WG has a 1 μm circular aperture at the intersection of the four branches. The group of Prof. Costanza Toninelli at LENS, European Laboratory for Non-Linear Spectroscopy, performed micro-infiltration of DBT@Ant nanocrystals into the aperture at the centre of the WG (Fig. 3.10b). The micro-infiltration set-up (Eppendorf Femtojet) consists of a micropipette (Eppendorf Femtotips) with external

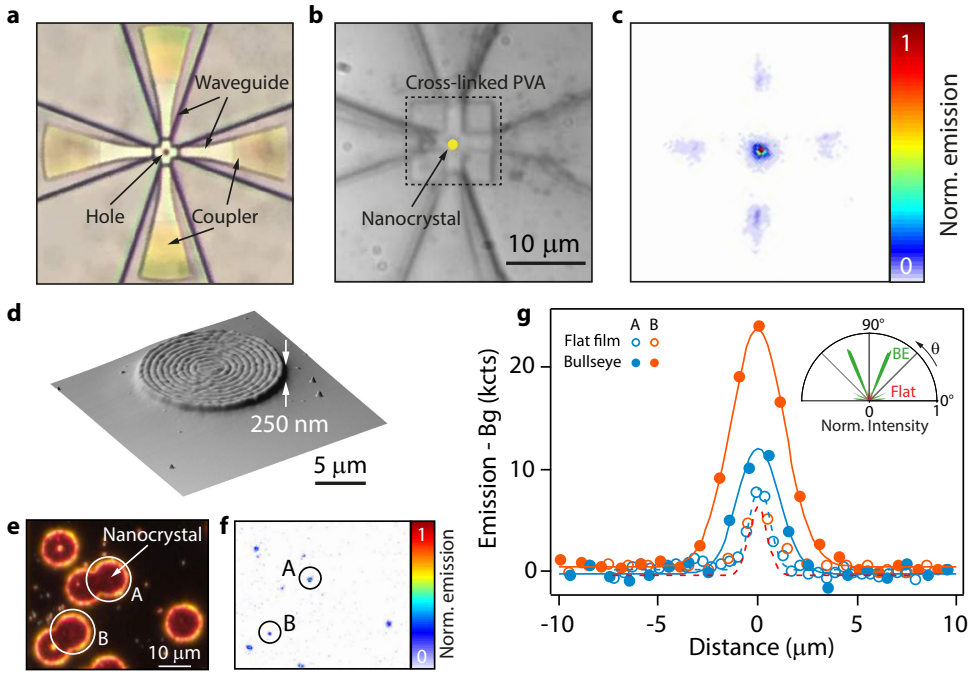

Figure 3.10: Hybrid nanophotonic devices with integrated DBT molecules. **a:** Crossed silicon nitride waveguide (WG) with a circular aperture of 1 μm at the intersection. **b:** Reflection image of a WG as illustrated in **(a)** after deposition of DBT@Ant nanocrystals and EBL patterning of a protective PVA layer. **c:** Fluorescence map collected with an EMCCD camera under off-resonant confocal excitation at the nanocrystal position for the WG shown in **(b)**. The out-coupled light at the four grating couplers is clearly visible. **d:** Atomic force microscopy (AFM) image of a "bullseye" structure exposed in HPC. The coupler is made of 10 rings and has a period of 550 nm and gap of 165 nm. **e:** Dark field reflection image of "bullseye" gratings aligned on the anthracene nanocrystal positions. **f:** Fluorescence image from the sample in **(e)**. **g:** Comparison of fluorescence at RT for two molecules in a cellulose flat film and after integration within the "bullseye" antennae shown in **(e)**. Enhancement of emission up to a factor 2 is observed, as confirmed by the simulation of the radiation pattern (inset).

diameter of about 2 μm and inner diameter of 0.5 μm, held on a 3D micrometric stage for fine movement. The aqueous nanocrystals suspension is injected into the micropipette, upon filtering with a 450 μm pore-size

filter (Sartorius Minisart) to get rid of eventual clusters and avoid obstruction. By monitoring the process with an optical microscope, the pipette tip is then approached to the region of interest until a micro-drop of suspension is deposited via surface adhesion. After water evaporation, nanocrystals are positioned with high precision and good success rate ($\sim 1/3$ of deposited NCs are at the centre of the crossed waveguide structure). Then, PVA squares are patterned by electron-beam lithography at the intersection of the crossed WG. As a result, EBL shaping allows to prevent crystal sublimation at ambient condition and provides a clean surface, which is crucial to achieve efficient light coupling into the waveguide. Off-resonant confocal excitation at 767 nm triggers emission from the molecules which partially couples into the waveguide and is guided throughout the four grating out-couplers (Fig. 3.10c). By evaluating the relative intensity of the guided emission, coupling of the molecule to the structure is estimated to be about 10%. This value is the result of the integration of the emission of many molecules in the nanocrystal, each with unequal coupling efficiency owing to the different position and orientation, and is therefore an underestimation. These results show the successful insertion of the nanocrystal at the centre of the WG and the potential of our technique to couple quantum emitters to standard photonics structures.

3.3.2 Enhancement of quantum emission by lithographed photonic structures

While for NVCs diamond has already proven to be an efficient platform for designing and controlling photonic structures such as "bullseye" antennae, integration of organic molecules has not yet found its preferred platform. We show here that water-based polymers as valuable candidates.

"Bullseye" antennae consist typically in circular concentric gratings etched in metals or other materials with a convenient refractive index. The periodicity, split width and separation are such that the light emitted from photon sources positioned at the antenna's center is scattered according to Bragg's law and results in a constructive interference in the vertical direction. The guided light can then be collected using a high numerical aperture with an efficiency of up to 90% [110].

A circular "bullseye" grating with a period of 550 nm and gap of 165 nm

is modelled and exposed on a layer of HPC on a gold substrate. This geometry serves to maximize the out-coupling of an optical excitation from the emitter into the far-field (Fig. 3.10d). The fabrication starts with the measurement of the fluorescence image of DBT molecules in the HPC layer, deposited on a substrate with pre-patterned alignment markers. The "bullseye" design is then aligned on the extracted positions with respect to the markers (Fig. 3.10e,f). By comparing the emission from nanocrystal positions A and B before and after integration into the "bullseye" antenna, we observe emission enhancement of up to a factor 2 (Fig. 3.10g). The increased signal in the presence of the "bullseye" structure can be interpreted as an increased collection efficiency, as confirmed by numerical simulations of the emission pattern of a structure with the same nominal parameters (see inset of Fig. 3.10g). It is worth noting that emission enhancement is mainly observed from nanocrystals that are not clearly visible in the dark field reflection image (Fig. 3.10e). This is due to the fact that nanocrystals more deeply embedded in the HPC layer couple more efficiently to the "bullseye" antenna.

3.4 Water-processed fabrication of polymeric photonic structures by nanoimprinting lithography

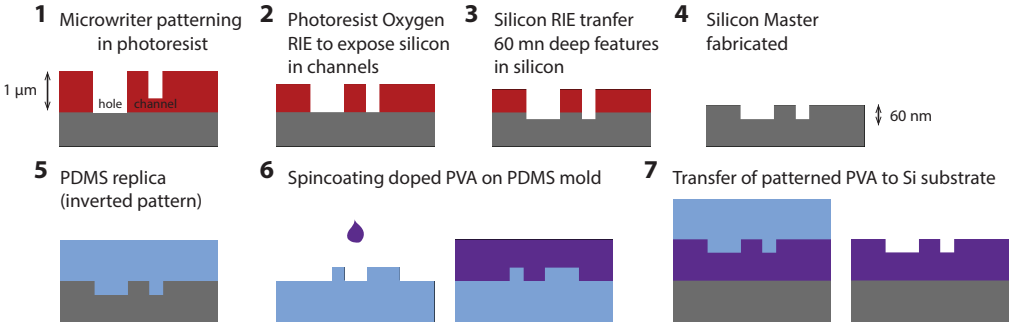

Figure 3.11: Process flow for the fabrication of array of holes with gas evacuation channels by replica molding.

In collaboration with Dr. Camilla Dore from the group of Prof. Augustín Mihi at ICMAB - UAB, Barcelona and Dr. Johann Osmond from

ICFO, we adopted the novel approach of using water-based polymers (PVA, HPC) as a platform for imprinting nanophotonics structures.
Water-based polymers are promising candidates for nanofabrication as they don't need any further solvents being purely water processable resists. The nanoimprinting technique has the advantage of allowing mass production fabrication with submicrometric resolution in a cost efficient and environmentally friendly fashion. It also needs little or no heating for the process, which could affect molecular emission properties in our case.
HPC molding for soft lithography has been used for the fabrication of photonic and plasmonic structures [111]. Large areas of submicrometric features and aspect ratios higher than 1 are fabricated in silicon, for replica molding procedure. It's also possible to combine them with metal deposition on the imprinted resist to obtain patterned metal structures [108]. HPC membranes are also used for their high-water solubility and excellent mechanical properties for transferring metal and carbon nanotubes inks [112].
Our approach is to use the same nanoimprinting technique by replica molding to fabricate hole structures with gas evacuation channels, similar to the ones presented in Section 3.2.5, in a much less invasive way as no solvents nor heating are needed for the nanoimprinting. The fabrication steps are illustrated in Figure 3.11.

Dr. Dore first fabricated a silicon mold with holes of diameters of 10 μm and 5 μm connected by gas evacuation channels of 2 μm. Then a PDMS replica is fabricated based on the silicon mold. By spincoating on the PDMS mold a layer of PVA at 1800rpm, acceleration 1000rpm, for 60 sec., we obtain an array of holes connected by gas evacuation channels of ~ 1.2 μm which is then aligned and transferred onto the silicon chip and this process is repeated until covering the whole area of the silicon chip, as shown in Figure 3.12a-c. We then try to repeat this procedure using PVA doped with nanocrystals prepared as in Section 3.1. While the fabrication is pretty straightforward and easy to reproduce in an extensive way, two main issues appear that really compromise the process. On one hand, the spatial distribution of NCs in spincoated PVA is such that getting one NC in a hole has an extremely low probability (below 5%) (Fig. 3.12d. On the other, the NCs are too high to fit into the mold and end up poking outside the holes in the final PVA layer compromising further transfer of a 2D material on top (see Fig. 3.12e). We tried to optimize this process by depositing multiple layers of polymer in order

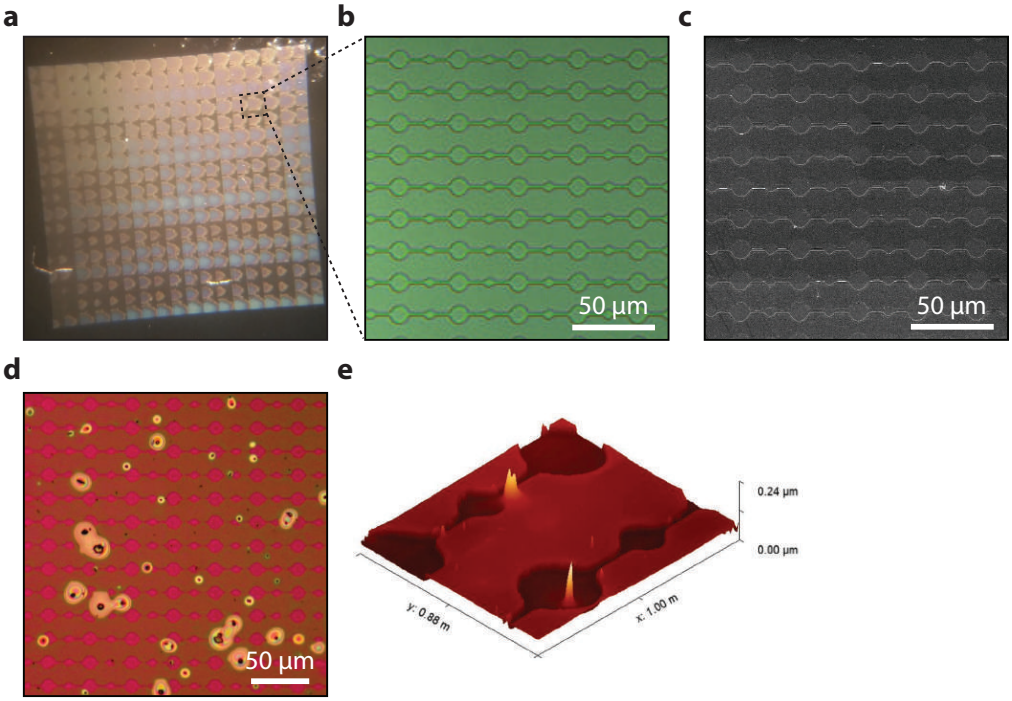

Figure 3.12: Fabrication of hole structures by nanoimprinting of doped PVA. **a:** Silicon chip covered by PVA membranes patterned by replica molding. Optical image **(b)** and SEM micrograph **(b)** of the patterned structures. Scale bar is 50 μm. **d:** Replica molding with doped PVA. **e:** AFM tomograph of holes with NCs poking out.

to create a thicker coating above the nanocrystals but observed that the deposition of each layer of water-based polymer ended up dissolving in the previous one, hampering the chance of getting a thick polymeric layer. One possible approach to improve the results of this technique could be to prepare a polymeric suspension with filtered nanocrystals to control their dimension even though their density would also naturally drop. Another direction to explore could be the one of first depositing the doped-polymer onto the silicon chip and later transferring the nanoimprinted structures, even though in this way it would not be possible to control the alignment between the holes and the nanocrystals.

3.5 Exfoliation of 2D materials for integration into hybrid devices

We target the fabrication of hybrid devices integrating quantum emitters in the form of single organic molecules (see Section 3.1) and 2D materials. Graphene [28] and transition metal dichalcogenides (TMDs) are well known atomic-thin materials. The exfoliation technique of these materials has been perfected over the last years allowing us to obtain big, single-layer flakes. With relatively small absorption in the visible range of light (2.3% for graphene) and being electrically tunable by modifying their Fermi energy, these materials can be used as semi-transparent electrodes and easily integrate in our devices. While being extremely interesting on their own for their semimetallic (graphene) and semiconducting properties (TMDs) [113], they can also be stacked to form complex Van der Waals heterostructures [114, 115].

3.5.1 Stamp transfer technique of 2D materials on hybrid devices

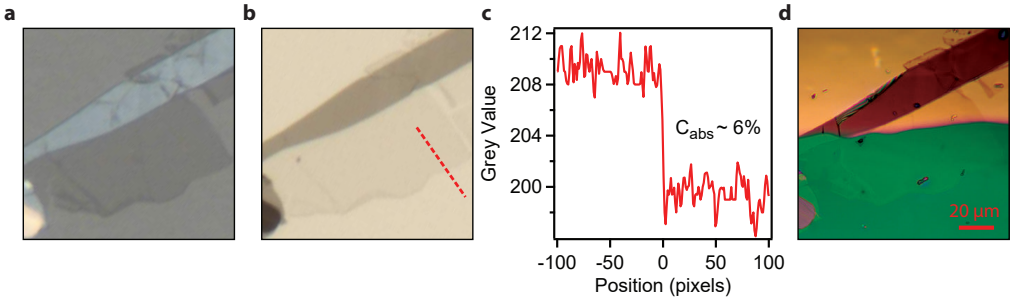

Figure 3.13: Optical bright field image **(a)** and transmission image **(b)** of a graphene flake exfoliated with the technique present in the text. **c:** Line cut of the transmission signal along the red dashed line in **(b)** showing absorption contrast of ~ 6 % and suggesting we're dealing with a bilayer flake. **d:** Optical image of the final device with the bilayer graphene transferred on top.

To obtain and transfer 2D materials on our devices we use a dry transfer technique [116]. First, bulk TMDs or graphite are exfoliated mechanically using commercial polydimethylsiloxane (PDMS) sheets.

Starting from a bulk mesa of the material on the PDMS sheet we repeatedly peel flakes of graphite off the mesa with a fresh PDMS surface until the area of the PDMS is covered with flat, light grey areas, then we inspect the final PDMS stamp under the microscope. Exfoliated flakes of both materials are identified optically by their optical absorption contrast under white-light illumination on a transparent polymer stamp used for transfer onto the devices (see Figure 3.13a,b). We perform line cuts through micrographs of the graphene or TMD flake to calibrate the number of flakes from the absorption contrast modeled as $C_{abs} = \frac{I_{PDMS} - I_{flake}}{I_{PDMS}}$, where I_{PDMS} and I_{flake} are the greyscale values on bare PDMS and on the flake, respectively. As a reference, we assume that for thin flakes up to 4-5 layers, the step-like reduction of contrast is $\sim -3\%$ for graphene and -4% for TMDs (Figure 3.13c).
The transfer process is performed at room temperature and without other nanofabrication steps or need of solvents. We place the PDMS stamp with the flake we want to transfer upside down on a manual micromanipulator which allows us to control the x-y-z positions of the stamp with a positioning accuracy of typically 2-3 μm. Under the microscope, we approach the stamp onto the chosen position of the sample. Once in contact, we heat the substrate with an electric heating stage up to 80 °C. We then slowly lift off the stamp from the surface of the sample, always controlling at the microscope that the flake is well stuck on the sample and doesn't detach or wrinkle. With no need of further processing, the flake is then transferred with good adhesion and flatness onto our device (Fig. 3.13d).

3.5.2 Fabrication of stacks of encapsulated 2D materials

When encapsulation in hexagonal boron nitride (hBN) is needed for further protection of the 2D material [117] a different technique is used to exfoliate the 2D material,make the stack of bottom hBN/2D material/top hBN and transfer it, as illustrated in Figure 3.14a. First, our chosen 2D material (graphene or TMD) is exfoliated using a strip of high quality ultra-clean blue tape, where a mesa of the 2D material is deposited and repeatedly peeled until covering the whole surface of the tape. Then Si^{--}/SiO_2 clean chips of around 1×1 cm^2 are stuck with the clean surface on the tape, peeled and later inspected under the microscope to search for monolayer flakes.

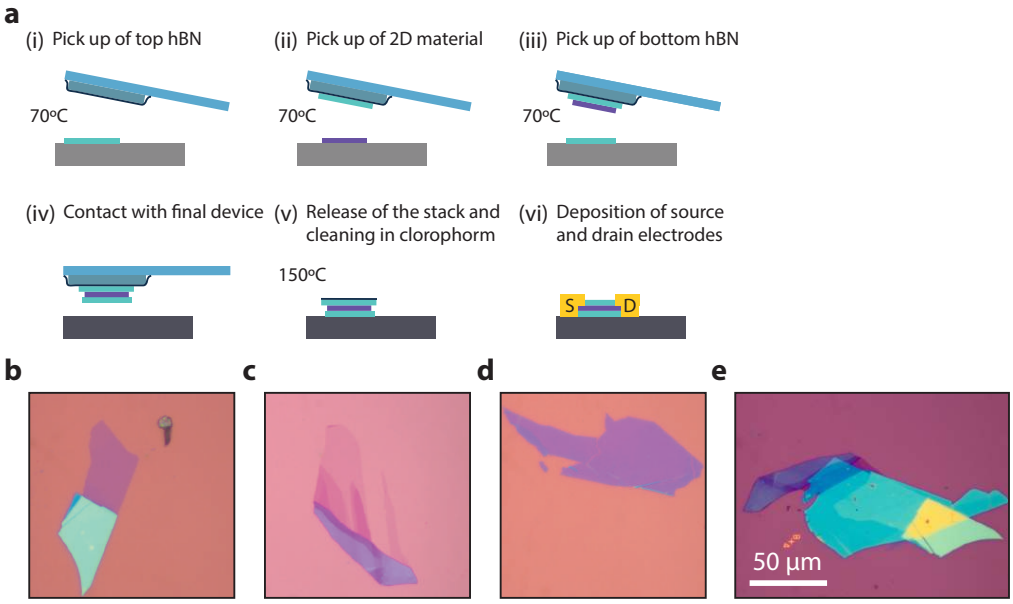

Figure 3.14: a: Fabrication steps of a stack of encapsulated 2D material. **b:** Top hBN flake with thickness $\sim$ 10 nm. **c:** Monolayer graphene flake. **d:** Bottom hBN flake with thickness $\sim$ 50 nm. **e:** Final stack of bottom hBN/Graphene/top hBN.

Flakes of hBN are exfoliated using a thin PDMS layer and then transferred onto a Si^{--}/SiO_2 chip.
Flakes of top hBN, 2D material and bottom hBN (Fig. 3.14b,c,d respectively) are picked up in this order using a stamp of PDMS coated with a thin layer of propylene carbonate (PC). The pick up is performed under a microscope, controlling the temperature by an electrically heated platform and the speed at which we get in contact with the silicon chip. The stack is then dropped at 100 °C onto our final device under the microscope using a micro-manipulator and temperature is increased up to 180°C until the PC layer starts to melt and the stack is detached from the stamp. The PC layer left on the device is then dissolved in chloroform for 30 mins, leaving a clean bottom hBN/2D material/top hBN stack on our final sample (see Fig. 3.14e).

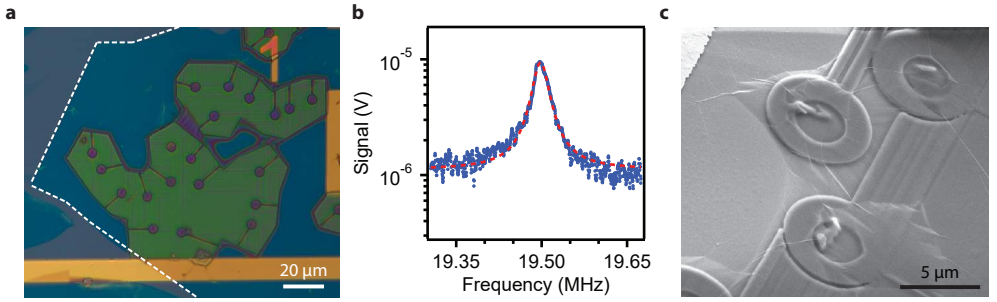

Figure 3.15: Building a hybrid optomechanical device. **a:** Final hybrid device with a big monolayer graphene flake onto an electron-beam shaped doped PVA structure, covering more than 20 holes. **b:** Mechanical response of a suspended graphene drum. **c:** SEM image of some nanocrystals poking out of the holes therefore affecting the mechanics of the 2D drum.

3.5.3 Preliminary results on nano-optomechanics

Following previous work in the team about near-field optomechanics [45], we focused on a novel type of coupling between single photons and 2D materials, purely dispersive, based on vacuum quantum fluctuations [50].

The main challenge we faced in this direction was the fabrication of such devices. We used the technique presented in Section 3.2.5 to design hole structures deterministically positioned at the DBT-doped Ac nanocrystals' location. The laser spectroscopy technique presented in Chapter 2 allowed us to address single molecules in each NC. The final device (see Fig. 3.15a) has been reproduced with success various times using the dry transfer technique for depositing suspended graphene flakes on top of the 3D structure. Even though we have been able to measure few suspended membranes with good mechanical properties (see Fig. 3.15b, showing a resonator with quality factor $Q \sim 600$), in many cases the NCs didn't fit inside the holes but poke out, affecting the mechanics of the 2D drums (see Fig. 3.15c). Another issue which appeared very often with this fabrication was that we couldn't observe any emission from the nanocrystals in the holes, supposedly because of contamination effects due to electron irradiation. Only once we succeeded in having a complete device with narrow-linewidth DBT molecules below a good quality resonator.

To increase the success rate of this process a polymeric suspension of filtered NCs could be used, in order to control the dimension of the

nanocrystals. Also, designing larger hole structures might reduce the contamination effects affecting the molecular emission but it might also make the transfer of suspended membranes more difficult.

3.6 Conclusions

Our fabrication technique of doped nanocrystals in water-based polymers provides a platform for easy on-chip integration of single photon sources protected in a nanoscale environment. We observe narrow linewidth single photon emission from electron-irradiated DBT molecules in such polymeric medium. The technique presented highlights the potential of electron beam patterning for single-molecule-based quantum photonic devices. We envision different geometries such as waveguides [22], ring resonators or "bullseye" antennae [110] and pillar structures for efficient out-of-plane light extraction and emission control. Combining PVA with additives [118] for increasing its nominally low refractive index ($n_{PVA} \sim 1.5$) would enhance light confinement on substrates of similar refractive index. Further, solid-state quantum emitters properties are strongly affected by their near-field environment (plasmon-molecule coupling [119, 120], Casimir [50], energy transfer [36, 102]. Our patterning technique opens new possibilities exploring such near-field effects by shaping the emitter's environment with high precision, as well as combining it with other materials (conductive films, 2D materials). Such hybrid systems enable manipulation of the emitter properties at the scale of a single molecule, which would have a strong impact for quantum nanophotonic [58] and optomechanics [50, 121].

Fabrication of devices integrating ultra-narrow linewidth quantum emitters with 2D materials

- We synthesized DBT molecules in anthracene nanocrystals in a polymeric medium with state-of-the art emission properties
- We developed a technique for electron beam shaping of doped polymers not affecting the emission of the narrow linewidth quantum sources
- We designed 3D lithographed structures aligned on nanocrystals' position
- We explored different directions for the integration of solid state single-photon sources with nanophotonic devices such as waveguides, "bullseye" antennae and NEMS
- We realized hybrid devices combining quantum emitters and exfoliated 2D materials

Chapter 4

Electrical control of lifetime-limited quantum emitters using 2D materials

Hybrid nanophotonic systems blend the strengths of distinct photonic elements to strongly enhance light-matter interactions [122] in integrated photonic circuits. In these systems, narrow-linewidth quantum light emitters play a key role as single-photon sources (SPSs) which interact with their nanoscale environment. Controlling these interactions provides versatile SPS tuning required for coupling quantum resources. [58] Integrating nanoscale light emitters with two dimensional (2D) materials is motivated by the rich physics of near-field interactions and new hybrid light-matter states [123, 124]. This approach unites integrated solid-state SPSs such as nitrogen vacancy centers, quantum dots and single molecules with the diverse optoelectronic properties of 2D materials that facilitate emitting, controlling [38] and detecting light at the nanoscale. In such hybrid devices, quantum emitters can be integrated at subwavelength separation to the 2D interface to achieve efficient near-field coupling, which modifies the emitter's radiative decay rate [36, 125] or transition energy [50]. Recent experimental studies integrated 2D materials with ensembles of broadband emitters to demonstrate electrical [37, 44] and electromechanical [45] tuning of the decay rate by controlling nonradiative energy transfer (nRET) or the energy flow to confined electromagnetic modes such as 2D polaritons [44]. Therefore, hybrids of

2D materials and SPSs have the potential for *in situ* control of the conversion and channelling of single photons at the nanoscale. So far, these studies have been limited to ensembles and broad linewidth emitters. Integrating bright and narrow quantum emitters in such systems paves the way toward a tunable quantum light-matter interface, which is an essential ingredient for integrated quantum networks.
In this chapter, we present hybrid integration of 2D materials (semimetallic graphene or semiconducting MoS_2) with single, lifetime-limited quantum emitters in nanocrystals to provide active emission control. Using the 2D materials as transparent electrodes, we show broadband Stark tuning of the emission energy over 40000 times the emitter's linewidth and fast modulation of the emitter's optical resonance on the time scale of its radiative lifetime [126]. Such tuning can mitigate inhomogeneous broadening in solid-state environments to enable resonant and synchronized interaction between distinct quantum systems and allows for controlled coupling of narrowband quantum emitters to broadband nanophotonic circuitry.

4.1 Building a hybrid capacitive device integrating single molecules with 2D materials

Our hybrid devices are made of two main building blocks: quantum emitters and 2D materials. Our approach is particularly suited for making integrated devices: although the 2D material is just tens of nanometers from the quantum emitter, we observe only weak emission linewidth broadening and spectral diffusion. In contrast, emitters close to bulk transparent electrodes [127] such as ultrathin metal films suffer strong emission quenching, which hampers nanoscale integration. Furthermore, we find that the deposition process required to integrate a transparent conducting oxide inhibits molecular fluorescence, which highlights the potential of 2D materials for integration with ultrasensitive quantum emitters. At the same time, we show that a single quantum emitter can be used as a transducer of the 2D materials' electronic properties.

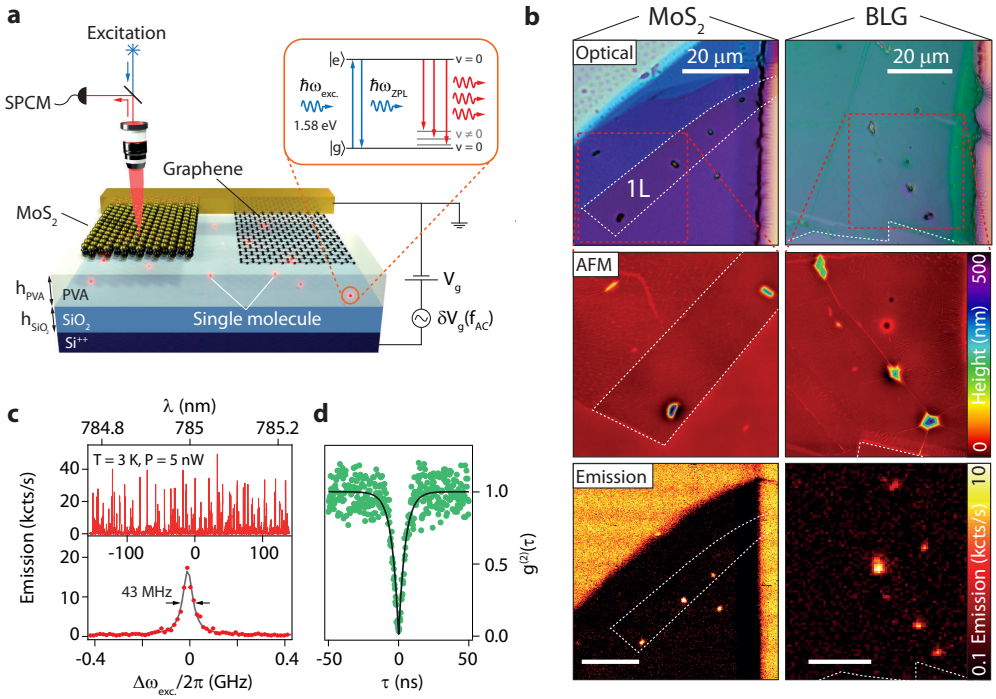

Figure 4.1: Single molecules integrated with 2D materials. **a:** Hybrid device schematic. Atomically thin layers of graphene and MoS_2 cover fluorescent molecules embedded in a PVA film (h_{PVA} = 300 nm) on SiO_2 (h_{SiO_2} = 285 nm). Single molecules are resonantly excited (inset) and their red-shifted fluorescence detected with a single-photon counting module (SPCM). Electric fields are controlled by applying DC (V_g) and AC (δV_g) potentials to the Si^{++} backgate. **b:** Top to bottom: optical micrograph, AFM topography, and DBT emission map for MoS_2 (left column) and bilayer graphene (right column) devices. White dashed lines outline the flakes. Scale bars are 20 μm. **c:** Top panel: fluorescence excitation spectrum of an ensemble of single molecules in an uncovered nanocrystal at 3 K. Bottom panel: detail of one emission peak with Lorentzian line shape (solid line), showing a full width at half-maximum of 43 $\pm$ 7 MHz. **d:** Antibunching measurement for resonant excitation of a single peak as shown in **(c)**. The solid line is a fit to the data using a second-order correlation function.

4.1.1 Integration of solid state quantum emitters with 2D materials for electronic control

As quantum emitters we choose single dibenzoterrylene (DBT) molecules: bright, photostable single-photon sources [63, 68] emitting at 785 nm (1.58 eV) with lifetime-limited linewidth ($\sim$ 40 MHz) [18] at 3 K even when hosted in a submicron environment [16]. Experimentally, we perform scanning laser spectroscopy to address individual DBT molecules at subwavelength separation to a 2D metallic or semiconducting interface.

In our device, the suspension of DBT-doped anthracene nanocrystals in PVA (prepared as in Section 3.1) is spin-cast onto a p-doped Si wafer coated with 285 nm thermally grown SiO_2 (see Fig. 4.1a). MoS_2 or graphene flakes are placed on top of the polymer film by a dry transfer technique and electrically contacted by gold electrodes. Electrodes are deposited onto the coated chip by thermal evaporation of 100 nm Au through a shadow mask. Nanocrystals close to the electrode displaying DBT fluorescence are localized at room temperature using off-resonant wide-field illumination.

Bulk MoS_2 and graphite are exfoliated mechanically using commercial polydimethylsiloxane (PDMS) sheets. Mono and bilayer flakes of both materials are identified optically by their optical absorption contrast under white-light illumination on a transparent polymer stamp used for transfer onto the devices. Line cuts through micrographs of a large bilayer graphene flake (BLG) and a multilayer MoS_2 used to make the devices are shown in Fig. 4.2a) and Fig. 4.2b) respectively. For thin flakes up to 4-5 layers, the step-like reduction of contrast -3% for graphene and -4% for MoS_2 reveals the flake thickness. We independently confirmed this calibration with Raman spectroscopy of graphene flakes in a previous publication [45]. A confocal reflection map of the transferred MoS_2 multilayer flake on PVA at 3 K is shown in Fig. 4.2c, using 30 nW laser power at 532 nm. Under an identical excitation configuration, a photoluminescence (PL) map of the same area shown in Fig. 4.2d reveals strong emission from the area with the 4% contrast reduction (as shown in Fig. 4.2a), which confirms that this area is a monolayer of the material [113]. The transfer process onto anthracene nanocrystals in PVA is performed at room temperature and without other nanofabrication steps (dry stamp transfer), which could potentially degrade emission.

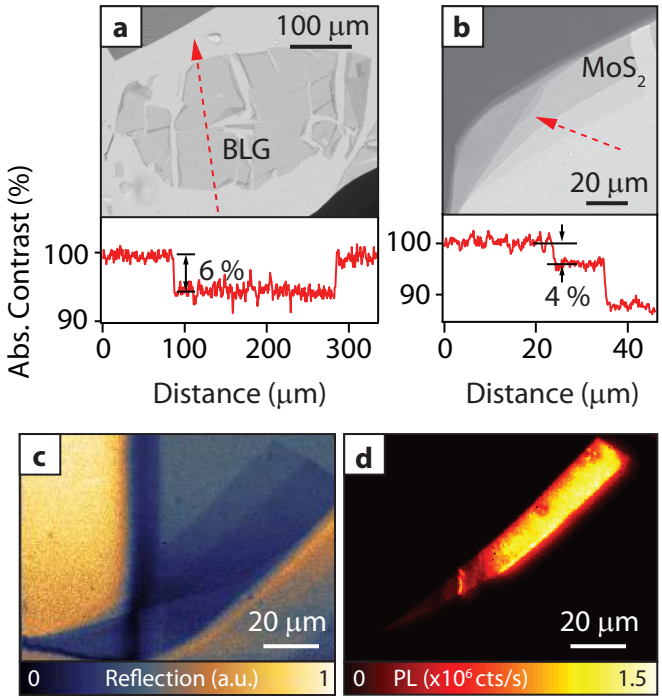

Figure 4.2: Optical identification of 2D flakes. Greyscale micrographs of BLG **(a)** and multilayer MoS_2 **(b)** flakes on a PDMS stamp under white light illumination show absorption by the atomically thin layers. Line cuts (red dashes) show step-like absorption contrast reduction with increasing number of layers (panels below micrograph). **c:** Scanning confocal reflection map of the transferred MoS_2 flake under 30 nW of 532 nm Illumination at 3 K. **d:** A scanning confocal photoluminescence (PL) map of the same area as in **(c)** shows strong emission from the monolayer area of the flake.

4.1.2 Characterization of single-photon sources

Measurements are performed under vacuum in a cryostat at 3 K. Using a custom-built confocal microscope to locally illuminate the device, we excite single molecules with a tunable 785 nm laser with circular polarization at 5 nW, below the saturation power of $\sim$ 20 nW.

To verify that we do not induce spectral broadening by saturating the molecules with excessive resonant excitation powers, we perform excitation power-dependent measurements of emission strength and

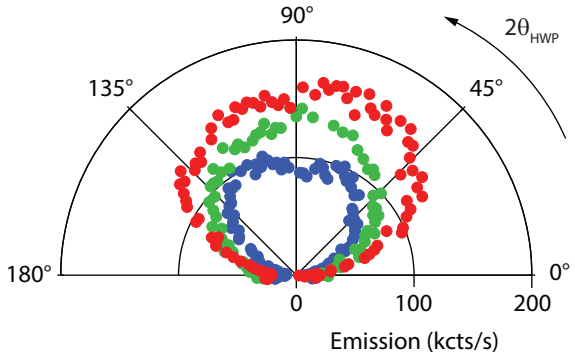

Figure 4.3: Projection of the linear dipole moment with respect to the excitation polarization for three different molecules (red, green and blue) in the same nanocrystal.

linewidth as explained in Chapter 2. For this particular emitter,we extract an emission saturation intensity of 67 kcts/s and a homogeneous linewidth of 145 MHz. Using a half-wave plate on a rotation mount, the excitation polarization is rotated by $2\theta_{HWP}$, where θ_{HWP} is the rotation angle of the half-wave plate. We excite three different molecules in the same nanocrystal at different linear polarization angles and record their angle-dependent emission intensity as shown in Fig. 4.3. This measurement confirms the dipolar nature of the emission and shows that dipoles of different molecules within a single nanocrystal are co-aligned [18].
After exciting with a 785 nm laser red-shifted single photon emission is detected with a single-photon counting module (SPCM) combined with spectral ZPL filtering by a long-pass filter. Emission maps are made using pseudobroadband excitation of DBT ensemble fluorescence by fast modulation (200 Hz) of the laser detuning compared to the SPCM integration time ($\sim$10 ms). MoS_2 photoluminescence is excited using a 532 nm laser and detected with a spectrometer (10 s integration time). Spatial maps of DBT ensemble fluorescence at 3 K show bright, localized emission beneath both 2D materials (4.1b). A simplified DBT energy level scheme is shown in the inset of Figure 4.1a. The transition of interest is the zero-phonon line (ZPL) between the ground vibrational levels (ν = 0) of the electronic ground and excited states. Upon resonant excitation of this transition, the molecule relaxes either to the electronic ground state (30-40% of emission [62]) or to a higher vibrational state ($\nu \neq 0$), thereby

emitting a red-shifted photon. Scanning laser spectroscopy on a pristine nanocrystal (4.1c) at 3 K reveals a series of sharp peaks from a DBT ensemble. This peak dispersion arises from local variations of strain and charge and enables spectrally addressing a single molecule [74]. The narrowest peaks in such ensembles display a typical linewidth of $\Gamma/2\pi = 43 \pm 7$ MHz. To confirm that we can address single molecules in a nanocrystal, we measure statistics of photon emission in Hanbury-Brown and Twiss (HBT) configuration (Figure 4.1d) and fit the normalized data with the second-order intensity autocorrelation, as discussed in Section 2.1.4. At zero delay time, we find $g^{(2)}(0) = 0.04 \pm 0.02 < 0.5$, which is signature of a single-photon source. We extract an excited state lifetime of $\tau_{DBT} = 4.7 \pm 0.5$ ns, implying a lifetime-limited linewidth $\Gamma_0/2\pi = 1/2\pi\,\tau_{DBT} = 34 \pm 5$ MHz, comparable to values observed in bulk anthracene crystals [62].
Therefore, single molecules in our device can exhibit lifetime limited linewidth within the measurement error. In a solid state environment, this linewidth can be broadened by dephasing and near-field interactions, which can hamper the performance of emitters in nanostructured devices [4].

4.2 Near-field effect of a quantum emitter in proximity of a 2D material

In our device, a 2D material is placed in the near-field of a single emitter (separation $d \ll \lambda$). In this regime, near-field interactions such as nonradiative energy transfer (nRET) from the molecule to the 2D material and Casimir-Polder (CP) energy level shifts are expected to occur. Both interactions scale divergently with separation as d^{-4}, in contrast to d^{-3} for bulk interfaces [50]. The nRET process leads to a linewidth broadening, while the CP energy level shift is a quantum effect related to the modification of vacuum fluctuations by the 2D interface. At fixed emitter-2D material separations, we can quantify the nRET contribution due to the presence of the 2D material by its impact on the emission linewidth. The CP contributions are difficult to quantify because for one specific emitter, the emission energy with and without the 2D material cannot be measured independently.

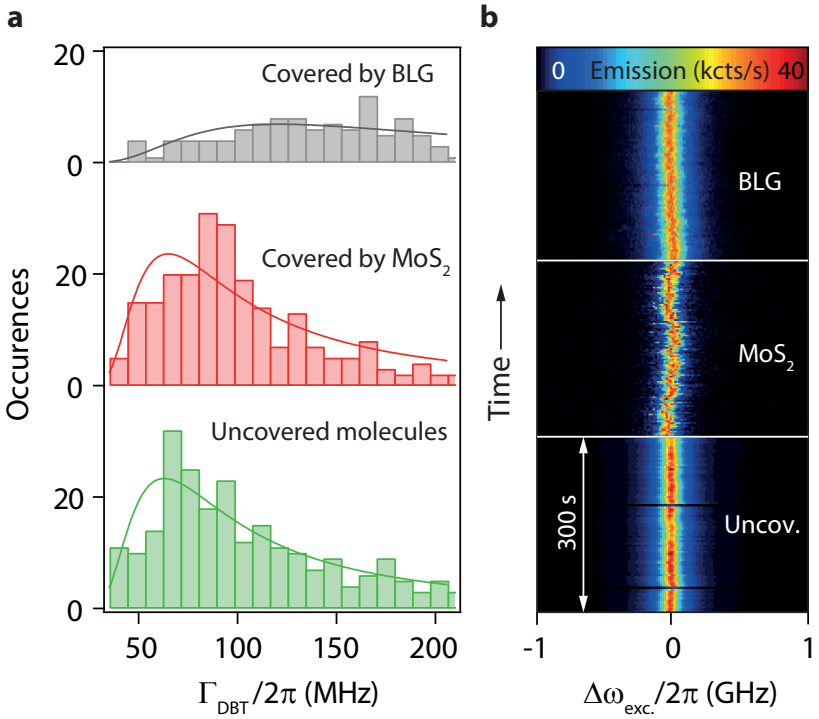

Figure 4.4: Emission broadening and time stability in the presence of 2D materials. **a:** Linewidth distribution for uncovered DBT (green), DBT covered by monolayer MoS_2 (red) and bilayer graphene (gray). Solid lines are fits to the data as described in the main text. **b:** Time trace of single DBT molecule emission (3 s/line) for uncovered DBT (bottom) and DBT covered by monolayer MoS_2 (middle) and bilayer graphene (top).

4.2.1 2D electrode deposited on DBT-doped nanocrystals in PVA

By measuring the emission linewidths of over 500 molecules (Figure 4.4) in three different configurations (uncovered, covered by bilayer graphene (BLG)/MoS_2) in different samples, we quantify the effect of proximity to 2D materials on the emission linewidth. We quantify the most probable linewidth $\tilde{\Gamma}/2\pi$ in each case by fitting the linewidth histogram with a Smirnov distribution [128], which describes single molecule linewidth distributions perturbed by long-range coupling to two-level fluctuators, e.g. in polymers. For uncovered nanocrystals, we obtain $\tilde{\Gamma}_{uncov.}/2\pi = 62$

MHz, which is comparable to $\Gamma_0/2\pi$, the lifetime-limited linewidth extracted from the second order autocorrelation function. This implies that the anthracene nanocrystal is a highly stable and crystalline environment [16] and most molecules within it do not experience significant spectral diffusion due to defects or proximity to the surface [16]. While emitters covered by MoS_2 experience extremely weak spectral broadening ($\tilde{\Gamma}_{MoS_2}/2\pi$ = 65 MHz), they are significantly broadened when covered by BLG ($\tilde{\Gamma}_{BLG}/2\pi$ = 108 MHz) and their linewidth distributed over a larger range. We attribute this broadening to higher nRET efficiency to gapless graphene as electronic transitions can be optically excited over a large range of energies and in particular at $\hbar\omega_{ZPL}$. In contrast, MoS_2 has bandgap and excitonic resonances at energies $> \hbar\omega_{ZPL}$, resulting in weak nRET, which preserves the narrow linewidth. These results show that neither the presence nor the integration process of 2D materials have a strong detrimental impact on the emission properties.

4.2.2 Performance of an ITO electrode

To compare the performance of 2D electrodes to commonly used transparent electrodes, we deposit indium tin oxide (ITO) onto a PVA film doped with anthracene nanocrystals hosting DBT molecules (Fig. 4.5a). We first confirm that nanocrystals in this sample contain emitting DBT molecules by illuminating the device with a 730 nm LED at room temperature to excite DBT emission off-resonantly. Using a long-pass filter at 785 nm and a sensitive camera, we make emission images as shown in the inset of Fig. 4.5a. Next, 100 nm of ITO is deposited onto this sample by sputtering at room temperature and subsequent annealing at 230 °C for 1h in ambient atmosphere,resulting in the appearance of ridges over the entire device surface (Fig. 4.5b). Although the nanocrystals are still visible in the PVA film after ITO deposition and annealing, we no longer observe DBT emission (inset Fig. 4.5b). As anthracene's bulk melting point is 200 °C and we have experimentally observed melting of isolated anthracene nanocrystals at 150 °C, we believe that the high temperature of the ITO annealing process causes structural damage to the nanocrystals and possibly oxidation of DBT molecules. For instance, higher molecule mobility can result in impurities - including our DBT molecules - being pushed towards the crystal edges. In this way the host-guest configuration is modified causing bleaching of the molecules.

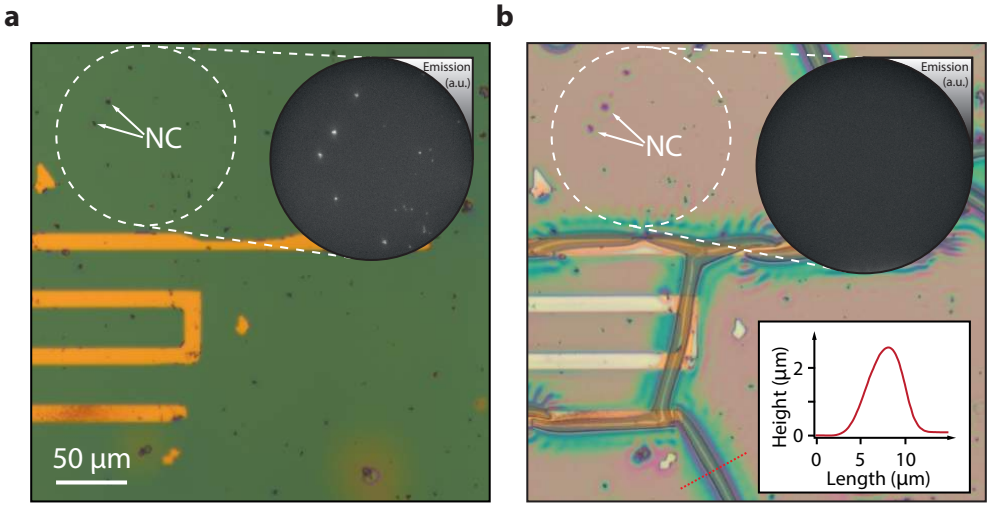

Figure 4.5: ITO deposition on a PVA thin film doped with anthracene nanocrystals (NC) hosting DBT molecules. **a:** Doped PVA film on a chip with gold electrodes. Inset: Emission map of area outlined as a dashed circle, taken at 300 K using 730 nm widefield illumination. **b:** The same sample as in **(a)** after sputtering 100 nm ITO and annealing. Top inset: widefield emission image of the same area as indicated in **(a)**. Bottom inset: AFM line section shown in dashed red.

In contrast, as ITO has a large bandgap of 3.6 eV compared to DBT's transition energy (1.58 eV), we do not expect non-radiative energy transfer to cause emission quenching. This result highlights the weakly invasive nature of 2D material integration, which makes it particularly suitable for fragile quantum emitters.

4.2.3 Statistics of single molecule emission fluctuation

To confirm that emission stability in time is preserved after 2D material integration, we measure DBT spectra over time for the three configurations (uncovered, covered by graphene/MoS_2) as shown in Figure 4.5b. To quantify emission stability in time, we extract histograms of fluctuations of ZPL frequency $\omega_{ZPL}/2\pi$ (Fig. 4.6a) and linewidth $\Gamma_{DBT}/2\pi$ (Fig. 4.6b) for a single molecule in uncovered, BLG- and MoS_2-covered configurations ($V_g = 0$ V) from data as shown in Fig. 4.4b. Fitting these histograms with a normal distribution, we find that the standard deviations of both ω_{ZPL} and Γ_{DBT} are at most on the order of the lifetime-limited linewidth ~ 40 MHz, which indicates stable emission in all three configurations. The trend of generally larger emission energy fluctuations under MoS_2 electrodes compared to their graphene counterparts is observed in different devices (Fig. 4.6c). To investigate DBT emission stability in the presence of electric fields, we measure emission spectra of the same molecule over time at different backgate voltages V_g (Fig. 4.6d). Fitting these data, we extract the ZPL drift with V_g (Fig. 4.6e), we observe a ZPL drift below 1MHz/s. This sets an upper limit on drift caused by frequency instability of our free-running current-tuned laser. For $V_g \neq 0$ V, the drift amplitude increases to values up to -3 MHz/s, independent of the sign of V_g. We attribute this drift to small but inevitable leakage currents between the 2D and silicon backgate electrodes which modify the electric field experienced by molecules. Considering a simple equivalent circuit model of our device: upon application of a backgate voltage V_g, a leakage current I_L flows through a leakage channel of resistance R_L in series with the device resistance $R \ll R_L$ (formed by the gold electrode and the 2D material) and in parallel to the device capacitance C. This results in a reduced effective voltage $V_{g,eff} < V_g$, due to the potential drop over the leakage resistance, giving rise to a reduced effective electric field strength $E_{eff} \sim \frac{V_{g,eff}}{d}$. Such leakage currents can show non-linear behaviour in V_g and in time, which translates to a transient ZPL drift

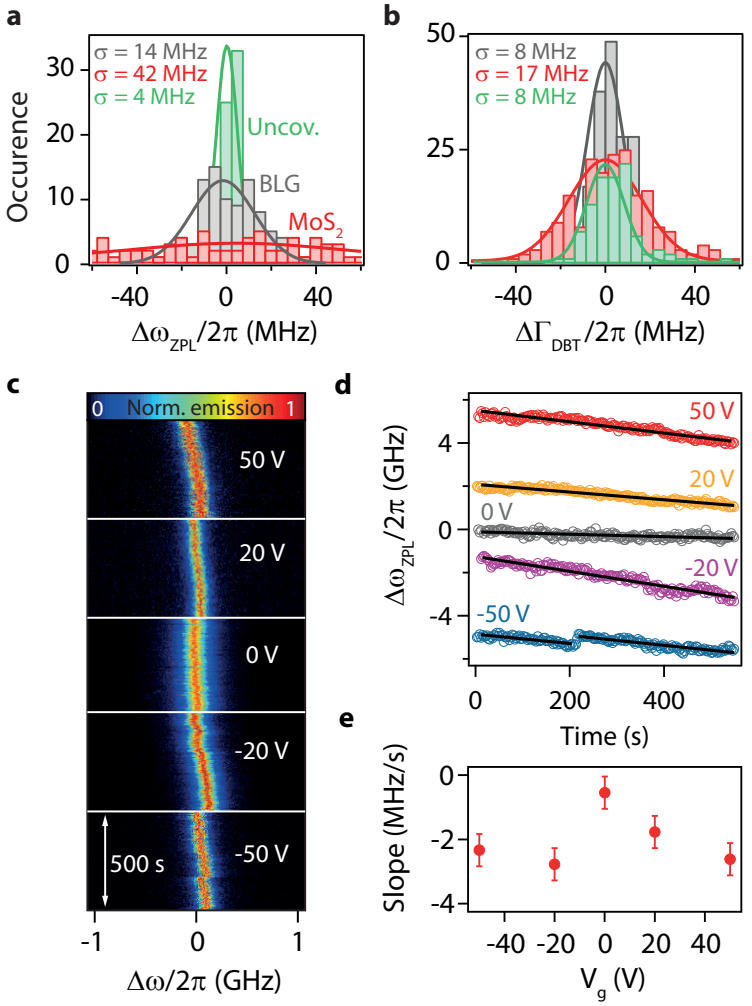

Figure 4.6: Statistics of single molecule emission fluctuation in time: histograms of ZPL frequency **(a)** and linewidth **(b)** fluctuations over a period of 300 s for an uncovered molecule (green) and a molecule covered by MoS_2 (red) and BLG (grey). Solid lines are Gaussian fits to the data, standard deviations are indicated in the figures. **c:** Time trace of single molecule emission (3s / line) in four different devices under graphene and MoS_2 electrodes. **d:** Time trace of single molecule emission (3s / line) under a graphene electrode at different backgate voltages. **e:** ZPL position extracted from data shown in **c**. Data are offset for clarity. Solid lines are linear fits to the data.

$\omega \propto V_{g,eff}^2$ due to the quadratic Stark effect. Nonetheless, these measurements show that ZPL fluctuations are still well below the lifetime-limited linewidth on the timescale of 10 s of seconds even at large V_g. In future experiments, using a stabilised laser and active feedback of emission strength to laser detuning and/or Stark tuning could reduce this drift. Overall, these results show that 2D semiconductors are particularly suitable for integration with sensitive quantum emitters at nanoscale proximity, introducing negligible perturbation in the photostability.

4.3 Electrically modifying the environment of single-photon sources using a 2D electrode

We now turn to electrical manipulation of single emitters. To achieve Stark tuning of DBT emission energy, we apply an electric potential V_g over the capacitor formed by the 2D electrode and the Si^{++} backgate, separated by a PVA/SiO_2 layer (see Figure 4.1a). We reach comparatively large [53] field strengths above 2 MV $\cdot$ cm^{-1} before dielectric breakdown takes place. DBT ensemble spectra below BLG at different V_g (Figure 4.7a) show a large, dominantly quadratic shift of the emitters in the whole ensemble on the order of hundreds of GHz ($\sim 10^4\ \Gamma_0/2\pi$), comparable to the inhomogeneous broadening of the entire ensemble [16]. While this tuning range is comparable to state-of-the-art devices employing semiconductor quantum dots and diamond defects, we highlight that our device displays emission linewidths within a smaller footprint, which is attractive for nanophotonic integration. We also verify that DBT emission energy remains stable under large applied electric fields by repeating stability measurements as shown in Figure 4.4b up to large values of V_g. We find small, gate-dependent emission energy drifts (< 3 MHz/s), likely due to small leakage currents in the device, which can be reduced by using a smaller 2D electrode area or by active feedback.

We remind that the Stark shift is modeled as (see Section 1.2.1):

$$\hbar\Delta\omega_{ZPL} = a|\vec{E}| + b|\vec{E}|^2 \tag{4.1}$$

where a and b are the linear and quadratic Stark coefficients. Here, $\vec{E} = L\vec{E}_{ext} - \vec{E}_0$ is the net local electric field experienced by the molecule upon application of an external field $|\vec{E}_{ext}| = V_g/h_{tot}$, ($h_{tot} = h_{PVA} +$

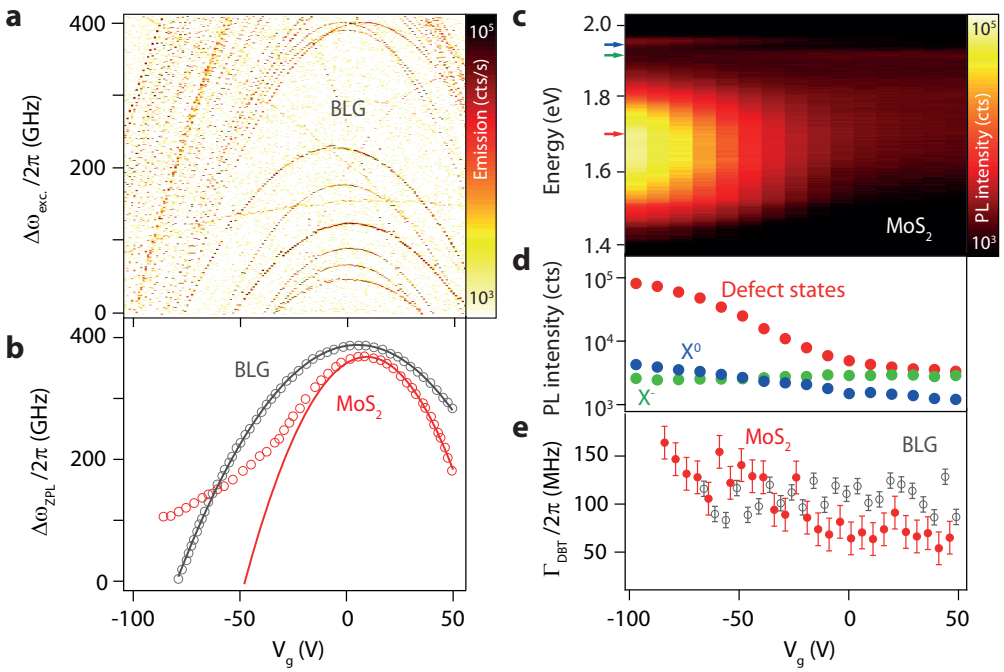

Figure 4.7: Stark tuning of a single molecule with a 2D electrode. **a:** Spectral map showing the Stark shift of an ensemble of single molecules under BLG with backgate voltage V_g. **b:** Gate-induced line shift of a single molecule under BLG (gray circles) and monolayer MoS_2 (red circles). Solid lines are parabolic fits (see main text). **c:** Backgate dependence of MoS_2 photoluminescence (PL) spectra at 532 nm (2.33 eV) excitation. **d:** PL intensity of neutral exciton (X^0, 1.96 eV, blue), negatively charged trion (X^-,1.93 eV, green) and defect band (1.7 eV, red) with V_g. **(e)** Emission linewidth for a single molecule under BLG (gray) and monolayer MoS_2 (red).

$h_{SiO_2} \sim 600$ nm) with a correction $\vec{E}_0$ that accounts for intrinsic electric fields, e.g. due to trapped charges and work function differences. We also include a local field correction factor $L = \frac{\bar{\epsilon}+2}{3} = 1.7$, derived from anthracene's averaged isotropic permittivity [129] $\bar{\epsilon} = 3.1$.

We extract the linear (a) and quadratic (b) Stark coefficients of molecules under graphene and MoS_2 electrodes by fitting the ZPL frequency shift as shown in Fig. 4.7b. As shown in Fig. 4.8, measurements on molecules in different nanocrystals below graphene and MoS_2 electrodes yield typical Stark coefficients of $a \sim 300$ MHz/(kV $\cdot$ cm^{-1}) and $b \sim$ -0.15 MHz/(kV $\cdot$ cm^{-1})^2, comparable to reported results [18]. The observed quadratic

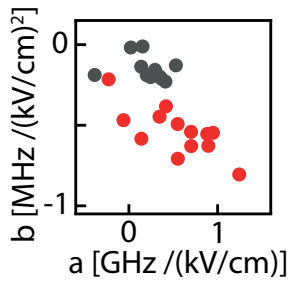

Figure 4.8: Linear **(a)** and quadratic **(b)** Stark coefficients for an ensemble of molecules under graphene (grey) and MoS_2 (red) electrodes.

Stark shift shows that $\vec{E}_{ext}$ is linear in V_g, as is expected for a metallic electrode such as BLG (Figure 4.7b). In contrast, emitters under MoS_2 deviate from the parabolic detuning below $V_{g,0} \sim -30V$ (Figure 4.7b), where the detuning flattens and $\Delta\omega_{ZPL}$ is almost independent of V_g. We attribute this deviation to a gate-induced change of resistivity: as the charge carrier density in a semiconductor changes more abruptly with V_g, we expect a sublinear dependence of $E_{ext}(V_g)$ as excess charge carriers are depleted in MoS_2. Electrostatic doping of the MoS_2 electrode is independently confirmed by gate-dependent photoluminescence (Figure 4.7c,d). The ratio of charged (X^-) to neutral (X^0) exciton PL intensities increases with V_g due to n-doping of the MoS_2 electrode. We also observe a broad emission peak at lower energy for negative V_g - associated with emission from defects in MoS_2 [130] - which overlaps with $\hbar\omega_{ZPL}$. With the appearance of this defect band, we observe a linewidth broadening $\Gamma_{DBT}/2\pi$ below $V_{g,0}$ for some emitters, which is absent in the case of a metallic BLG electrode (Figure 4.7e). This suggests that defects could act as nRET acceptors, leading to emission linewidth broadening of emitters close to MoS_2.

4.4 Dynamical emission control of quantum emitters

Our system combines large Stark tuning with lifetime-limited emitters that potentially enable adiabatic control up to a frequency set by their natural linewidth $\Gamma_0/2\pi$. We investigate the range of this dynamical control by actuating electrically our hybrid devices using a low noise voltage

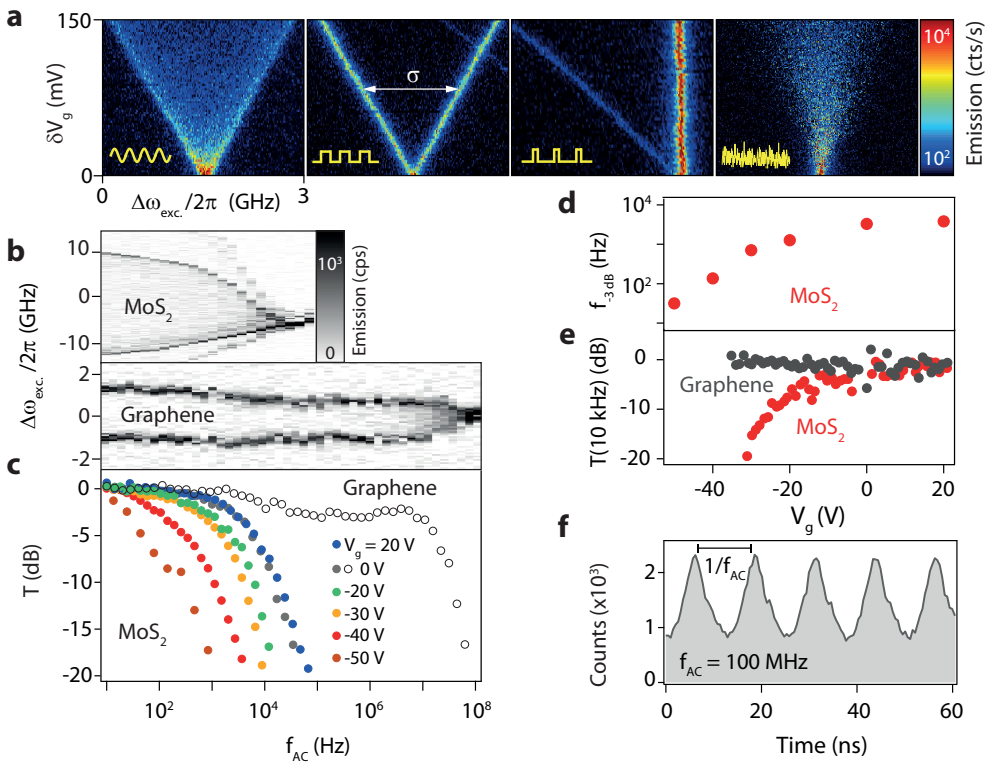

Figure 4.9: Dynamical emission control of quantum emitters. **a:** Single molecule emission as a function of AC amplitude δV_g for (left to right) sinusoidal, square and pulsed modulation (f_{AC} = 1 kHz), and for pink noise (100 kHz bandwidth). **b:** Single DBT emission spectra vs f_{AC} ($V_g + \delta V_g$ = 20 + 1 V) under MoS_2 (upper panel) and monolayer graphene (lower panel). **c:** Transmission function $T(f_{AC})$ for a single molecule at different V_g under MoS_2 (filled circles) and graphene (open circles). **d:** Backgate dependence of MoS_2 cutoff frequency f_{-3dB}. **e:** Transmission T (10 kHz) as a function of V_g for MoS_2 (red) and graphene (grey). **f:** Histogram of time-resolved single molecule emission intensity modulation at f_{AC} = 100 MHz. The transition energy $\hbar\omega_{ZPL}$ is modulated electrically while the excitation energy $\hbar\omega_{exc}$ is kept constant, leading to a periodic emission modulation.

source and an arbitrary waveform generator to provide DC and AC voltages. We apply oscillating potentials $V_{tot} = V_g + \delta V_g(f_{AC})$ to graphene and MoS_2 electrodes. For fast modulation frequencies compared to the spectral acquisition time ($f_{AC} \gg t_{meas}^{-1} \sim 0.1$ Hz), DBT emission peaks show a splitting $\sigma(f_{AC})$ (Figure 4.9a) proportional to the modulation

amplitude δV_g and the local Stark slope $\frac{\partial \omega_{ZPL}}{\partial V_g}$:

$$\sigma = \frac{\partial \omega_{ZPL}}{\partial V_g} \delta V_g \, T \tag{4.2}$$

Here, $T(f_{AC})$ is the transmission of the *RC*-low-pass filter governed by the effective device resistance R which includes contact resistance as well as the sheet resistance of the 2D material and backgate capacitance C.

4.4.1 RC low-pass behaviour of the hybrid device

Fig. 4.10a shows a simplified sketch of our device where a single molecule (SM) is embedded in a PVA layer and lies below a sheet of 2D material at a separation to a gold electrode. The PVA film lies on SiO_2 thermally grown on p-doped silicon (Si^{++}), which acts as a highly conductive backgate electrode. The top electrode of the device is formed by a 2D material of square resistivity ρ_{2D}, which may vary locally due to contamination, local doping and defects. Further, the capacitance to the backgate electrode may also vary over the device area due to local PVA thickness variations, while the SiO_2 is taken to have a constant thickness and capacitance. The propagation of an AC potential $V_{in}(f_{AC})$ applied to the gold electrode to the site of the SM may thus be modeled as the propagation through a transmission line (Fig. 4.10b) defined by the contact resistance and capacitance as well as the local resistance and capacitance defined by the 2D material and PVA film, respectively. Experimentally, we access the field strength due to the potential V_{out} at the SM site via the Stark shift, such that we do not have access to the individual resistance and capacitance components in this transmission line model. To approximate this complex transmission behaviour, we thus model our device as a simple first-order *RC* low-pass filter. This simplest form of an electric low-pass element consists of a resistor R and capacitor C arranged in a circuit as shown in Fig. 4.10c. Its frequency-dependent complex transmission function $\tilde{T}(\omega)$ relates the input and output voltage at angular frequency ω and is readily calculated treating the circuit as a voltage divider: $\tilde{T}(\omega) = \frac{V_{out}(\omega)}{V_{in}(\omega)} = \frac{\frac{1}{j\omega C}}{R+\frac{1}{j\omega C}} = \frac{1}{1+j\omega RC}$. For what follows, we use frequency $f_{AC} = \frac{\omega}{2\pi}$ to describe the experimentally applied AC drive frequency. The transmission amplitude thus follows the relation:

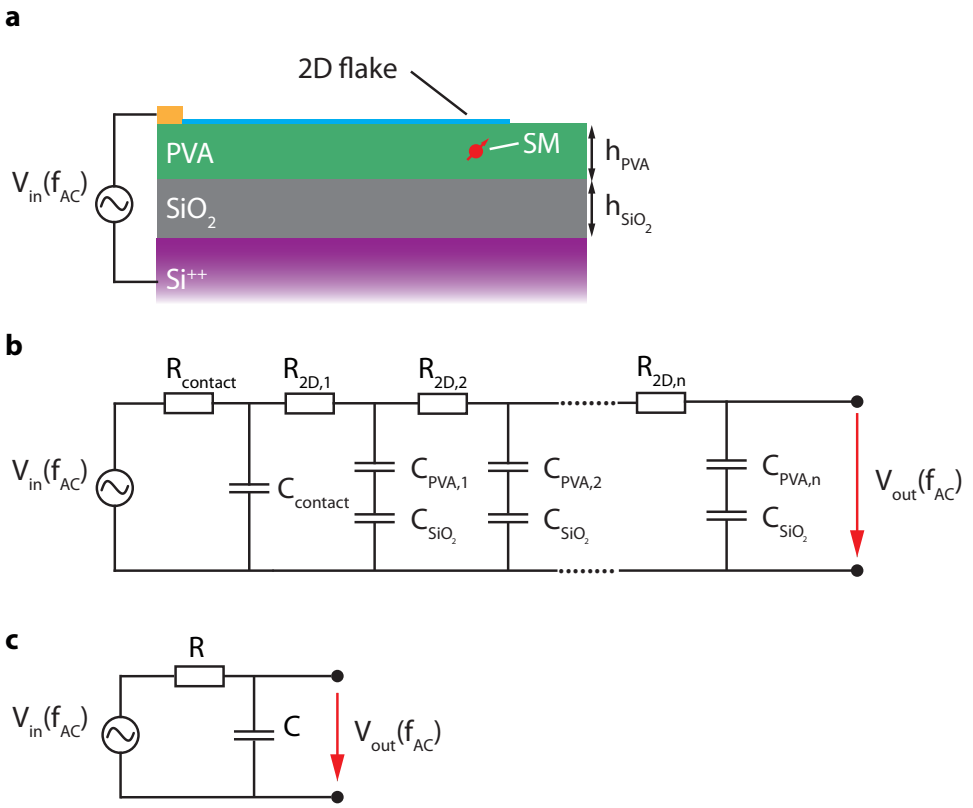

Figure 4.10: RC low-pass behaviour of the hybrid device. **a:** Device schematic, showing the dielectric layer formed by PVA and SiO_2 and the embedded single molecule (SM) underneath the 2D material flake (blue). AC voltages are applied to a gold electrode contacting the flake. **b:** Transmission line model of the device consisting of a series of n RC elements defined by local device properties. **c:** Simplified device model: first-order RC low-pass circuit.

$$T(f_{AC}) = |\tilde{T}(f_{AC})| = \frac{1}{\sqrt{1+(2\pi f_{AC} RC)^2}} = \frac{1}{\sqrt{1+(f_{AC}/f_{-3dB})^2}} \quad (4.3)$$

and shows low-pass behaviour with a characteristic cut-off frequency $f_{-3dB} = \frac{1}{2\pi RC}$ for which $T(f_{-3dB}) = 1/\sqrt{2}$. This expression shows that an increase of resistance R, for instance due to gate-induced doping of a 2D material, leads to a lower cut-off frequency, as is observed in Fig. 4.9d.

4.4.2 Extracting the cut-off frequency of a 2D low-pass filter from single photon emission

At fixed V_g and f_{AC}, the DBT emission spectra reflect the oscillation turning points of the modulating waveform (Figure 4.9a). Under square modulation with a fixed amplitude δV_g, the splitting vanishes with increasing f_{AC} for both MoS_2 and graphene electrodes (Figure 4.9b), albeit at a lower frequency for MoS_2. From this measurement, we extract $T(f_{AC})$ (4.2) and confirm low-pass behaviour with a characteristic cut-off frequency f_{-3dB} (Figure 4.9c). Interestingly, $T(f_{AC})$ shows a strong gate voltage V_g dependence for MoS_2 electrode, which is not observed for graphene. This dependence is quantified by f_{-3dB}, which increases with V_g and saturates at $\sim 5kHz \ll \Gamma_0/2\pi$ for $V_g > 0$ V (Figure 4.9d). We attribute this behaviour to a change of sheet resistivity and contact resistance due to gate-induced electrostatic n-doping of the MoS_2 consistent with PL measurements (Figure 4.7c,d). As a result, $f_{-3dB} \propto (RC)^{-1}$ increases as we sweep V_g from negative to positive values.

4.4.3 High-frequency modulation of the emission intensity of a single molecule

To capture the gating efficiency of our 2D electrodes, we extract transmission T at fixed f_{AC} = 10 kHz varying V_g (Figure 4.9e). The strong reduction of T for $V_g < 0$ V is consistent with a large gate-induced change of resistance in the semiconducting MoS_2 device, while graphene's metallicity maintains $T \sim 1$ over the full V_g range. Therefore, graphene enables Stark tuning of emitters over a large energy range and at high frequency at the expense of weak linewidth broadening. To extend this modulation bandwidth, we reduce the gate capacitance C by using a thicker PVA dielectric (h_{PVA} = 800 nm). Then, we modulate $\hbar\omega_{ZPL}$ around a fixed excitation energy by applying δV_g at f_{AC} = 100 MHz $\sim \Gamma_0/2\pi$ to a graphene electrode. Using a time-correlated single-photon counter synchronized to the modulation δV_g, we observe a periodic oscillation of emission intensity (Figure 4.9f) with a modulation depth of $\sim$ 50% (measurement time 30 s). This oscillation is a signature of the excitation laser periodically exploring a fraction of the emitter's absorption line. These measurements show that the dynamical modulation bandwidth of our devices, determined by the 2D electrode material and device geometry,

approaches $\Gamma_0/2\pi$. Conversely, single emitters act as local nanoprobes of the 2D material's electronic properties.

4.5 Conclusions

In this chapter, we demonstrate a hybrid device where 2D materials are integrated with lifetime-limited single photon emitters to achieve broadband and fast emission energy tuning [126]. Our results highlight the potential of atomically thin electrodes for integration with sensitive quantum emitters in a nanoscale device without perturbing narrow emission linewidth, in contrast to commonly employed bulk transparent electrodes. At high frequencies, Stark modulation reveals low-pass transmission behaviour related to the 2D materials' sheet resistivity. Using a graphene electrode, we show emission energy modulation at frequencies approaching the emitters' linewidth. Our device thus provides resonant tuning and high-frequency modulation of SPS on chip, required for obtaining indistinguishable and synchronised single photons. Finally, our device is a platform for studying novel forms of light-matter interaction with plasmon-polaritons in graphene [123] and exciton-polaritons in TMDs [124] at the single excitation level. Conversely, strong coupling to such excitations could allow the observation of normally forbidden higher-order transitions of the emitter [131].

Electrical control of lifetime-limited quantum emitters using 2D materials

- We built a hybrid capacitive device combining single organic molecules with 2D transparent electrodes
- We electrically tuned the DBT emission energy by Stark effect up to 10^4 times the emission linewidth
- We dynamically controlled the quantum emission by electrically actuating the device with an AC voltage
- We reached high-frequency modulation of the emission intensity of a single molecule up to the order of magnitude of the emission linewidth

Chapter 5

Single molecules as sensors of local electric fields in graphene

Sensitive nanoscopic probes of electric and magnetic fields play a key role in the study of material properties at the nanoscale. Nano-imaging of electric and magnetic properties [132], current flows [133] and noise sensing [134] has been demonstrated.
Nanoscale sensing of magnetic fields has been performed successfully using nitrogen vacancy centres (NVCs) in diamond at room temperature [135]. These systems have a high sensitivity to magnetic field (0.5 μT $\cdot$ Hz$^{-1/2}$ [135]). They are also able to detect individual charges (electric field sensitivity of 202 ± 6 V $\cdot$ cm$^{-1}\cdot$ Hz$^{-1/2}$, corresponding to the electric field produced by a single charge positioned at a distance of $\sim$ 150 nm from the spin sensor) [136].
As for electric field sensing, single-electron transistor scanning (SET) - with a charge sensitivity of a small fraction of an electron [137] - and atomic-like charge qubit in carbon nanotubes - with better electric field sensitivity than SET and similar magnetic field sensitivity to NVCs [132] - have shown the best results.
In this Chapter we study a different technique to measure electric fields at the nanoscale. This is based on the Stark effect induced by an external electric field on the energy levels of an organic molecule. As a result, we observe a shift in the emission energy of the two-level system (see Chapter 1). A narrow linewidth implies a higher sensitivity of the system to applied electric fields. DBT molecules with their narrow emission at cryogenic temperatures are therefore an ideal system to detect small

changes in the external electric field. At low temperature we are able to spectrally resolve single molecules thanks to their narrow linewidths (see Section 2.3.1). Each molecule has a different dipole orientation which results in different Stark effect parameters. This makes it possible to follow the behaviour of individual molecules up to high electric fields without broadening their signal, opening the way for a better understanding of the influence of an applied electric field at microscopic scale.
DBT molecules display a strong Stark effect [126]. Assuming an average linewidth of $\Gamma_{DBT}/2\pi = 100$ MHz and emission counts of the order of $N \sim 10000$, in the shot-noise limit the smallest shift detectable by the molecules is $\frac{\Gamma_{DBT}}{2\pi} \cdot \frac{\sqrt{N}}{N} \sim 1$ MHz. From the Stark shift formula presented in Section 1.2.1 we extract an electric field resolution of 3 V $\cdot$ cm^{-1} corresponding to such shift. The possibility of integrating these sensitive probes in a non-invasive way into more complex devices, such as 2D devices, and the ability to address single emitters with measurements at cryogenic temperatures, make these molecules valuable candidates for electric field sensing.

Here, we will present how the deposition of DBT-doped nanocrystals on top of a 2D device allows to map the electric field response from different positions of a 2D device. We will show anomalous results of the Stark effect at the edge of the 2D device suggesting a different charging behaviour of some local point defects, which we will describe with an electrostatic model.

5.1 Hybrid device integrating solid-state single-photon emitters with a graphene field effect transistor

The spincoating technique illustrated in Section 3.1 allows us to easily integrate anthracene nanocrystals (NCs) doped with DBT molecules into a nanoscale device by embedding the NCs in a layer of poly(vinyl alcohol) (PVA). Although we have no control on the final position of the NCs, increasing their density in PVA garantees a good coverage of the coated device.
Figure 5.1a shows a schematics of the device made of a single layer graphene flake, bottom encapsulated with a thin hBN layer of approximately 50 nm thickness, on top of 285 nm of SiO_2 deposited on a n-doped

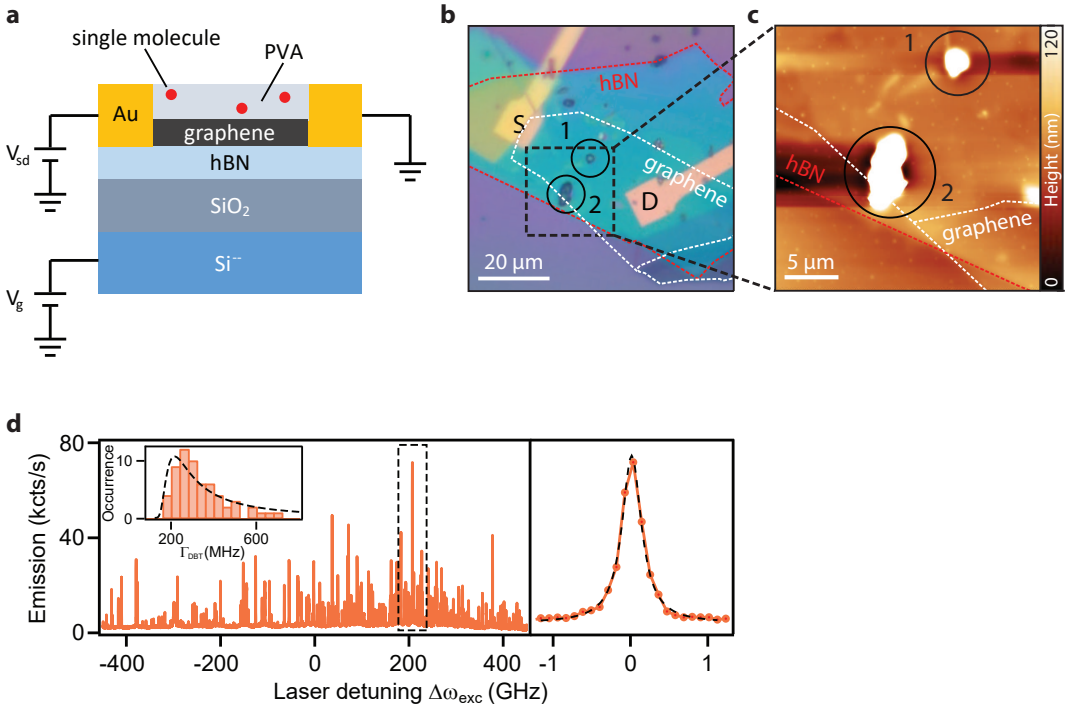

Figure 5.1: Graphene field effect transistor (FET) integrated with single organic molecules. **a:** Sketch of the graphene FET and measurement schematics. Nanocrystals doped with single molecules are deposited at the centre and at the edge of the graphene device. **b:** Optical microscope image of the graphene device with source (S) and drain (D) electrodes. 1 and 2 doped nanocrystals are deposited respectively at the centre and at the edge of the graphene flake. **c:** AFM tomography image of the area highlighted in **(b)**. **d:** Typical emission spectrum of one doped nanocrystal and zoom on one molecule's emission with linewidth 300 MHz as extracted from the Lorentzian fit (dashed line). In the inset is presented the histogram of linewidth distribution for more than 60 molecules.

silicon chip. Two gold contacts, source (S) and drain (D), evaporated on top allow us to apply a source-drain bias (V_{sd}) to graphene, hence to control the current flow through the device.
We then spincoat a layer of PVA doped with DBT molecules on top of the graphene field effect transistor (FET) as explained in Section 3.1. In the case of the device presented, we successfully deposited one NC at the centre (position 1) and one at the edge (position 2) of graphene (see Fig. 5.1b), which is an interesting configuration to explore the behaviour

of the two areas of graphene. The AFM scan in Figure 5.1c highlights the edges of the bottom hBN and graphene single layer flake. NCs 1 and 2 are shown as well, but with heights of more than 400 nm and 1 μm respectively they appear out of the chosen scale.
The molecules deposited on the sample are characterized using the laser spectroscopy technique presented in Chapter 2. Figure 5.1d shows multiple peaks, each corresponding to one molecule excited in the NC, measured spectrally by scanning the excitation energy through each resonance. The emission peak of one molecule (highlighted in dashed line) is zoomed on the right of Fig. 5.1d and fitted with a Lorentzian function providing a full width at half maximum of 300 MHz. In the inset we show the linewidth occurrence for a sample of more than 60 molecules measured on the sample. The histogram peaks at 215 MHz as a result from fitting it with the Smirnov distribution function [128]. The average linewidth is broader compared to state-of-the-art ones because of the presence of graphene causing broadening via non-radiative energy transfer [126].

5.2 Electrostatic measurements at the centre and edge of graphene via Stark shift

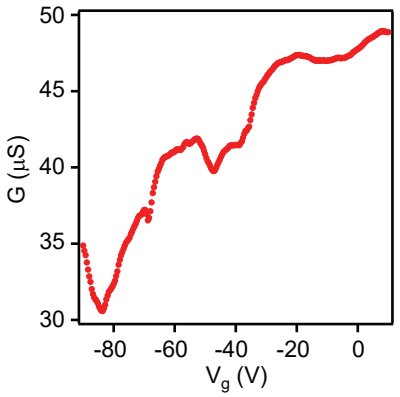

Figure 5.2: Transport characteristics of the graphene-based FET. Neutrality point of the device is around $V_g \sim$ -80 V.

Thanks to the geometry of our device (see Figure 5.1a) we can address the following question: how does the electric field $\vec{E}(\vec{r})$ generated by

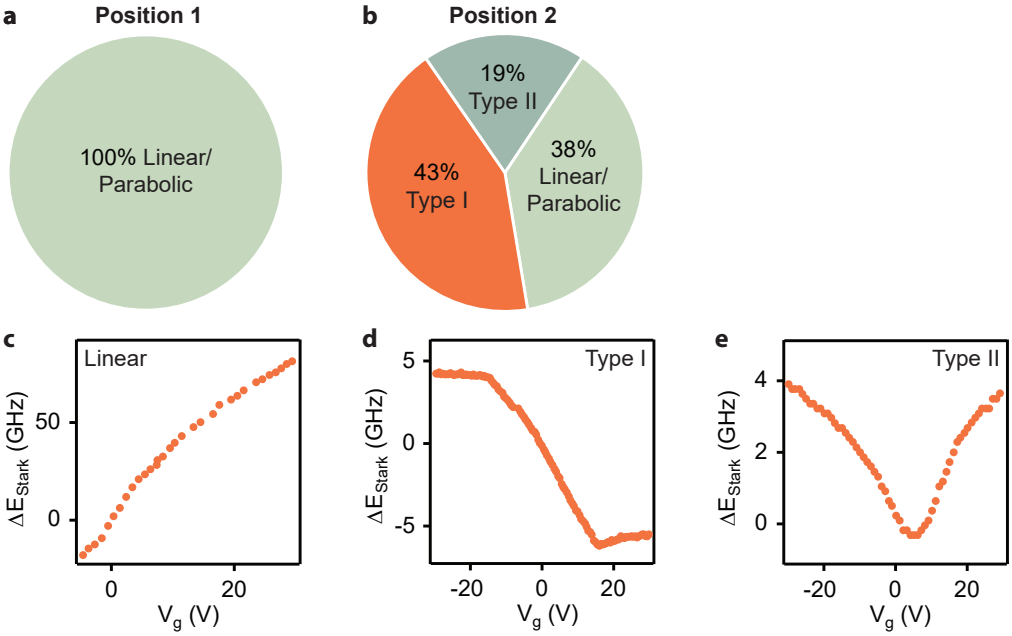

Figure 5.3: Detecting local electrostatic states in graphene via Stark shift. **a:** For more than 80 molecules measured in nanocrystal 1 (at the centre of graphene) we observe 100% linear or parabolic Stark shift. **b:** Response in energy shift as a function of V_g for molecules in nanocrystal 2, positioned at the edge of graphene. For more than 190 molecules detected, approximately 38% exhibit linear or parabolic Stark shift (**c**), while 43% show an atypical Z-shaped behaviour (Type I, **d**) and 19% show an atypical V-shaped behaviour (Type II, **e**).

graphene differ at a position $\vec{r}$ at the centre from the edge of the device? The relevance of this question is supported by the fact that the difference in behaviour of graphene at the edge and in bulk is still an open question. For instance, a full understanding of the role of dangling bonds and charge defects at the edge as well as of the contribution of graphene edge states to the device's conducting properties are still lacking [138].
To read out the nature of the electric field generated by graphene we observe the shift of the molecules' emission energy. The typical linear and parabolic Stark effect of organic molecules (see Section 4.3) have been extensively studied in literature [18, 19, 52, 53, 139] typically in capacitive geometries. In the geometry of our device the molecules lie on top of graphene, where we theoretically expect zero electric field, even though the picture is more complex than that as it will be discussed later

in Section 5.4.
First, we characterize the device using the source and drain electrodes shown in Figure 5.1a by measuring the graphene conductance G as a function of the applied backgate V_g. We remind that the conductance is defined as $G = I_{SD}/V_g$, where I_{SD} is the current flowing from source (S) to drain (D) electrodes. The graph in Figure 5.2 shows that our device is heavily n-doped with a neutrality point around $V_g \sim$ -80 V.
Then, we explore the behaviour of molecules in the NC at the centre (1) and edge (2) of the graphene device. For an ideal graphene sheet, we expect to have $|\vec{E}| = 0$ above the flake since we are in a parallel plate capacitor geometry and graphene is behaving like a metal.

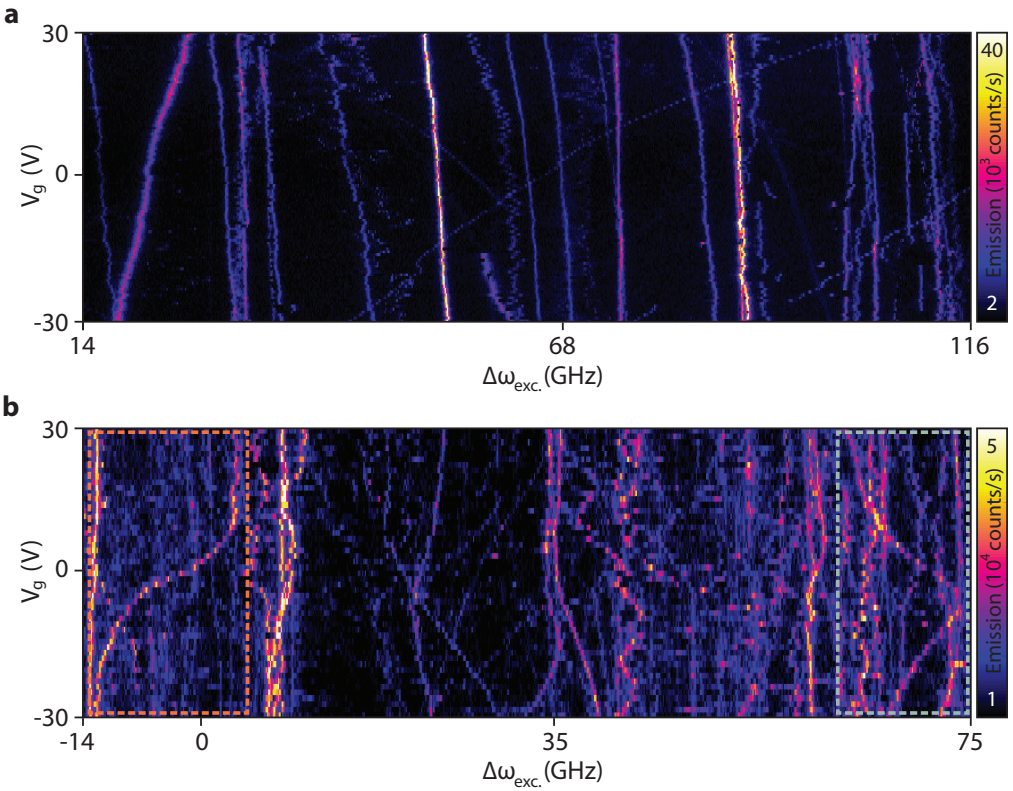

Figure 5.4: DBT molecules spectra as a function of the backgate voltage V_g. **a:** Above bulk graphene (position 1) we observe typical linear and parabolic Stark response. **b:** At the edge of graphene (position 2) we observe linear and parabolic Stark response as well as exotic Z-shaped (highlighted in orange) and V-shaped (in green) type of behaviours.

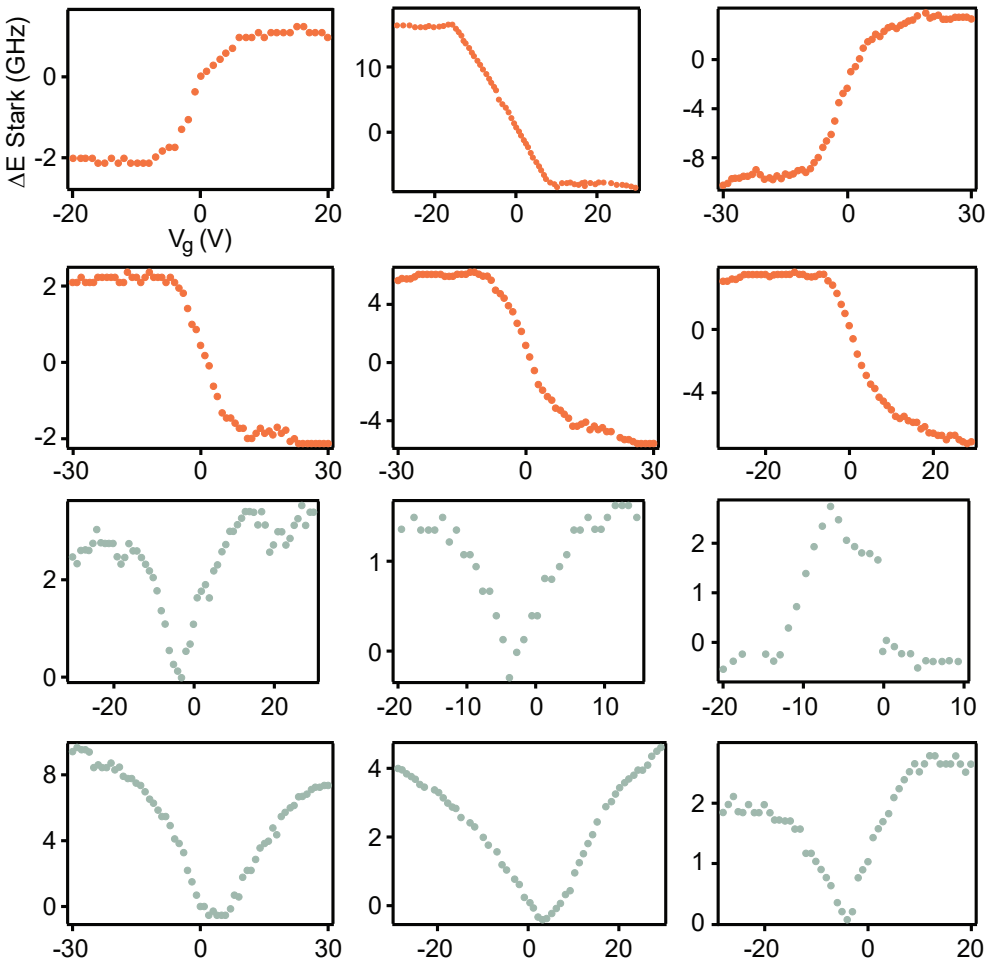

Figure 5.5: Anomalous Type I (orange) and II (green) Stark response have been measured multiple times from molecules in nanocrystal 2.

The measurement procedure is the same both at the centre and the edge. We position the laser at the centre of the NC and detune its energy within the inhomogeneous broadening of DBT molecules in the NC ($\Delta\omega_{ensamble}/2\pi >$ 200 GHz - 1 THz). Since the laser has a narrow linewidth < 1 MHz $\ll \Gamma_{DBT}/2\pi$ we are able to isolate the spectrum of each molecule (for more details refer to Chapter 2). We repeatedly collect one full spectrum of more than 100 molecules while modifying the backgate voltage V_g from -30 to 30 V, as shown in Figure 5.4a. For NC 1 we observe that all the samples detected (a total of 83 molecules) show a linear or parabolic Stark shift (see 5.3a). This effect disagrees

with our prediction that the electric field above bulk graphene should be zero at first approximation. However, in graphene charge carriers behave as two-dimensional Dirac fermions [140] and are subjected to microscopic perturbations such as corrugations and electron-density inhomogeneities (charge puddles) [141, 142] the field is not completely balanced and molecules can feel a non-zero in-plane electric field at the centre of graphene as well.

At the edge of graphene, the detuning map at different backgate voltages (see Fig. 5.4b) shows a more diverse family of behaviours. In addition to the typical linear and parabolic Stark response we observe repeatedly exotic Z-shaped (highlighted in orange) and V-shaped (in green) type of behaviours, referred to as Type I and Type II respectively form now on. Figure 5.3b is a visual representation of the response of 194 molecules in the crystal at the edge of graphene. 38% of them show a typical linear or parabolic Stark behaviour (see 5.3c). 43% of them show a linear Stark shift behaviour saturating for positive and negative backgate voltages (Type I, see 5.3d). Together with this unexpected response, 38% of the molecules show a non-monotonic "V" shape saturating as well for positive and negative backgate voltages (Type II, see 5.3e).
Figure 5.5 shows the reproducibility of the exotic Type I and II Stark behaviours for several molecules in the same NC at the edge of graphene. We also notice that the saturation reached by molecules at positive and negative backgate voltages is symmetric around V_g = 0 V, while the device showed neutrality point at $V_g \sim$ -80 V (see Fig. 5.2).
The main anomalies in Stark shift observed from molecules in nanocrystal 2 (different types of behaviour, saturation regimes, symmetry around V_g = 0 V) support the assumption of some local defects charging at the edge of graphene, for which a proper model will be developed in the next section.

5.3 Modeling defects in graphene using the Stark effect

To understand the experimental results presented in Section 5.2 we develop a theoretical model with the help of Dr. Iacopo Torre. We assume that a point defect is located at the edge of graphene and we model it as a conducting sphere which gets charged as well as graphene when

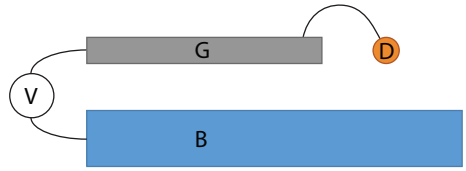

Figure 5.6: Simple schematics of a graphene capacitive device with a point defect, represented as a conducting sphere, connected to the edge.

modifying the backgate potential V_g. Starting from simple electrostatics and taking into account that the electrostatic potential is linear, in the configuration illustrated in Figure 5.6 the total electrostatic potential is:

$$\phi(\vec{r}) = \phi_G f_G(\vec{r}) + \phi_D f_D(\vec{r}) + \phi_B f_B(\vec{r}) \tag{5.1}$$

where ϕ_G, ϕ_D and ϕ_B are the electrostatic potentials of the graphene, the defect and the backgate respectively and $f_G(\vec{r})$, $f_D(\vec{r})$ and $f_B(\vec{r})$ are the respective functions taking into account the contribution of each potential at a position $\vec{r}$ in space. Assuming that the backgate is set to ground and that we apply the potential through the top gate we can set $\phi_B = 0$. The electric field $\vec{E}(\vec{r})$ generated by graphene and the defect at a position $\vec{r}$ becomes:

$$\begin{aligned} \vec{E}(\vec{r}) &= -\phi_G \nabla f_G(\vec{r}) - \phi_D \nabla f_D(\vec{r}) \\ &= -V_g \nabla f_G(\vec{r}) - \phi_D[V_g] \nabla f_D(\vec{r}) \end{aligned} \tag{5.2}$$

In Equation 5.2 we make the assumptions that $\phi_G = V_g$ since the system is at equilibrium and that ϕ_D is a function of V_g, being connected to graphene.
We use the Stark shift formula introduced in Section 1.2.1 and expressed as in [18]:

$$\hbar\delta\omega = -\delta\vec{\mu} \cdot \vec{E}(\vec{r}) - \frac{1}{2}\vec{E}(\vec{r}) \cdot \delta\bar{\bar{\alpha}} \cdot \vec{E}(\vec{r}) \tag{5.3}$$

By replacing Eq. 5.2 in Eq. 5.3 we get:

$$\hbar\delta\omega = aV_g + bV_g^2 + a'\phi_D[V_g] + b'V_g\phi_D[V_g] + b''(\phi_D[V_g])^2 \tag{5.4}$$

We are looking for a solution of Equation 5.4 providing the relation

between the electrostatic potential of the defect ϕ_D and the applied backgate potential V_g. We assume that graphene and the defect are connected, hence at equilibrium they share the same electrochemical potential μ_T, while the bottom electrode has an electrochemical potential μ_B. The difference between the two the electrochemical potential is fixed by the backgate voltage V_g as follows:

$$\mu_T - \mu_B = -eV_g \tag{5.5}$$

where e is the elementary charge.

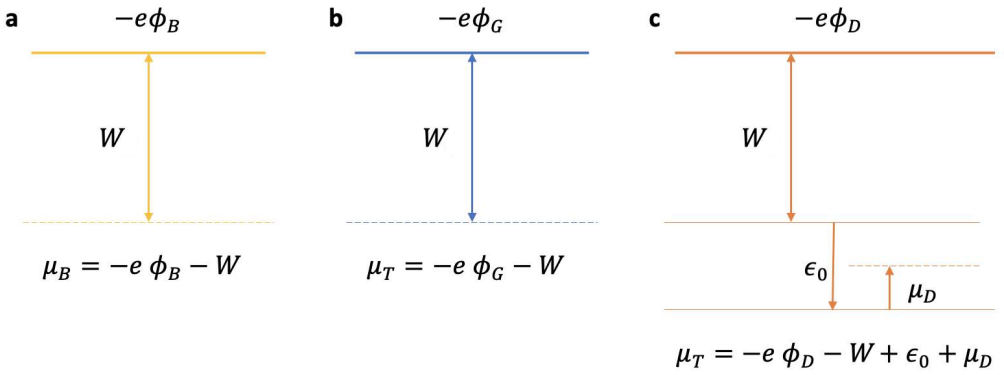

Figure 5.7: Energy diagrams for the three elements of the device: bottom gate (**a**), graphene (**b**) and the defect (**c**).

Going a bit more in depth into the energy diagrams of the three elements of our system, we model the bottom gate as a perfect metal with work function W and vacuum energy level $-e\phi_B$ (see Fig. 5.7a), therefore the electrochemical potential is:

$$\mu_B = -e\phi_B - W \tag{5.6}$$

where we set $\phi_B = 0$ as mentioned before in this section.
Graphene is modeled as having a work function W and vacuum energy level $-e\phi_G$ (see Fig. 5.7b). Considering the transport characteristic shown in Figure 5.2, we are far from the charge neutrality point of the device hence graphene behaves like a metal and the quantum capacitance effect is negligible. Quantum capacitance is the effect happening when graphene is close to the charge neutrality point, hence the charge density is low and electric field leaks through the graphene top gate. As a result, we can assume that there's no shift in the electrochemical potential due

to doping ($\mu_G = 0$). The electrochemical potential of the top electrode becomes $\mu_T = -e\phi_G - W$.
Finally the defect is represented as having a work function $W_D = W + \epsilon_0$ taking into account a small correction ϵ_0 between the work function of graphene and the impurity level. From the corrected energy level of the impurity we calculate the electrochemical potential of the defect μ_D (see Fig. 5.7c) and we can write the relation:

$$\mu_T = -e\phi_D - W - \epsilon_0 + \mu_D \tag{5.7}$$

We have assumed that the three elements have the same work function as we are at equilibrium and don't expect charge tunneling between bottom and top gate.
By substituting Equations 5.6, 5.7 in Equation 5.5 we obtain an equation of the electrostatic potential ϕ_D and the shift in electrochemical potential of the defect μ_D:

$$-eV_g = -e\phi_D + \epsilon_0 + \mu_D \tag{5.8}$$

To solve this equation we model the charge occupation of the impurity level Q_D using the Fermi function n_F calculated at the energy of the defect:

$$Q_D = Q_0 - egn_F(-\beta\mu_D) \tag{5.9}$$

where Q_D is the number of charges on the defect, Q_0 is the number of charges at zero bias, g is the degeneracy of the defect taking into account that each defect could host pairs of electrons with opposite spins, n_F is the Fermi function describing the population of the impurity level at energy $-\beta\mu_D$, with $\beta = \frac{1}{k_B T}$. Extracting μ_D from Equation 5.8 and substituting it into Equation 5.9 we obtain an expression as function of the electrostatic potential of the defect ϕ_D:

$$\begin{aligned} -egn_F[\beta(eV_g - e\phi_D + \epsilon_0)] + egn_F[\beta\epsilon_0] &= C_{GD}\phi_G + C_D\Phi_D \\ &= C_{GD}V_g + C_D\phi_D \end{aligned} \tag{5.10}$$

where we have replaced $\phi_G = V_g$ as commented before in this section and assumed neutrality of the defect at $V_g = 0$V.
In the low temperature regime, which is the one we are interested in

since all our measurements are performed at 3K, the Fermi function becomes sharper around the electrochemical potential value [143] and can be substituted in Equation 5.10 by a step function:

$$\theta(-e\phi_D + eV_g + \epsilon_0) - \theta(\epsilon_0) = \frac{C_{GD}}{eg}V + \frac{C_D}{eg}\phi_D \tag{5.11}$$

where C_{GD} is the capacitance between graphene and the defect, C_D is the capacitance of the defect which being modeled just as conducting sphere is proportional to its radius. We can assume that $C_{GD} \ll C_D$ because of the geometry of our device.

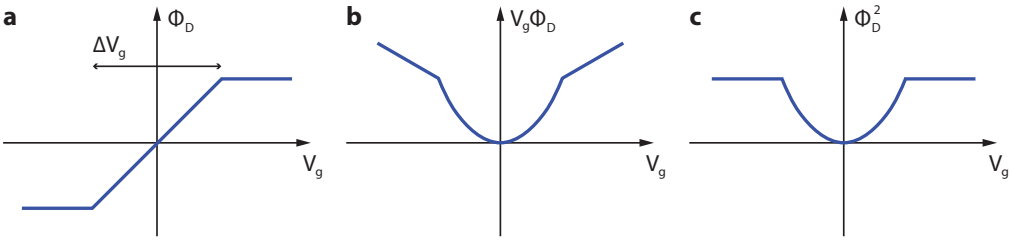

Figure 5.8: Model of the electric field generated by a defect in graphene. **a:** Solution of the linear term in $\phi_D[V_g]$ of the Stark effect discussed in the text. The electrostatic potential of the defect ϕ_D follows a linear behaviour within a voltage ΔV_g and then saturates. The solutions to the mixed **(b)** and quadratic **(c)** terms of the Stark shift present similar saturation behaviours.

The solution $\phi_D[V_g]$ of Equation 5.11 is shown in Figure 5.8a. The defect's electrostatic potential shows a linear behaviour with slope $\Delta\phi_D/\Delta V_g = 1$ corresponding to the phase in which the defect is charging. This regime is symmetric around 0 in a range $\Delta V_g \simeq \frac{eg}{C_D}$ representing the charging energy of the defect. Outside of this regime the electrostatic potential saturates. This behaviour, which is the solution of the linear term $\hbar\delta\omega = a'\phi_D[V_g]$ of Eq. 5.4, agrees well with the experimental results presented in Figure 5.4a for the Type I Stark shift. The solutions of the mixed and quadratic terms $\hbar\delta\omega = b'V_g\phi_D[V_g] + b''(\phi_D[V_g])^2$ of Eq. 5.4 are presented respectively in Fig. 5.8b,c and once again they fit well the Type II Stark behaviour we observed (see Fig. 5.4b).

5.4 Gaining information on the defect by fitting the Stark effect

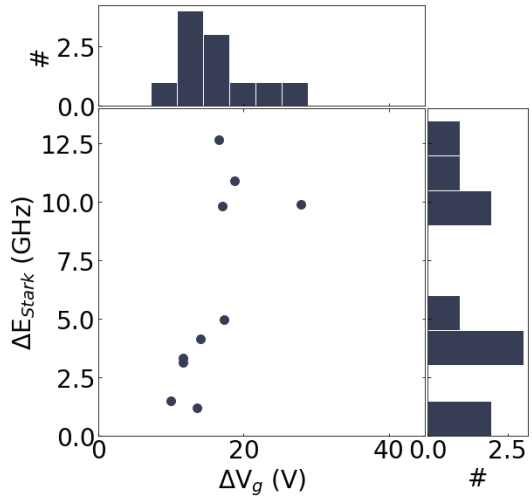

Figure 5.9: Distribution of the energy shift ΔE_{Stark} as a function of the relative shift in potential ΔV_g for the linear regime between bottom and top saturation of several Type I molecules in the nanocrystal at the edge of graphene. The lateral histograms highlight that ΔV_g is narrowly distributed around the value $\overline{\Delta V_g} = 12 \pm 4$ V, while ΔE_{Stark} is spread over a broader range (approximately 13 V).

In order to prove the strength of the model presented in Section 5.3 and to gain information about its parameters, we test it on the Stark effect of several molecules measured in the nanocrystal positioned at the edge of graphene (NC 2). We proceed to fit several molecules showing Type I Stark shift. We focus on Type I behaviour for simplicity but this interpretation can be well extended to Type II. From the fit we can extract the shift in energy ΔE_{Stark} between the bottom and top saturation, as well as the corresponding shift in backgate potential ΔV_g. Figure 5.9 shows the distribution of ΔE_{Stark} as a function of the relative ΔV_g for ten molecules in NC 2 showing Type I Stark shift. We observe that the span in ΔV_g is rather narrow (from the Gaussian fit of the histogram distribution we extract $\overline{\Delta V_g} = 12 \pm 4$ V). This result suggests that all the molecules are sensing the same defect or many defects with a similar charging behaviour. On the other hand, the shift in energy ΔE_{Stark} spreads over a

bigger range of 13 V ($\overline{\Delta E}_{Stark} = 8 \pm 6$ V). The dispersion of ΔE_{Stark} can be attributed to the position of the molecule with respect to the defect as well as to the direction of the molecule's polarization with respect to the field lines which plays a role in the Stark coefficients.
The charging energy ΔV_g obtained fitting the data can provide information on the size of the defect. Assuming $\Delta V_g \sim 20$ V, we can use the following equation:

$$\Delta V_g \simeq \frac{eg}{C_D} \sim 20V \tag{5.12}$$

to extract the defect capacitance C_D. Considering for simplicity that the degeneracy $g = 1$ and remembering that the defect is modeled as a sphere with capacitance $C = 4\pi\epsilon_0 R$, we can extract the radius R of the defect sphere which is of the order of 10^{-11} m, comparable to the Bohr radius a_0, suggesting that the defect is of atomic size. As we have no way to verify the value of the degeneracy, this calculation might as well work for defects with degeneracy $g \gg 1$ containing g charges.

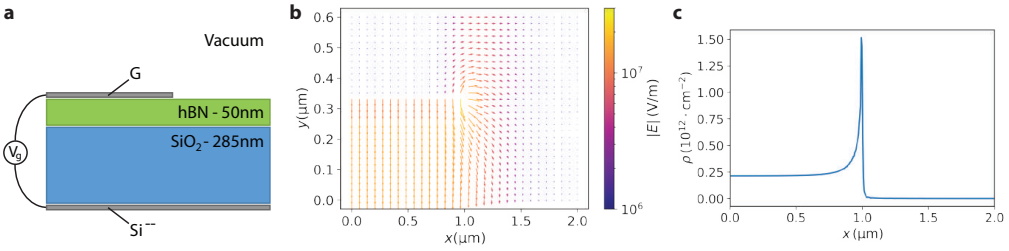

Figure 5.10: Modeling the electric field lines generated by graphene. **a:** Capacitive model where a potential difference V_g is applied between the top graphene (G) and the bottom Si^{--} electrodes. The two electrodes are separated by 50 nm hBN + 285 nm SiO_2. **b:** Direction and intensity of the electric field lines rotating at the edge of graphene. **c:** Charge density above and outside graphene. The position $x = 1$ μm corresponds to the edge of the device.

The electrostatic model of the defect describes well the anomalous saturation behaviour observed only in NC 2 at the edge of graphene. Yet, to explain the difference between Type I and Type II behaviours we have to look into the direction of the field lines above and at the edge of graphene. We use a capacitive model as the one shown in Figure 5.10a, where a potential difference V_g is applied between the top graphene and

the bottom Si^{--} electrodes. Figure 5.10b shows that inside the capacitor the field lines are vertical and uniform as expected. That's because graphene behaves as a metal since we are far from the charge neutrality point of the device, as discussed previously in this section. At the edge though, lines coming from the bottom electrode have to rotate to reach graphene. The density of these lines decreases exponentially moving from the edge to the top-centre of the graphene flake, as confirmed by the model of the density of charges which decreases exponentially starting from the edge (see Fig. 5.10c).
The geometry of our device plays a role in the different Stark behavious as well. NC 2 is positioned at the edge of graphene and has approximate length 7 μm, width 3 μm and height 1.3 μm. Despite the attempts to perform super-localization as described in Chapter 2, the oblong shape of the anthracene crystal, with a similar refractive index to the PVA layer, is responsible for strong guiding of light therefore preventing the correct positioning the molecules within the NC. This super-localization technique might be repeated with a smaller and more regular crystal, on which it has already proven to be successful (see Chapter 2).
In case of NC 2, the molecules we are detecting might be distributed all over the nanocrystal. The position of each molecule in the nanocrystal corresponds to a different position with respect to graphene, that is a different orientation of the electric field lines with respect to the molecular dipole. It's important to remember that, as described in Chapter 2, we excite the molecules with a linearly polarized laser with polarization in-plane with the device. Because of our measurement technique we are able to detect only molecules which have a large component of the transition dipole moment along the laser polarization [53]. Despite knowing the orientation of the transition dipole, the change in dipole moment between ground and excited state $\delta\vec{\mu}$ introduced in Equation 5.3 can be oriented in any direction. The scalar product $\delta\vec{\mu}\cdot\vec{E}$ in the Stark shift formula (Eq. 5.3) happens to be maximum in case of molecules for which $\delta\vec{\mu}$ is parallel to the electric field lines. In this configuration linear Stark shift is dominant and Type I behaviours are predominant. When, on the other hand, the molecule is in a position where $\delta\vec{\mu}$ is orthogonal to the electric field lines, the linear term becomes negligible and mostly the parabolic Stark term plays a role in Eq. 5.3. This is the case of Type II molecules.

Fitting the raw data of several Type I and II molecules using Eq. 5.3 and substituting as $\vec{E}(\vec{r})$ the solution to the electrostatic equation shown

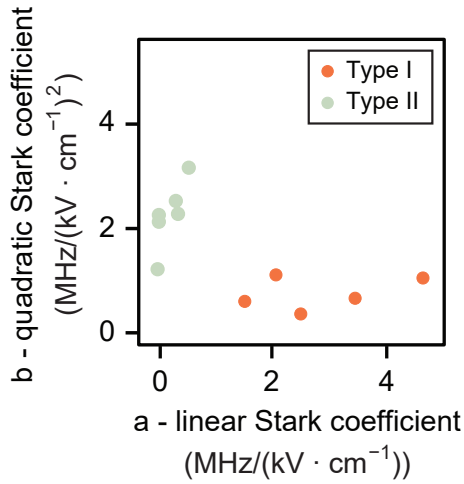

Figure 5.11: Distribution of the linear (a) and parabolic (b) Stark coefficients for 11 molecules. Type I molecules (orange) have very small quadratic Stark contribution ($\bar{b}_I = 0.7 \pm 0.3$ MHz/(kV $\cdot$ cm^{-1})^2), Type II molecules (green) have negligible linear Stark contribution ($\bar{a}_{II} = 0.2 \pm 0.2$ MHz/(kV $\cdot$ cm^{-1})).

in Figure 5.8 - normalized to 1 for simplicity - we can extract the linear (a) and parabolic (b) Stark coefficients for each molecule. Figure 5.11 shows the distribution of the two coefficients for 11 molecules. Type I molecules (in orange) display a very small b coefficient ($\bar{b}_I = 0.7 \pm 0.3$ MHz/(kV $\cdot$ cm^{-1})^2) and a broader distribution for the linear coefficient a ($\bar{a}_I = 2.9 \pm 1.1$ MHz/(kV $\cdot$ cm^{-1})). Type II molecules (in green) have a very small linear contribution a ($\bar{a}_{II} = 0.2 \pm 0.2$ MHz/(kV $\cdot$ cm^{-1})) while a dominant parabolic contribution represented by the quadratic coefficient b ($\bar{b}_{II} = 2.2 \pm 0.6$ MHz/(kV $\cdot$ cm^{-1})^2). These results show a clear correlation between Type I and II Stark effect and a mainly linear or parabolic contribution in the Stark equation.

5.5 Conclusions

In this chapter, we have shown the fabrication of an hybrid device combining a graphene field effect transistor with narrow linewidth quantum emitters. Thanks to the sensitivity of the emitters to external electric fields (Stark effect), we have exploited them as probes of the field generated by graphene. The emitters have displayed large Stark shift, similar to results previously reported in literature [126]. As the geometry of the

device allowed to study the behaviour of the electric field at different locations of the graphene device, we have observed a very different Stark response at the edge compared to the centre, with anomalous Stark effect saturating at positive and negative backgate voltages. We have presented an electrostatic model based on the idea of having a point defect charging at the edge of graphene, which reproduces very well the experimental data and the saturation regime. The model is developed in the steady state, for which fluctuations around equilibrium are averaged, but in reality the occupation of the defect state oscillates between 0 and 1 inducing a fluctuating electric field. A more advanced model might take into account these electric field fluctuations resulting in fluctuations of the molecules' emission signal, opening the way to the study of noise in graphene using quantum emitters as probes.

Single molecules as sensors of local electric fields in graphene

- We used single molecules as electric field sensors at the centre and edge of a graphene field effect transistor
- We observed exotic Stark effect at the edge of graphene due to local charge states saturating at positive and negative backgate voltages
- We developed an electrostatic model describing a defect point charging at the edge of the graphene device
- We identified the correlation between the Stark shift behaviour and the linear and quadratic contribution to the Stark shift equation

Chapter 6

Conclusion and outlook

In this thesis, we explored the near-field effects arising between a quantum emitter and a 2-dimensional material at the nanoscale. Interesting phenomena, often otherwise negligible, are offered by reducing the size of and the distance between photonic elements.
The novelty in our approach is in the choice of the two blocks building our hybrid device. On one hand, we work with nanoscopic quantum emitters characterized by well defined resonant energy and lifetime-limited emission with ultranarrow linewidth, making them good sensors of fields and charges. In addition to that, the solid state single-photon sources used in this work are stable, reproducible, scalable and convenient to integrate. On the other hand, we have 2-dimensional materials, which can be exfoliated, stacked and transferred onto a device. They provide tunable atomic-thin slabs with different electronic properties to explore near-field effects.

One technological issue we faced in this work is the integration of these two elements. With appropriate dry transfer techniques, we achieved interfacing single molecules into a capacitor configuration exploiting 2D materials as transparent and non-invasive electrodes. We also developed a lithographic technique to deterministic design 3D polymer-based photonic structures aligned on the emitters' position using electron beam lithography, for integration into waveguides and emission enhancement.
The capacitive hybrid device allowed the application of an electric field detected by the molecules with a field resolution of 3 $V \cdot cm^{-1}$ and a

maximum Stark shift of their emission energy up to 10^4 times the intrinsic linewidth. The 2D electrode could also be used to modulate the molecule's emission at high frequency (comparable to their linewidth $\sim$ 100 MHz) by applying an oscillating AC field.
A different scenario is offered when single molecules are deposited on top a graphene transistor. We used organic molecules as nanoscopic sensors of electric field at different locations of the device, revealing an exotic behavior at the edge of graphene explained by the charging and saturation of atomic-scale defects.

Future perspectives

Hybrid devices combining quantum emitters with 2D materials have shown their efficiency in terms of energy tuning and emission modulation.
Emission energy tunability is an appealing feature to complement integration of single-photon sources with other nanophotonic elements. Coupling quantum emitters to a specifically designed plasmonic (see Fig. 6.1a) or optical (see Fig. 6.1b) antenna allows to maximize the dipole interaction and enhance the emission [144], while 2D materials enable electrical tuning of the emission via Stark shift. This approach might be used to couple different single-photon sources through the same plasmonic antenna (as represented in the sketch of Figure 6.1a) or waveguide [145]. The energy tunability might as well be exploited to explore strong coupling regimes, by shifting the emitter's energy into resonance with excitons in 2D materials to reach an exciton-polariton coupling.

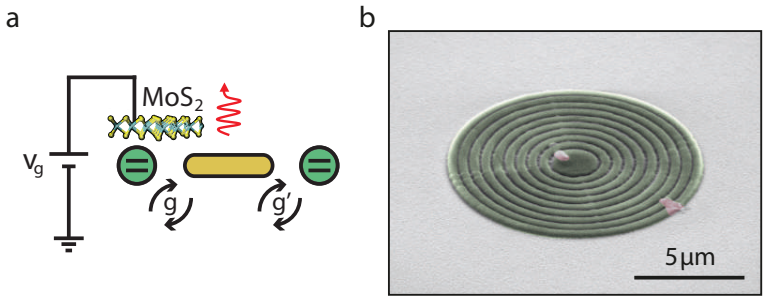

Figure 6.1: Coupling of single-photon sources to nanophotonic structures such as plasmonic (**a**) and optical (**b**) antennas.

We have also demonstrated the emission modulation of single-photon sources up to a frequency comparable to their linewidth. Pushing the control over their dynamics to much shorter time scale than the lifetime might allow to observe non-linear light-matter interactions at the quantum level [146].

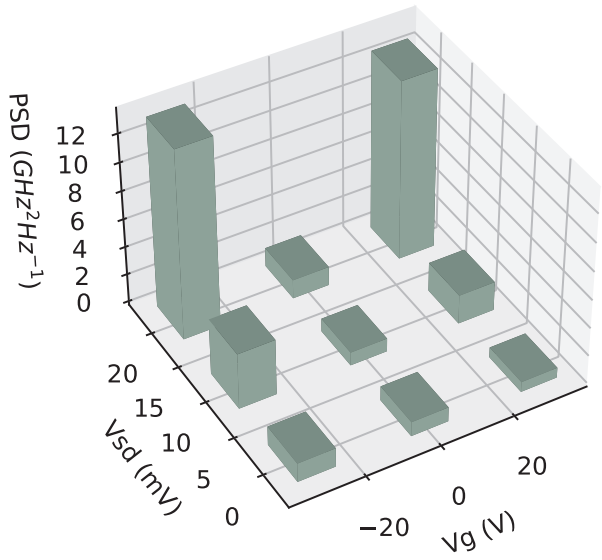

Figure 6.2: Preliminary results on white noise sensing measured in a graphene field effect transistor, showing an increase as function of the current running through the device.

Single-photon sources could also be used to study properties of their environment and of 2D materials in the near proximity. Detection of charge behaviour in graphene opens the way to noise sensing and non-invasive probing of localized charge carriers in 2D materials. In a graphene-based field effect transistor, like the one presented in Chapter 5, we can use quantum emitters as sensors of environmental perturbations. We collect DBT molecules' emission energy fluctuations in time while modifying the current running through the device from source to drain electrodes, at different backgate voltages. The Fourier transform of this signal contains information on the noise contribution as function of the frequency. We focus on the white noise behaviour with source-drain bias. Some preliminary results, presented in Figure 6.2, show a different sensitivity to source-drain currents at different backgate voltages applied to the device. At zero bias we don't observe increasing noise at high

positive or negative backgate, as expected from our previous work [126]. On the other hand, we observe a clear increasing trend with bias at high positive and negative backgate voltages, suggesting the kicking in of some noise mechanism.
Likewise, single organic molecules could be used to study the occupancy level of 0D and 1D quantum systems.

Bibliography

[1] Inside Quantum Technology. *Quantum computing market to reach US $ 1.9 billion by 2023, says new IQT report*. URL: https://www.insidequantumtechnology.com/news-release/quantum-computing-market-to-reach-us1-9-billion-by-2023-says-new-iqt-report/#:~:text=Quantum%20Computing%20Market%20To%20Reach,2023%2C%20Says%20New%20IQT%20Report. Accessed: 08.12.2020.

[2] Claudio U. Hail et al. "Nanoprinting organic molecules at the quantum level". In: *Nature Communications* 10.1 (2019), p. 1880. DOI: 10.1038/s41467-019-09877-5. URL: https://doi.org/10.1038/s41467-019-09877-5.

[3] Nicolas Sangouard and Hugo Zbinden. "What are single photons good for?" In: *Journal of Modern Optics* 59.17 (2012), pp. 1458–1464. DOI: 10.1080/09500340.2012.687500. eprint: https://doi.org/10.1080/09500340.2012.687500. URL: https://doi.org/10.1080/09500340.2012.687500.

[4] Igor Aharonovich, Dirk Englund, and Milos Toth. "Solid-state single-photon emitters". In: *Nature Photonics* 10.10 (2016), pp. 631–641. DOI: 10.1038/nphoton.2016.186. URL: https://doi.org/10.1038/nphoton.2016.186.

[5] Kevin G. Schädler. "Single quantum emitter manipulation with 2D materials." PhD thesis. UPC, Institut de Ciències Fotòniques, 2018. URL: http://hdl.handle.net/2117/119095.

[6] Alán Aspuru-Guzik and Philip Walther. "Photonic quantum simulators". In: *Nature Physics* 8.4 (2012), pp. 285–291. DOI: 10.1038/nphys2253. URL: https://doi.org/10.1038/nphys2253.

[7] Han-Sen Zhong et al. "Quantum computational advantage using photons". In: *Science* 370.6523 (2020), pp. 1460–1463. ISSN: 0036-8075. DOI: 10.1126/science.abe8770. eprint: https://science.sciencemag.org/content/370/6523/1460.pdf. URL: https://science.sciencemag.org/content/370/6523/1460.

[8] E. Knill, R. Laflamme, and G. J. Milburn. "A scheme for efficient quantum computation with linear optics". In: *Nature* 409.6816 (2001), pp. 46–52. DOI: 10.1038/35051009. URL: https://doi.org/10.1038/35051009.

[9] Pietro Lombardi et al. "A Molecule-Based Single-Photon Source Applied in Quantum Radiometry". In: *Advanced Quantum Technologies* 3.2 (2020), p. 1900083. DOI: https://doi.org/10.1002/qute.201900083. eprint: https://onlinelibrary.wiley.com/doi/pdf/10.1002/qute.201900083. URL: https://onlinelibrary.wiley.com/doi/abs/10.1002/qute.201900083.

[10] Klaus Mølmer and Anders Sørensen. "Multiparticle Entanglement of Hot Trapped Ions". In: *Phys. Rev. Lett.* 82 (9 1999), pp. 1835–1838. DOI: 10.1103/PhysRevLett.82.1835. URL: https://link.aps.org/doi/10.1103/PhysRevLett.82.1835.

[11] L. You. "Creating Maximally Entangled Atomic States in a Bose-Einstein Condensate". In: *Phys. Rev. Lett.* 90 (3 2003), p. 030402. DOI: 10.1103/PhysRevLett.90.030402. URL: https://link.aps.org/doi/10.1103/PhysRevLett.90.030402.

[12] C. Hettich et al. "Nanometer Resolution and Coherent Optical Dipole Coupling of Two Individual Molecules". In: *Science* 298.5592 (2002), pp. 385–389. ISSN: 0036-8075. DOI: 10.1126/science.1075606. eprint: https://science.sciencemag.org/content/298/5592/385.full.pdf. URL: https://science.sciencemag.org/content/298/5592/385.

[13] Yumin Shen, Timothy M. Sweeney, and Hailin Wang. "Zero-phonon linewidth of single nitrogen vacancy centers in diamond nanocrystals". In: *Phys. Rev. B* 77 (3 2008), p. 033201. DOI: 10.1103/PhysRevB.77.033201.

[14] N. Somaschi et al. "Near-optimal single-photon sources in the solid state". In: *Nature Photonics* 10.5 (2016), pp. 340–345. DOI: 10.1038/nphoton.2016.23.

[15] Alexander Högele et al. "Photon Antibunching in the Photoluminescence Spectra of a Single Carbon Nanotube". In: *Phys. Rev. Lett.* 100 (21 2008), p. 217401. DOI: 10.1103/PhysRevLett.100.217401.

[16] Sofia Pazzagli et al. "Self-Assembled Nanocrystals of Polycyclic Aromatic Hydrocarbons Show Photostable Single-Photon Emission". In: *ACS Nano* 12.5 (2018). PMID: 29630340, pp. 4295–4303. DOI: 10.1021/acsnano.7b08810.

[17] Carmen Palacios-Berraquero et al. "Large-scale quantum-emitter arrays in atomically thin semiconductors". In: *Nature Communications* 8.1 (2017), p. 15093. DOI: 10.1038/ncomms15093.

[18] Aurélien A L Nicolet et al. "Single dibenzoterrylene molecules in an anthracene crystal: main insertion sites." eng. In: *Chemphyschem* 8.13 (2007), pp. 1929–1936. ISSN: 1439-4235 (Print); 1439-4235 (Linking). DOI: 10.1002/cphc.200700340.

[19] Amin Moradi et al. "Matrix-induced Linear Stark Effect of Single Dibenzoterrylene Molecules in 2,3-Dibromonaphthalene Crystal". In: *ChemPhysChem* 20.1 (2019), pp. 55–61. DOI: https://doi.org/10.1002/cphc.201800937. eprint: https://chemistry-europe.onlinelibrary.wiley.com/doi/pdf/10.1002/cphc.201800937. URL: https://chemistry-europe.onlinelibrary.wiley.com/doi/abs/10.1002/cphc.201800937.

[20] Jean-Michel Caruge and Michel Orrit. "Probing local currents in semiconductors with single molecules". In: *Phys. Rev. B* 64 (20 2001), p. 205202. DOI: 10.1103/PhysRevB.64.205202. URL: https://link.aps.org/doi/10.1103/PhysRevB.64.205202.

[21] Maja Colautti et al. "Laser-Induced Frequency Tuning of Fourier-Limited Single-Molecule Emitters". In: *ACS Nano* 14.10 (2020). PMID: 32936612, pp. 13584–13592. DOI: 10.1021/acsnano.0c05620. eprint: https://doi.org/10.1021/acsnano.0c05620. URL: https://doi.org/10.1021/acsnano.0c05620.

[22] Pierre Türschmann et al. "Chip-Based All-Optical Control of Single Molecules Coherently Coupled to a Nanoguide". In: *Nano Letters* 17.8 (2017). PMID: 28671833, pp. 4941–4945. DOI: 10.1021/acs.nanolett.7b02033. eprint: https://doi.org/10.1021/acs.nanolett.7b02033. URL: https://doi.org/10.1021/acs.nanolett.7b02033.

[23] P. Lombardi et al. “Photostable Molecules on Chip: Integrated Sources of Nonclassical Light”. In: *ACS Photonics* 5.1 (2018), pp. 126–132. DOI: 10.1021/acsphotonics.7b00521. eprint: https://doi.org/10.1021/acsphotonics.7b00521. URL: https://doi.org/10.1021/acsphotonics.7b00521.

[24] S. Grandi et al. “Hybrid plasmonic waveguide coupling of photons from a single molecule”. In: *APL Photonics* 4.8 (2019), p. 086101. DOI: 10.1063/1.5110275. eprint: https://doi.org/10.1063/1.5110275. URL: https://doi.org/10.1063/1.5110275.

[25] Maja Colautti et al. “A 3D Polymeric Platform for Photonic Quantum Technologies”. In: *Advanced Quantum Technologies* 3.7 (2020), p. 2000004. DOI: https://doi.org/10.1002/qute.202000004. eprint: https://onlinelibrary.wiley.com/doi/pdf/10.1002/qute.202000004. URL: https://onlinelibrary.wiley.com/doi/abs/10.1002/qute.202000004.

[26] Sebastien Boissier et al. “Coherent characterisation of a single molecule in a photonic black box”. In: *Nature Communications* 12.1 (2021), p. 706. DOI: 10.1038/s41467-021-20915-z. URL: https://doi.org/10.1038/s41467-021-20915-z.

[27] C. Toninelli et al. “Single organic molecules for photonic quantum technologies”. In: *Nature Materials* (2021). DOI: 10.1038/s41563-021-00987-4. URL: https://doi.org/10.1038/s41563-021-00987-4.

[28] K. S. Novoselov et al. “Electric Field Effect in Atomically Thin Carbon Films”. In: *Science* 306.5696 (2004), pp. 666–669. ISSN: 0036-8075. DOI: 10.1126/science.1102896. eprint: https://science.sciencemag.org/content/306/5696/666.full.pdf. URL: https://science.sciencemag.org/content/306/5696/666.

[29] K. S. Novoselov et al. “Two-dimensional atomic crystals”. In: *Proceedings of the National Academy of Sciences* 102.30 (2005), pp. 10451–10453. ISSN: 0027-8424. DOI: 10.1073/pnas.0502848102. eprint: https://www.pnas.org/content/102/30/10451.full.pdf. URL: https://www.pnas.org/content/102/30/10451.

[30] Kin Fai Mak and Jie Shan. “Photonics and optoelectronics of 2D semiconductor transition metal dichalcogenides”. In: *Nature Photonics* 10.4 (2016), pp. 216–226. DOI: 10.1038/nphoton.2015.282.

[31] C. R. Dean et al. "Boron nitride substrates for high-quality graphene electronics". In: *Nature Nanotechnology* 5.10 (2010), pp. 722–726. DOI: 10.1038/nnano.2010.172. URL: https://doi.org/10.1038/nnano.2010.172.

[32] R. F. Frindt. "Superconductivity in Ultrathin $NbSe_2$ Layers". In: *Phys. Rev. Lett.* 28 (5 1972), pp. 299–301. DOI: 10.1103/PhysRevLett.28.299.

[33] K S Novoselov et al. "2D materials and van der Waals heterostructures." eng. In: *Science* 353.6298 (2016), aac9439. ISSN: 1095-9203 (Electronic); 0036-8075 (Linking). DOI: 10.1126/science.aac9439.

[34] Yuan Cao et al. "Unconventional superconductivity in magic-angle graphene superlattices". In: *Nature* 556.7699 (2018), pp. 43–50. DOI: 10.1038/nature26160.

[35] Zheyuan Chen et al. "Energy Transfer from Individual Semiconductor Nanocrystals to Graphene". In: *ACS Nano* 4.5 (2010). PMID: 20402475, pp. 2964–2968. DOI: 10.1021/nn1005107. eprint: https://doi.org/10.1021/nn1005107. URL: https://doi.org/10.1021/nn1005107.

[36] L. Gaudreau et al. "Universal Distance-Scaling of Nonradiative Energy Transfer to Graphene". In: *Nano Letters* 13.5 (2013). PMID: 23488979, pp. 2030–2035. DOI: 10.1021/nl400176b. eprint: https://doi.org/10.1021/nl400176b. URL: https://doi.org/10.1021/nl400176b.

[37] Dhiraj Prasai et al. "Electrical Control of near-Field Energy Transfer between Quantum Dots and Two-Dimensional Semiconductors". In: *Nano Letters* 15.7 (2015). PMID: 26027714, pp. 4374–4380. DOI: 10.1021/acs.nanolett.5b00514. eprint: https://doi.org/10.1021/acs.nanolett.5b00514. URL: https://doi.org/10.1021/acs.nanolett.5b00514.

[38] Chitraleema Chakraborty et al. "Quantum-Confined Stark Effect of Individual Defects in a van der Waals Heterostructure". In: *Nano Letters* 17.4 (2017). PMID: 28267348, pp. 2253–2258. DOI: 10.1021/acs.nanolett.6b04889. eprint: https://doi.org/10.1021/acs.nanolett.6b04889. URL: https://doi.org/10.1021/acs.nanolett.6b04889.

[39] Mark Fox. *Quantum optics: an introduction*. Oxford master series in atomic, optical, and laser physics. Oxford: Oxford Univ. Press, 2006. URL: https://cds.cern.ch/record/1001868.

[40] Edward Mills Purcell. "Spontaneous Emission Probabilities at Radio Frequencies". In: *Physical Review* 69.5994 (1946), pp. 839–839.

[41] Susumu Noda, Masayuki Fujita, and Takashi Asano. "Spontaneous-emission control by photonic crystals and nanocavities". In: *Nature Photonics* 1.8 (2007), pp. 449–458. DOI: 10.1038/nphoton.2007.141. URL: https://doi.org/10.1038/nphoton.2007.141.

[42] Alberto G. Curto et al. "Unidirectional Emission of a Quantum Dot Coupled to a Nanoantenna". In: *Science* 329.5994 (2010), pp. 930–933. ISSN: 0036-8075. DOI: 10.1126/science.1191922. eprint: https://science.sciencemag.org/content/329/5994/930.full.pdf. URL: https://science.sciencemag.org/content/329/5994/930.

[43] François Federspiel et al. "Distance Dependence of the Energy Transfer Rate from a Single Semiconductor Nanostructure to Graphene". In: *Nano Letters* 15.2 (2015). PMID: 25607231, pp. 1252–1258. DOI: 10.1021/nl5044192.

[44] K. J. Tielrooij et al. "Electrical control of optical emitter relaxation pathways enabled by graphene". In: *Nature Physics* 11.3 (2015), pp. 281–287. DOI: 10.1038/nphys3204. URL: https://doi.org/10.1038/nphys3204.

[45] Antoine Reserbat-Plantey et al. "Electromechanical control of nitrogen-vacancy defect emission using graphene NEMS". In: *Nature Communications* 7.1 (2016), p. 10218. DOI: 10.1038/ncomms10218. URL: https://doi.org/10.1038/ncomms10218.

[46] Etienne Lorchat et al. "Filtering the photoluminescence spectra of atomically thin semiconductors with graphene". In: *Nature Nanotechnology* 15.4 (2020), pp. 283–288. DOI: 10.1038/s41565-020-0644-2. URL: https://doi.org/10.1038/s41565-020-0644-2.

[47] H.B.G. Casimir. In: *Proc. K. Ned. Akad. Wet.* 51 (1948), pp. 793–795.

[48] H. B. G. Casimir and D. Polder. "The Influence of Retardation on the London-van der Waals Forces". In: *Phys. Rev.* 73 (4 1948), pp. 360–372. DOI: 10.1103/PhysRev.73.360. URL: https://link.aps.org/doi/10.1103/PhysRev.73.360.

[49] C. I. Sukenik et al. "Measurement of the Casimir-Polder force". In: *Phys. Rev. Lett.* 70 (5 1993), pp. 560–563. DOI: 10.1103/PhysRevLett.70.560. URL: https://link.aps.org/doi/10.1103/PhysRevLett.70.560.

[50] Christine A. Muschik et al. "Harnessing Vacuum Forces for Quantum Sensing of Graphene Motion". In: *Phys. Rev. Lett.* 112 (22 2014), p. 223601. DOI: 10.1103/PhysRevLett.112.223601. URL: https://link.aps.org/doi/10.1103/PhysRevLett.112.223601.

[51] J. Stuart Foster. "Some leading features of the stark effect". In: *Journal of the Franklin Institute* 209.5 (1930), pp. 585–624. ISSN: 0016-0032. DOI: https://doi.org/10.1016/S0016-0032(30)90851-4. URL: https://www.sciencedirect.com/science/article/pii/S0016003230908514.

[52] M. Orrit et al. "Stark effect on single molecules in a polymer matrix". In: *Chemical Physics Letters* 196.6 (1992), pp. 595–600. ISSN: 0009-2614. DOI: https://doi.org/10.1016/0009-2614(92)86000-8. URL: https://www.sciencedirect.com/science/article/pii/0009261492860008.

[53] Ch. Brunel et al. "Stark Effect on Single Molecules of Dibenzanthanthrene in a Naphthalene Crystal and in a n-Hexadecane Shpol'skii Matrix". In: *The Journal of Physical Chemistry A* 103.14 (1999), pp. 2429–2434. DOI: 10.1021/jp983956t. eprint: https://doi.org/10.1021/jp983956t. URL: https://doi.org/10.1021/jp983956t.

[54] Artur Branny et al. "Deterministic strain-induced arrays of quantum emitters in a two-dimensional semiconductor". In: *Nature Communications* 8.1 (2017), p. 15053. DOI: 10.1038/ncomms15053. URL: https://doi.org/10.1038/ncomms15053.

[55] K. Barthelmi et al. "Atomistic defects as single-photon emitters in atomically thin MoS2". In: *Applied Physics Letters* 117.7 (2020), p. 070501. DOI: 10.1063/5.0018557. eprint: https://doi.org/10.1063/5.0018557. URL: https://doi.org/10.1063/5.0018557.

[56] Matthew R. Rosenberger et al. "Quantum Calligraphy: Writing Single-Photon Emitters in a Two-Dimensional Materials Platform". In: *ACS Nano* 13.1 (2019), pp. 904–912. DOI: 10.1021/acsnano.8b08730. eprint: https://doi.org/10.1021/acsnano.8b08730. URL: https://doi.org/10.1021/acsnano.8b08730.

[57] Carmen Palacios-Berraquero et al. "Atomically thin quantum light-emitting diodes". In: *Nature Communications* 7.1 (2016), p. 12978. DOI: 10.1038/ncomms12978.

[58] Jeremy L. O'Brien, Akira Furusawa, and Jelena Vučković. "Photonic quantum technologies". In: *Nature Photonics* 3.12 (2009), pp. 687–695. DOI: 10.1038/nphoton.2009.229. URL: https://doi.org/10.1038/nphoton.2009.229.

[59] Pieter Kok et al. "Linear optical quantum computing with photonic qubits". In: *Rev. Mod. Phys.* 79 (1 2007), pp. 135–174. DOI: 10.1103/RevModPhys.79.135. URL: https://link.aps.org/doi/10.1103/RevModPhys.79.135.

[60] Valerio Scarani et al. "The security of practical quantum key distribution". In: *Rev. Mod. Phys.* 81 (3 2009), pp. 1301–1350. DOI: 10.1103/RevModPhys.81.1301. URL: https://link.aps.org/doi/10.1103/RevModPhys.81.1301.

[61] Vittorio Giovannetti, Seth Lloyd, and Lorenzo Maccone. "Advances in quantum metrology". In: *Nature Photonics* 5.4 (2011), pp. 222–229. DOI: 10.1038/nphoton.2011.35. URL: https://doi.org/10.1038/nphoton.2011.35.

[62] J.-B. Trebbia et al. "Efficient generation of near infra-red single photons from the zero-phonon line of a single molecule". In: *Opt. Express* 17.26 (2009), pp. 23986–23991. DOI: 10.1364/OE.17.023986. URL: http://www.opticsexpress.org/abstract.cfm?URI=oe-17-26-23986.

[63] Jean-Baptiste Trebbia, Philippe Tamarat, and Brahim Lounis. "Indistinguishable near-infrared single photons from an individual organic molecule". In: *Phys. Rev. A* 82 (6 2010), p. 063803. DOI: 10.1103/PhysRevA.82.063803. URL: https://link.aps.org/doi/10.1103/PhysRevA.82.063803.

[64] Daqing Wang et al. "Coherent Coupling of a Single Molecule to a Scanning Fabry-Perot Microcavity". In: *Phys. Rev. X* 7 (2 2017), p. 021014. DOI: 10.1103/PhysRevX.7.021014. URL: https://link.aps.org/doi/10.1103/PhysRevX.7.021014.

[65] Chloe Clear et al. "Phonon-Induced Optical Dephasing in Single Organic Molecules". In: *Phys. Rev. Lett.* 124 (15 2020), p. 153602. DOI: 10.1103/PhysRevLett.124.153602. URL: https://link.aps.org/doi/10.1103/PhysRevLett.124.153602.

[66] W. E. Moerner and L. Kador. "Optical detection and spectroscopy of single molecules in a solid". In: *Phys. Rev. Lett.* 62 (21 1989), pp. 2535–2538. DOI: 10.1103/PhysRevLett.62.2535. URL: https://link.aps.org/doi/10.1103/PhysRevLett.62.2535.

[67] M. Orrit and J. Bernard. "Single pentacene molecules detected by fluorescence excitation in a p-terphenyl crystal". In: *Phys. Rev. Lett.* 65 (21 1990), pp. 2716–2719. DOI: 10.1103/PhysRevLett.65.2716. URL: https://link.aps.org/doi/10.1103/PhysRevLett.65.2716.

[68] C. Toninelli et al. "Near-infrared single-photons from aligned molecules in ultrathin crystalline films at room temperature". In: *Opt. Express* 18.7 (2010), pp. 6577–6582. DOI: 10.1364/OE.18.006577. URL: http://www.opticsexpress.org/abstract.cfm?URI=oe-18-7-6577.

[69] Claudio Polisseni et al. "Stable, single-photon emitter in a thin organic crystal for application to quantum-photonic devices". In: *Opt. Express* 24.5 (2016), pp. 5615–5627. DOI: 10.1364/OE.24.005615. URL: http://www.opticsexpress.org/abstract.cfm?URI=oe-24-5-5615.

[70] Sofia Pazzagli. "Organic nanocrystals and polymeric waveguides: a novel path towards integrated quantum nanophotonics". PhD thesis. Università degli Studi di Firenze, 2018.

[71] Samuele Grandi et al. "Quantum dynamics of a driven two-level molecule with variable dephasing". In: *Phys. Rev. A* 94 (6 2016), p. 063839. DOI: 10.1103/PhysRevA.94.063839. URL: https://link.aps.org/doi/10.1103/PhysRevA.94.063839.

[72] F. Jelezko, B. Lounis, and M. Orrit. "Pump–probe spectroscopy and photophysical properties of single di-benzanthanthrene molecules in a naphthalene crystal". In: *The Journal of Chemical Physics* 107.6 (1997), pp. 1692–1702. DOI: 10.1063/1.474525. eprint: https://doi.org/10.1063/1.474525. URL: https://doi.org/10.1063/1.474525.

[73] W. E. Moerner and David P. Fromm. "Methods of single-molecule fluorescence spectroscopy and microscopy". In: *Review of Scientific Instruments* 74.8 (2003), pp. 3597–3619. DOI: 10.1063/1.1589587. URL: https://doi.org/10.1063/1.1589587.

[74] T. Basché et al. *Single-Molecule Optical Detection, Imaging and Spectroscopy*. Wiley, 2008. ISBN: 9783527614707.

[75] R. Hanbury Brown and R. Q. Twiss. "A Test of a New Type of Stellar Interferometer on Sirius". In: *Nature* 178.4541 (1956), pp. 1046–1048. DOI: 10.1038/1781046a0. URL: https://doi.org/10.1038/1781046a0.

[76] L. Fleury et al. "Nonclassical Photon Statistics in Single-Molecule Fluorescence at Room Temperature". In: *Phys. Rev. Lett.* 84 (6 2000), pp. 1148–1151. DOI: 10.1103/PhysRevLett.84.1148. URL: https://link.aps.org/doi/10.1103/PhysRevLett.84.1148.

[77] H. J. Kimble, M. Dagenais, and L. Mandel. "Photon Antibunching in Resonance Fluorescence". In: *Phys. Rev. Lett.* 39 (11 1977), pp. 691–695. DOI: 10.1103/PhysRevLett.39.691. URL: https://link.aps.org/doi/10.1103/PhysRevLett.39.691.

[78] Ingemar Johansson Cox, CJR Sheppard, and T Wilson. "Super-resolution by confocal fluorescent microscopy". Udefineret/Ukendt. In: *Optik (Online)* 60.4 (1982), pp. 391–396. ISSN: 1653-3666.

[79] R. Webb. "Confocal optical microscopy". In: *Reports on Progress in Physics* 59 (1996), pp. 427–471.

[80] Ilja Gerhardt et al. "Detection of Single Molecules Illuminated by a Light-Emitting Diode". In: *Sensors* 11.1 (2011), pp. 905–916. ISSN: 1424-8220. DOI: 10.3390/s110100905. URL: https://www.mdpi.com/1424-8220/11/1/905.

[81] C. Raynaud et al. “Superlocalization of Excitons in Carbon Nanotubes at Cryogenic Temperature”. In: *Nano Letters* 19.10 (2019). PMID: 31487461, pp. 7210–7216. DOI: 10.1021/acs.nanolett.9b02816. eprint: https://doi.org/10.1021/acs.nanolett.9b02816. URL: https://doi.org/10.1021/acs.nanolett.9b02816.

[82] P.-L. de Assis et al. “Strain-Gradient Position Mapping of Semiconductor Quantum Dots”. In: *Phys. Rev. Lett.* 118 (11 2017), p. 117401. DOI: 10.1103/PhysRevLett.118.117401. URL: https://link.aps.org/doi/10.1103/PhysRevLett.118.117401.

[83] Min Gu et al. “Super-resolving single nitrogen vacancy centers within single nanodiamonds using a localization microscope”. In: *Opt. Express* 21.15 (2013), pp. 17639–17646. DOI: 10.1364/OE.21.017639. URL: http://www.opticsexpress.org/abstract.cfm?URI=oe-21-15-17639.

[84] E. Betzig. “Proposed method for molecular optical imaging”. In: *Opt. Lett.* 20.3 (1995), pp. 237–239. DOI: 10.1364/OL.20.000237. URL: http://ol.osa.org/abstract.cfm?URI=ol-20-3-237.

[85] W. E. Moerner and Michel Orrit. “Illuminating Single Molecules in Condensed Matter”. In: *Science* 283.5408 (1999), pp. 1670–1676. ISSN: 0036-8075. DOI: 10.1126/science.283.5408.1670. eprint: https://science.sciencemag.org/content/283/5408/1670.full.pdf. URL: https://science.sciencemag.org/content/283/5408/1670.

[86] O. Gazzano et al. “Bright solid-state sources of indistinguishable single photons”. In: *Nature Communications* 4.1 (2013), p. 1425. DOI: 10.1038/ncomms2434. URL: https://doi.org/10.1038/ncomms2434.

[87] Luca Sapienza et al. “Nanoscale optical positioning of single quantum dots for bright and pure single-photon emission”. In: *Nature Communications* 6.1 (2015), p. 7833. DOI: 10.1038/ncomms8833. URL: https://doi.org/10.1038/ncomms8833.

[88] Marcelo Davanco et al. “Heterogeneous integration for on-chip quantum photonic circuits with single quantum dot devices”. In: *Nature Communications* 8.1 (2017), p. 889. DOI: 10.1038/s41467-017-00987-6. URL: https://doi.org/10.1038/s41467-017-00987-6.

[89] Ph. Tamarat et al. "Stark Shift Control of Single Optical Centers in Diamond". In: *Phys. Rev. Lett.* 97 (8 2006), p. 083002. DOI: 10.1103/PhysRevLett.97.083002. URL: https://link.aps.org/doi/10.1103/PhysRevLett.97.083002.

[90] I. Yeo et al. "Strain-mediated coupling in a quantum dot–mechanical oscillator hybrid system". In: *Nature Nanotechnology* 9.2 (2014), pp. 106–110. DOI: 10.1038/nnano.2013.274. URL: https://doi.org/10.1038/nnano.2013.274.

[91] B. Lounis and W. E. Moerner. "Single photons on demand from a single molecule at room temperature". In: *Nature* 407.6803 (2000), pp. 491–493. DOI: 10.1038/35035032. URL: https://doi.org/10.1038/35035032.

[92] Clemens Hofmann et al. "Towards nanoprobes for conduction in molecular crystals: Dibenzoterrylene in anthracene crystals". In: *Chemical Physics* 318.1 (2005). Molecular Nanoscience, pp. 1–6. ISSN: 0301-0104. DOI: https://doi.org/10.1016/j.chemphys.2005.02.003. URL: https://www.sciencedirect.com/science/article/pii/S0301010405000674.

[93] Kyle D. Major et al. "Growth of optical-quality anthracene crystals doped with dibenzoterrylene for controlled single photon production". In: *Review of Scientific Instruments* 86.8 (2015), p. 083106. DOI: 10.1063/1.4928500. eprint: https://doi.org/10.1063/1.4928500. URL: https://doi.org/10.1063/1.4928500.

[94] Hae-Ryong Chung et al. "Effect of solvent on organic nanocrystal growth using the reprecipitation method". In: *Journal of Crystal Growth* 294.2 (2006), pp. 459–463. DOI: https://doi.org/10.1016/j.jcrysgro.2006.07.010. URL: https://www.sciencedirect.com/science/article/pii/S0022024806006889.

[95] Amy C. Sullivan, Matthew W. Grabowski, and Robert R. McLeod. "Three-dimensional direct-write lithography into photopolymer". In: *Appl. Opt.* 46.3 (2007), pp. 295–301. DOI: 10.1364/AO.46.000295. URL: http://ao.osa.org/abstract.cfm?URI=ao-46-3-295.

[96] Andreas W. Schell et al. "Three-dimensional quantum photonic elements based on single nitrogen vacancy-centres in laser-written microstructures". In: *Scientific Reports* 3.1 (2013), p. 1577. DOI: 10.1038/srep01577. URL: https://doi.org/10.1038/srep01577.

[97] A. Sipahigil et al. "An integrated diamond nanophotonics platform for quantum-optical networks". In: *Science* 354.6314 (2016), pp. 847–850. ISSN: 0036-8075. DOI: 10.1126/science.aah6875. eprint: https://science.sciencemag.org/content/354/6314/847.full.pdf. URL: https://science.sciencemag.org/content/354/6314/847.

[98] M. Gschrey et al. "Highly indistinguishable photons from deterministic quantum-dot microlenses utilizing three-dimensional in situ electron-beam lithography". In: *Nature Communications* 6.1 (2015), p. 7662. DOI: 10.1038/ncomms8662. URL: https://doi.org/10.1038/ncomms8662.

[99] R Abargues et al. "High-resolution electron-beam patternable nanocomposite containing metal nanoparticles for plasmonics". In: *Nanotechnology* 19.35 (2008), p. 355308. DOI: 10.1088/0957-4484/19/35/355308. URL: https://doi.org/10.1088/0957-4484/19/35/355308.

[100] José Marqués-Hueso et al. "Au-PVA Nanocomposite Negative Resist for One-Step Three-Dimensional e-Beam Lithography". In: *Langmuir* 26.4 (Feb. 2010), pp. 2825–2830. DOI: 10.1021/la902915n. URL: https://doi.org/10.1021/la902915n.

[101] James C. Bray and Edward W. Merrill. "Poly(vinyl alcohol) hydrogels. Formation by electron beam irradiation of aqueous solutions and subsequent crystallization". In: *Journal of Applied Polymer Science* 17.12 (1973), pp. 3779–3794. DOI: https://doi.org/10.1002/app.1973.070171219. eprint: https://onlinelibrary.wiley.com/doi/pdf/10.1002/app.1973.070171219. URL: https://onlinelibrary.wiley.com/doi/abs/10.1002/app.1973.070171219.

[102] G Mazzamuto et al. "Single-molecule study for a graphene-based nano-position sensor". In: *New Journal of Physics* 16.11 (2014), p. 113007. DOI: 10.1088/1367-2630/16/11/113007. URL: https://doi.org/10.1088/1367-2630/16/11/113007.

[103] Toma Susi et al. "Atomistic Description of Electron Beam Damage in Nitrogen-Doped Graphene and Single-Walled Carbon Nanotubes". In: *ACS Nano* 6.10 (2012). PMID: 23009666, pp. 8837–8846. DOI: 10.1021/nn303944f. eprint: https://doi.org/10.1021/nn303944f. URL: https://doi.org/10.1021/nn303944f.

[104] R.F. Egerton, P. Li, and M. Malac. "Radiation damage in the TEM and SEM". In: *Micron* 35.6 (2004). International Wuhan Symposium on Advanced Electron Microscopy, pp. 399–409. ISSN: 0968-4328. DOI: https://doi.org/10.1016/j.micron.2004.02.003. URL: https://www.sciencedirect.com/science/article/pii/S0968432804000381.

[105] Florian Banhart. "Irradiation effects in carbon nanostructures". In: *Reports on Progress in Physics* 62.8 (1999), pp. 1181–1221. DOI: 10.1088/0034-4885/62/8/201. URL: https://doi.org/10.1088/0034-4885/62/8/201.

[106] B. Gross. "Radiation-induced charge storage and polarization effects". In: *Electrets*. Ed. by Gerhard M. Sessler. Berlin, Heidelber: Springer Berlin Heidelberg, 1987, pp. 217–284. ISBN: 978-3-540-70750-9. DOI: 10.1007/3540173358_12. URL: https://doi.org/10.1007/3540173358_12.

[107] John H. L. Watson. "An Effect of Electron Bombardment upon Carbon Black". In: *Journal of Applied Physics* 18.2 (1947), pp. 153–161. DOI: 10.1063/1.1697597. eprint: https://doi.org/10.1063/1.1697597. URL: https://doi.org/10.1063/1.1697597.

[108] Camilla Dore, Johann Osmond, and Agustín Mihi. "A water-processable cellulose-based resist for advanced nanofabrication". In: *Nanoscale* 10 (37 2018), pp. 17884–17892. DOI: 10.1039/C8NR04851G. URL: http://dx.doi.org/10.1039/C8NR04851G.

[109] Sanli Faez et al. "Coherent Interaction of Light and Single Molecules in a Dielectric Nanoguide". In: *Phys. Rev. Lett.* 113 (21 2014), p. 213601. DOI: 10.1103/PhysRevLett.113.213601. URL: https://link.aps.org/doi/10.1103/PhysRevLett.113.213601.

[110] Luozhou Li et al. "Efficient Photon Collection from a Nitrogen Vacancy Center in a Circular Bullseye Grating". In: *Nano Letters* 15.3 (2015). PMID: 25714414, pp. 1493–1497. DOI: 10.1021/nl503451j. eprint: https://doi.org/10.1021/nl503451j. URL: https://doi.org/10.1021/nl503451j.

[111] André Espinha et al. "Hydroxypropyl cellulose photonic architectures by soft nanoimprinting lithography". In: *Nature Photonics* 12.6 (2018), pp. 343–348. DOI: 10.1038/s41566-018-0152-1. URL: https://doi.org/10.1038/s41566-018-0152-1.

[112] Camilla Dore et al. "Hydroxypropyl Cellulose Adhesives for Transfer Printing of Carbon Nanotubes and Metallic Nanostructures". In: *Small* 16.47 (2020), p. 2004795. DOI: https://doi.org/10.1002/smll.202004795. eprint: https://onlinelibrary.wiley.com/doi/pdf/10.1002/smll.202004795. URL: https://onlinelibrary.wiley.com/doi/abs/10.1002/smll.202004795.

[113] Andrea Splendiani et al. "Emerging Photoluminescence in Monolayer MoS2". In: *Nano Letters* 10.4 (2010). PMID: 20229981, pp. 1271–1275. DOI: 10.1021/nl903868w. eprint: https://doi.org/10.1021/nl903868w. URL: https://doi.org/10.1021/nl903868w.

[114] K. S. Novoselov et al. "A roadmap for graphene". In: *Nature* 490.7419 (2012), pp. 192–200. DOI: 10.1038/nature11458. URL: https://doi.org/10.1038/nature11458.

[115] M. Massicotte et al. "Picosecond photoresponse in van der Waals heterostructures". In: *Nature Nanotechnology* 11.1 (2016), pp. 42–46. DOI: 10.1038/nnano.2015.227. URL: https://doi.org/10.1038/nnano.2015.227.

[116] Andres Castellanos-Gomez et al. "Deterministic transfer of two-dimensional materials by all-dry viscoelastic stamping". In: *2D Materials* 1.1 (2014), p. 011002. DOI: 10.1088/2053-1583/1/1/011002. URL: https://doi.org/10.1088/2053-1583/1/1/011002.

[117] Alexander S. Mayorov et al. "Micrometer-Scale Ballistic Transport in Encapsulated Graphene at Room Temperature". In: *Nano Letters* 11.6 (2011). PMID: 21574627, pp. 2396–2399. DOI: 10.1021/nl200758b. eprint: https://doi.org/10.1021/nl200758b. URL: https://doi.org/10.1021/nl200758b.

[118] P. Obreja et al. "Poly (vinyl-alcohol) films for microphotonics". In: *Proceedings. The 16th International Conference on Microelectronics, 2004. ICM 2004.* 2004, pp. 676–679. DOI: 10.1109/ICM.2004.1434756.

[119] Sergei Kühn et al. "Enhancement of Single-Molecule Fluorescence Using a Gold Nanoparticle as an Optical Nanoantenna". In: *Phys. Rev. Lett.* 97 (1 2006), p. 017402. DOI: 10.1103/PhysRevLett.97.017402. URL: https://link.aps.org/doi/10.1103/PhysRevLett.97.017402.

[120] Anika Kinkhabwala et al. “Large single-molecule fluorescence enhancements produced by a bowtie nanoantenna”. In: *Nature Photonics* 3.11 (2009), pp. 654–657. DOI: 10.1038/nphoton.2009.187. URL: https://doi.org/10.1038/nphoton.2009.187.

[121] Vadim Puller, Brahim Lounis, and Fabio Pistolesi. “Single Molecule Detection of Nanomechanical Motion”. In: *Phys. Rev. Lett.* 110 (12 2013), p. 125501. DOI: 10.1103/PhysRevLett.110.125501. URL: https://link.aps.org/doi/10.1103/PhysRevLett.110.125501.

[122] Oliver Benson. “Assembly of hybrid photonic architectures from nanophotonic constituents”. In: *Nature* 480.7376 (2011), pp. 193–199. DOI: 10.1038/nature10610. URL: https://doi.org/10.1038/nature10610.

[123] Frank H. L. Koppens, Darrick E. Chang, and F. Javier García de Abajo. “Graphene Plasmonics: A Platform for Strong Light–Matter Interactions”. In: *Nano Letters* 11.8 (2011). PMID: 21766812, pp. 3370–3377. DOI: 10.1021/nl201771h. eprint: https://doi.org/10.1021/nl201771h. URL: https://doi.org/10.1021/nl201771h.

[124] Vasilios D. Karanikolas et al. “Near-field relaxation of a quantum emitter to two-dimensional semiconductors: Surface dissipation and exciton polaritons”. In: *Phys. Rev. B* 94 (19 2016), p. 195418. DOI: 10.1103/PhysRevB.94.195418. URL: https://link.aps.org/doi/10.1103/PhysRevB.94.195418.

[125] Archana Raja et al. “Energy Transfer from Quantum Dots to Graphene and MoS2: The Role of Absorption and Screening in Two-Dimensional Materials”. In: *Nano Letters* 16.4 (2016). PMID: 26928675, pp. 2328–2333. DOI: 10.1021/acs.nanolett.5b05012. eprint: https://doi.org/10.1021/acs.nanolett.5b05012. URL: https://doi.org/10.1021/acs.nanolett.5b05012.

[126] Kevin G. Schädler et al. “Electrical Control of Lifetime-Limited Quantum Emitters Using 2D Materials”. In: *Nano Letters* 19.6 (2019). PMID: 31074994, pp. 3789–3795. DOI: 10.1021/acs.nanolett.9b00916. URL: https://doi.org/10.1021/acs.nanolett.9b00916.

[127] Rinu Abraham Maniyara et al. "An antireflection transparent conductor with ultralow optical loss (<2 %) and electrical resistance (<6 Ωsq-1)". In: *Nature Communications* 7.1 (2016), p. 13771. DOI: 10.1038/ncomms13771. URL: https://doi.org/10.1038/ncomms13771.

[128] Benjamin Gmeiner et al. "Spectroscopy and microscopy of single molecules in nanoscopic channels: spectral behavior vs. confinement depth". In: *Phys. Chem. Chem. Phys.* 18 (29 2016), pp. 19588–19594. DOI: 10.1039/C6CP01698G. URL: http://dx.doi.org/10.1039/C6CP01698G.

[129] P G Cummins and D A Dunmur. "The electric permittivity of crystalline anthracene". In: *Journal of Physics D: Applied Physics* 7.3 (1974), pp. 451–454. DOI: 10.1088/0022-3727/7/3/312. URL: https://doi.org/10.1088/0022-3727/7/3/312.

[130] Kin Fai Mak et al. "Tightly bound trions in monolayer MoS2". In: *Nature Materials* 12.3 (2013), pp. 207–211. DOI: 10.1038/nmat3505. URL: https://doi.org/10.1038/nmat3505.

[131] Nicholas Rivera et al. "Shrinking light to allow forbidden transitions on the atomic scale". In: *Science* 353.6296 (2016), pp. 263–269. ISSN: 0036-8075. DOI: 10.1126/science.aaf6308. eprint: https://science.sciencemag.org/content/353/6296/263.full.pdf. URL: https://science.sciencemag.org/content/353/6296/263.

[132] I. Khivrich and S. Ilani. "Atomic-like charge qubit in a carbon nanotube enabling electric and magnetic field nano-sensing". In: *Nature Communications* 11.1 (2020), p. 2299. DOI: 10.1038/s41467-020-16001-5. URL: https://doi.org/10.1038/s41467-020-16001-5.

[133] Jean-Philippe Tetienne et al. "Quantum imaging of current flow in graphene". In: *Science Advances* 3.4 (2017). DOI: 10.1126/sciadv.1602429. eprint: https://advances.sciencemag.org/content/3/4/e1602429.full.pdf. URL: https://advances.sciencemag.org/content/3/4/e1602429.

[134] Trond I. Andersen et al. "Electron-phonon instability in graphene revealed by global and local noise probes". In: *Science* 364.6436 (2019), pp. 154–157. ISSN: 0036-8075. DOI: 10.1126/science.

aaw2104. eprint: https://science.sciencemag.org/content/364/6436/154.full.pdf. URL: https://science.sciencemag.org/content/364/6436/154.

[135] J. R. Maze et al. "Nanoscale magnetic sensing with an individual electronic spin in diamond". In: *Nature* 455.7213 (2008), pp. 644–647. DOI: 10.1038/nature07279. URL: https://doi.org/10.1038/nature07279.

[136] F. Dolde et al. "Electric-field sensing using single diamond spins". In: *Nature Physics* 7.6 (2011), pp. 459–463. DOI: 10.1038/nphys1969.

[137] M. J. Yoo et al. "Scanning Single-Electron Transistor Microscopy: Imaging Individual Charges". In: *Science* 276.5312 (1997), pp. 579–582. ISSN: 0036-8075. DOI: 10.1126/science.276.5312.579. eprint: https://science.sciencemag.org/content/276/5312/579.full.pdf. URL: https://science.sciencemag.org/content/276/5312/579.

[138] A. Aharon-Steinberg et al. "Long-range nontopological edge currents in charge-neutral graphene". In: *Nature* 593.7860 (2021), pp. 528–534. DOI: 10.1038/s41586-021-03501-7. URL: https://doi.org/10.1038/s41586-021-03501-7.

[139] Urs P. Wild et al. "Single molecule spectroscopy: Stark effect of pentacene in p-terphenyl". In: *Chemical Physics Letters* 193.6 (1992), pp. 451–455. ISSN: 0009-2614. DOI: https://doi.org/10.1016/0009-2614(92)85830-4. URL: https://www.sciencedirect.com/science/article/pii/0009261492858304.

[140] A. K. Geim and K. S. Novoselov. "The rise of graphene". In: *Nature Materials* 6.3 (2007), pp. 183–191. DOI: 10.1038/nmat1849. URL: https://doi.org/10.1038/nmat1849.

[141] J. Martin et al. "Observation of electron–hole puddles in graphene using a scanning single-electron transistor". In: *Nature Physics* 4.2 (2008), pp. 144–148. DOI: 10.1038/nphys781. URL: https://doi.org/10.1038/nphys781.

[142] Yuanbo Zhang et al. "Origin of spatial charge inhomogeneity in graphene". In: *Nature Physics* 5.10 (2009), pp. 722–726. DOI: 10.1038/nphys1365. URL: https://doi.org/10.1038/nphys1365.

[143] Charles Kittel. *Introduction to Solid State Physics*. 8th ed. Wiley, 2004. ISBN: 9780471415268.

[144] Anshuman Singh et al. "Nanoscale Mapping and Control of Antenna-Coupling Strength for Bright Single Photon Sources". In: *Nano Letters* 18.4 (2018). PMID: 29570309, pp. 2538–2544. DOI: 10.1021/acs.nanolett.8b00239. URL: https://doi.org/10.1021/acs.nanolett.8b00239.

[145] Alexey Shkarin et al. "Nanoscopic Charge Fluctuations in a Gallium Phosphide Waveguide Measured by Single Molecules". In: *Phys. Rev. Lett.* 126 (13 2021), p. 133602. DOI: 10.1103/PhysRevLett.126.133602. URL: https://link.aps.org/doi/10.1103/PhysRevLett.126.133602.

[146] Daniel Cano et al. "Fast electrical modulation of strong near-field interactions between erbium emitters and graphene". In: *Nature Communications* 11.1 (2020), p. 4094. DOI: 10.1038/s41467-020-17899-7. URL: https://doi.org/10.1038/s41467-020-17899-7.